Materials Advances

ROYAL SOCIETY OF CHEMISTRY

REVIEW

View Article Online
View Journal | View Issue

Check for updates

Cite this: *Mater. Adv.*, 2022, **3**, 2612

Fluorescent Schiff base sensors as a versatile tool for metal ion detection: strategies, mechanistic insights, and applications

Manoj Kumar Goshisht,[a] Goutam Kumar Patra[b] and Neetu Tripathi*[c]

Received 12th December 2021,
Accepted 24th January 2022

DOI: 10.1039/d1ma01175h

rsc.li/materials-advances

Metal ions exist globally. Therefore, the study of the design strategies, mechanistic insights, and applications of fluorescent Schiff base sensors for metal ion detection constitutes an active topic of research. Further, theoretical studies on these systems using various spectroscopic techniques add new flavor in terms of providing a better understanding of the photo-electronic properties of Schiff base sensors and their complexes with metals. The presented review article starts with the general introduction of fluorescent Schiff base sensors for metal ion detection, and consists of two main sections. The first section illustrates the strategies and different mechanistic insights into metal ion detection using Schiff base sensors. The second section demonstrates the application of fluorescent Schiff base sensors in metal ion sensing, biomedical imaging, environmental monitoring, and optoelectronic systems. Additionally, a summary of the reviewed fluorescent Schiff base sensors is presented in a table format. Finally, the conclusion and future scope of fluorescent Schiff base sensors for metal ion detections are discussed.

---

[a] *Department of Chemistry, Government Naveen College Tokapal, Bastar, Chhattisgarh 494442, India*

[b] *Department of Chemistry, Faculty of Physical Sciences, Guru Ghasidas Vishwavidyalaya, Bilaspur (Chhattisgarh), 495009, India*

[c] *Department of Chemistry, Guru Nanak Dev University, Amritsar, Punjab 143005, India. E-mail: neetutripathi1990@yahoo.com, neetuchem1990@gmail.com*

Manoj Kumar Goshisht

Dr Manoj Kumar Goshisht is an Assistant Professor of Chemistry at Govt. Naveen College Tokapal, Bastar, Chhattisgarh, India. He obtained his master's degree from Guru Jambheshwar University of Science & Technology, Hisar, Haryana, and PhD degree from Dr B. R. Ambedkar National Institute of Technology, Jalandhar, Punjab, India. He has cleared the National Eligibility Test (CSIR-UGC NET) for Assistant Professor in the subject of Chemical Sciences. He is a winner of the Editors Pick Award of the "9th DST & ACS Workshop" held on 11th August 2021. His research interests include organic chemistry, materials chemistry, supramolecular chemistry, and nanomaterials. He has published various research papers in reputed international peer-reviewed journals such as The American Chemical Society, The Royal Society of Chemistry, and Springer Nature. He also has a book to his credit published by CRC Press (an imprint of the Taylor & Francis group).

Goutam Kumar Patra

Prof. Goutam Kumar Patra received his PhD from Jadavpur University, under the supervision of Prof. Dipankar Datta at Indian Association for the Cultivation of Science, Kolkata. Then he joined Tel Aviv University, Israel, as a postdoctoral research fellow with Prof. Israel Goldberg (2000–2002). Subsequently he moved to Carnegie Mellon University, USA, where he worked with Prof. Catalina Achim. Then he joined as Asst. Prof. in Vijoygarh Jyotish Ray College, Kolkata, in December 2003. He visited Max Planck Institute of Bioinorganic Chemistry, Mülheim, Germany, as a BOYSCAST fellow during 2006–2007 and worked with the then Director, Prof. Karl Wieghardt. He has been a Professor in Guru Ghasidas Central University, Bilaspur, since 2012. His research interests include chemosensors, redox activity, azamacrocyclic chemistry, crystal engineering, porphyrin and supramolecular chemistry, peptide nucleic acids (PNAs) and free radical chemistry. So far, he has published more than hundred research papers in journals of national and international repute.

1. Introduction

The metal ions constitute an active topic of research owing to their global existence. In the human body, metal ions enjoy special status because of their participation in numerous biological processes. In our surroundings, metal ions are present in food, soil, and water.[1] However, the presence of metal ions at concentrations above or below the permissible limit (Table 1) may cause hazardous effects on the environment and human beings.[2–5] In the past, various methods such as inductively coupled plasma atomic emission spectroscopy, inductively coupled plasma mass spectroscopy, electrochemical detection, and ion chromatography have been reported for metal ion detection.[6–10]

However, these methods suffer from limitations such as inadequate practical applications, expensive instruments, time-consuming processes, complicated procedures, *etc.* Recently, significant attention has been paid to developing fluorescent chemosensors for metal ion detection owing to their excellent selectivity, sensitivity as well as rapid response time.[4,11,12]

In recent years, the design and synthesis of fluorescent chemosensors are of central importance because of their straightforward synthesis, tailor-made properties, and rapid, selective, and sensitive detection of the analyte on-site.[13–19] Here, positive metal ion detection may result in visible color change, fluorescence color change, a shift in emission wavelength or intensity (blue-shift or red-shift) or may result in the appearance of new emission maxima.[20–25] Fluorescent chemosensors for metal ion detection generally contain Schiff base,[26–28] pyridine,[29,30] pyrene,[31,32] anthracene,[33,34] quinoline,[35,36] naphthalene,[37] urea,[38,39] coumarin,[40,41] phenolphthalein,[42,43] and rhodamine[44,45] groups as the binding site. Among various fluorescent chemosensors, Schiff base-based sensors have shown outstanding results owing to their simple synthesis, and provide a suitable electronic and geometrical environment for coordination with single metal ions as well as with multiple metal ions simultaneously. Schiff bases commonly include hydrazone, acyl hydrazone, salicylimine, azine, and other groups, and provide nitrogen and oxygen atoms for coordination with metal ions.[46–50] Schiff base-based chemosensors may show the aggregation-induced emission (AIE) phenomenon because of the free rotation around the C═N bond. Additionally, the excited-state intramolecular proton transfer (ESIPT) process was exhibited by chemosensors containing the salicylimine group.[51–54]

Table 1 Permissible concentration levels of metals in drinking water by WHO (World Health Organization) and recommended daily amount (RDA) of metal ions in the human body

Metal ion	In drinking water (mg l^{-1})	In human body	Ref.
Mg^{2+}	50	~300–400 mg day^{-1}	3 and 5
Ca^{2+}	75	—	5
Al^{3+}	0.03 mg l^{-1}	3–10 mg day^{-1}	3 and 4
Sn^{2+}	1–2 μg l^{-1}	—	2
Pb^{2+}	0.05	93.5 μg day^{-1}	5
Cr^{3+}	0.05	50–200 mg day^{-1}	4
Mn^{2+}	0.1 mg/l	2.3 mg day^{-1}	2–4
Fe^{2+}/Fe^{3+}	0.3	8 mg day^{-1}	3–5
Co^{2+}	0.001	5–40 μg day^{-1}	3–5
Ni^{2+}	0.0008	80–130 μg day^{-1}	3–5
Cu^{2+}	1.0	2 mg day^{-1}	3–5
Zn^{2+}	5.0	8 mg day^{-1}	3 and 4
Hg^{2+}	0.001–65	—	4 and 5
Cd^{2+}	0.005	—	4 and 5

Nowadays, Schiff base sensors and their complexes with metal ions have become a hot topic of research owing to their practical application in numerous scientific areas such as in environmental monitoring and in biological cell imaging of target ions within the cells, tissues, and organelles.[4,55–59] Furthermore, the tailor-made and multi-stimuli responsive properties of Schiff bases enable their application in optoelectronic systems.[60–62] The molecular switching properties of Schiff base sensors have been applied in the construction of molecular keypads and logic gates.[63,64]

In the past, significant research work has been done in developing fluorescent Schiff base sensors for metal ion detection.[63,65–71] However, to the best of our knowledge, no review has been reported on metal ion detection using fluorescent Schiff base sensors. In this review article, we start with the general introduction of fluorescent Schiff base sensors for metal ion detection and then divide the article into main sections. The first section illustrates the strategies and different mechanistic insights into metal ion detection using Schiff base sensors. The second section demonstrates the practical applications of fluorescent Schiff base sensors in metal ion sensing, biomedical imaging, environmental monitoring, and optoelectronic systems (Fig. 1). Additionally, a summary of the reviewed fluorescent Schiff base sensors is presented in a table format (Table 2). Finally, the conclusion and future opportunities of

Neetu Tripathi

Dr Neetu Tripathi obtained her PhD from Guru Nanak Dev University, Amritsar, India. She completed her master's with 1st rank (Gold medal) in MSc Chemistry (Instrumental Analysis). She has been a recipient of the prestigious INSPIRE fellowship of the Government of India during her PhD. She has also cleared National Eligibility Test (CSIR-UGC NET) for Assistant Professor and Graduate Aptitude test (GATE) in the subject of chemical sciences. Her research interest includes organic chemistry, materials chemistry, supramolecular chemistry, and nanomaterials. She has published various research papers in international peer-reviewed journals (Royal Society of Chemistry, Elsevier journals and Springer journal). She is also the co-author of a book published by CRC Press (an imprint of the Taylor & Francis group).

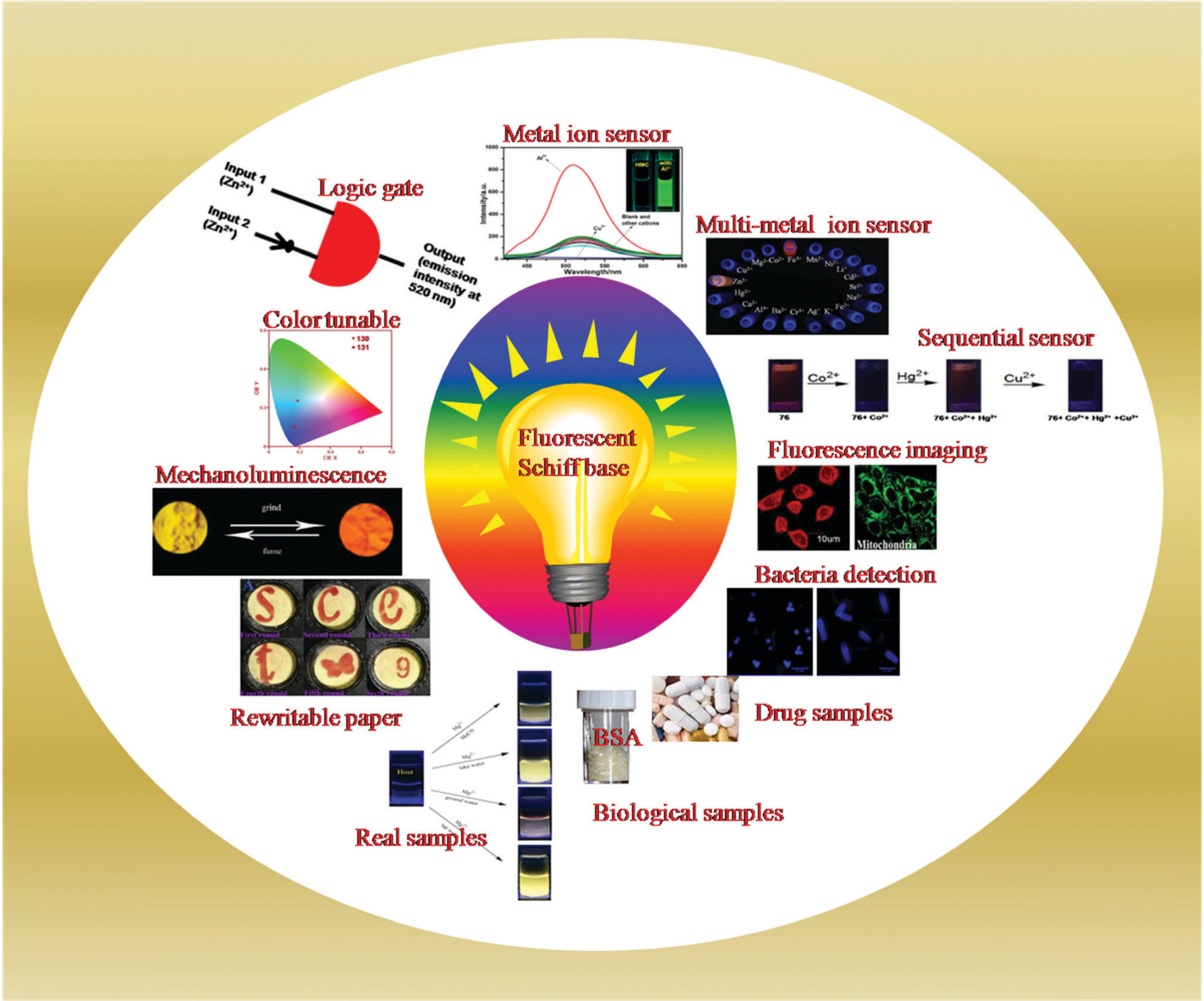

Fig. 1 Practical applications of fluorescent Schiff base sensors.

fluorescent Schiff base sensors for metal ion detection are discussed.

2. Strategies and mechanistic insights into fluorescence-based metal ion detection

The general approach for metal ion detection involves sensor–metal ion coordination interactions. A Schiff base sensor contains a binding functional unit that can coordinate with a metal ion, causing enhancement/quenching of emission intensity, ratiometric fluorescence change, or enhancement/quenching of fluorescence color of the solution, leading to chelation-enhanced fluorescence (CHEF) or chelation-enhanced quenching (CHEQ) effect. The commonly used mechanisms for metal ion detection are formation/disruption of self-assembly/disassembly, aggregation/disaggregation, photo-induced electron transfer (PET), intra/intermolecular charge transfer (ICT), metal to ligand charge transfer (MLCT), ligand to metal charge transfer (LMCT), Förster resonance energy transfer (FRET), excited state intramolecular proton transfer (ESIPT), inner filter effect (IFE), metal-induced chemical change and C═N isomerization.

2.1 Self-assembly/disassembly

Self-assembled molecules are versatile materials for a variety of applications, including analyte detection and fluorescence imaging. In the sensing system, the fluorescence of the sensor can be modulated by analyte interaction and the self-assembly process. In the literature, various strategies such as self-assembly-disassembly driven detection of metal ions, metal ion-induced disassembly, self-assembly coupled with the AIE phenomenon, *etc.* have been used for fluorescence-based detection of metal ions.[202,203] Herein, we will discuss the self-assembly-based mechanism for metal ion detection using fluorescent Schiff base molecules.

Wu *et al.* developed pyrene-based Schiff base **1** with AEE (Aggregation emission enhancement) properties for fluorescence-based

Table 2 Summary of the reported fluorescent Schiff base sensors, fluorescence response, excitation wavelength (λ_{ex}), emission wavelength (λ_{em}), metal ion, limit of detection (LOD), Recovery rates (%) ± RSD (%) (relative standard deviation) in the spiked samples, mechanism, application, and references

Sensor	Fluorescence response	Solvent	λ_{ex} (nm)	λ_{em} (nm)	Metal ion	LOD	Recovery rates (%) ± RSD (%) in the spiked samples	Mechanism	Application	Ref.
1	Turn-on	H_2O–DMF (1 : 1, v/v)	370	455	Cu^{2+}	35 nM	—	Cu^{2+} induced self-assembly	Metal ion sensor, fluorescence imaging of intracellular Cu^{2+}	72
2	Turn-off	99% HEPES buffer–CH_3CN	390	526	Cu^{2+}	0.261 ppb	95 to 120 ± <0.5 in tap water, pond water, and industrial waste water	Disassembly of self-assembled aggregates	Metal ion sensor, cell imaging of HeLa cells, logic circuit, TLC strips	73
3	Blue shift of emission, turn-on	CH_3CN	393	454.5	Cu^{2+}	2.5 μM	—	Coordination of sensor **3** with Cu^{2+} blocks the PET process	Metal ion sensor	32
4	Turn-off	H_2O/DMSO (v/v, 1 : 1)	400	585	Cu^{2+}	32.8 nM	—	Coordination of Cu^{2+} with sensor **4** caused activation of the PET process between coumarin and Cu^{2+}	Metal ion sensor, fluorescence imaging of intracellular Cu^{2+}	41
5	Blue shift of emission, turn-on	Tris–HCl buffer (CH_3OH/H_2O = 9 : 1, v/v)	430	516	Zn^{2+}	0.144 μM	—	PET and CHEF effect	Metal ion sensor	74
6	Turn-on, red-shift in the case of Cu^{2+}	CH_3OH–tris buffer (1 : 1)	340	440	Cu^{2+} and Pb^{2+}	1.2 μM and 0.9 μM for Cu^{2+} and Pb^{2+}, respectively	98.3 to 101.6 ± <1.5 for Cu^{2+}, and 100.7 to 109.8 ± <2 for Pb^{2+} in water samples	PET and ICT process	Metal ion sensor, logic gate, cell imaging	75
7	Turn-off	THF–H_2O (9 : 1, v/v)	365	484	Cu^{2+}	Less than 1 μM	—	Metal to ligand charge transfer, CHEQ	Metal ion sensor	76
8	Turn-off	Aqueous medium	405	517	Cu^{2+}	12.3 nM	—	Ligand to metal charge transfer	Metal ion sensor, secondary sensor for CN^- (turn-on), logic gate, cellular imaging	77
9	Turn-off	DMF/water mixtures	400	525 and 630	Cu^{2+}	9.12 nM	—	FRET	Metal ion sensor	78
10	Turn-on	PBS buffer at pH 7.4	360	415 and 548	Al^{3+}	10 nM	—	ESIPT, metal-template aggregation	Metal ion sensor	79
11	Turn-off	Aqueous medium	350	438	Cr(VI)	0.175 μM	99 to 104 ± <2 in ground and tap water, 102.5 ± <2 in human serum, and 101.5 to 105 ± <2 in vitamin C tablets	Inner filter effect	Metal ion sensor, secondary sensor for ascorbic acid (turn-on), tap water, ground water	80
12	Turn-on	CH_3CN–H_2O (7 : 3, v/v)	305	389	Al^{3+} and Cr^{3+}	88.7 nM and 63.1 nM for Al^{3+} and Cr^{3+}, respectively	97.8 to 103.8 ± <1 for Al^{3+} and 96.5 to 104.8 ± <1.5 for Cr^{3+} in tap and deionized water	Metal induced chemical change, C═N isomerization	Metal ion sensor, tap water	81
13	Turn-on	Ethanol	491	547	Mg^{2+}	0.516 μM	—	PET process, CHEF effect	Metal ion sensor	82
14	Ratiometric fluorescence change	HEPES buffer solution (pH = 7.2)	370	545 and 483	Ca^{2+}	0.3 μM	—	ICT process	Metal ion sensor	83
15	Turn-on	HEPES buffer solution	365	488	Al^{3+}	15.0 nM	94.4 ± 2.2 in tap water	PET process, CHEF effect	Metal ion sensor, test paper, tap water	84
16	Turn-on, blue-shift	Methanol	316	550	Al^{3+}	14 nM	—	CHEF effect	Metal ion sensor	85
17	Turn-on	DMF–H_2O (v/v, 9 : 1)	390	490	Al^{3+}	6.7 μM	—	ICT process, CHEF effect and C═N isomerization	Metal ion sensor	86

Table 2 (*continued*)

Sensor	Fluorescence response	Solvent	λ_{ex} (nm)	λ_{em} (nm)	Metal ion	LOD	Recovery rates (%) ± RSD (%) in the spiked samples	Mechanism	Application	Ref.
18	Turn-on	Ethanol	428	502	Al^{3+}	38.7 nM	—	PET phenomenon, CHEF effect	Metal ion sensor	87
19	Turn-on	Ethanol	350	391	Al^{3+}	0.1 µM	—	PET process, CHEF effect	Metal ion sensor	88
20	Turn-on	Ethanol	410	480	Al^{3+}	31.9 nM	—	PET process, CHEF effect	Metal ion sensor	89
21	Turn-on	Ethanol–H_2O (v/v, 3 : 1)	420	475 and 508	Al^{3+}	18.2 nM	—	PET process	Metal ion sensor, solid state sensor	90
22	Turn-on, blue-shift	Aqueous medium	389	460	Al^{3+}	0.6.9 µM	—	ICT phenomenon	Metal ion sensor	91
23	Turn-on	Ethanol	363	420	Al^{3+}	0.2 µM	—	PET phenomenon, CHEF effect	Metal ion sensor	92
24 and **25**	Turn-on	DMSO–H_2O		493 and 476 for sensors **24** and **25**, respectively	Al^{3+}	14.9 nM and 15.1 nM for sensors **24** and **25**, respectively	—	PET process, CHEF effect	Metal ion sensor	93
26 and **27**	Turn-on	Methanol	410	506 and 489 for sensors **26** and **27**, respectively	Al^{3+}	47.9 nM and 82.8 nM for sensors **26** and **27**, respectively	—	CHEF effect	Metal ion sensor	94
28	Turn-on	Ethanol	394	478	Al^{3+}	4.2 ppm	—	CHEF effect	Metal ion sensor	95
29	Turn-on	DMF	378	481	Al^{3+}	1.2 µM	—	ICT process, CHEF effect	Metal ion sensor	96
30	Turn-on	Methanol–H_2O (9 : 1, v/v)	334	521	Al^{3+}	0.1587 µM	—	PET process, CHEF effect	Metal ion sensor	97
31	Turn-on	DMSO–H_2O (1 : 1, v/v)	320	460	Sn^{2+}	0.314 µM	—	PET process, ICT process, C=N isomerization and CHEF effect	Metal ion sensor	98
32	Turn-on	CH_3CN–H_2O (95/5%)	273	537	Cr^{3+}	0.22 µM	—	PET process, CHEF effect	Metal ion sensor	99
33	Turn-on	CH_3CN–H_2O (95/5%)	360	663	Cr^{3+}	0.13 µM	—	PET process, CHEF effect	Metal ion sensor	100
34	Turn-off	DMF	280	356 and 372	Fe^{3+}	37.5 nM	103 ± 1.9 and 97.5 ± 2.1 in distilled water and tap water, respectively	LMCT	Metal ion sensor	101
35	Turn-on	Aqueous medium	256	505	Fe^{3+}	48.0 nM	—	PET process, CHEF effect	Metal ion sensor	102
36	Turn-on, red-shift	CH_3CN–H_2O (1 : 1, v/v)	300	370	Fe^{2+}	0.15 µM	104.8 ± 0.04, 100.8 ± 0.03, 97.0 ± 0.03, and 93.3 ± 0.05 in tap water, tablets, dark chocolate and tomato juice, respectively	ICT process, CHEF effect	Metal ion sensor, tap water, tablets, dark chocolate and tomato juice	103
37 and **38**	Turn-off	DMF/HEPES buffer (7 : 3, v/v)	318 and 304 for sensors **37** and **38**, respectively	446 and 426 for sensors **37** and **38**, respectively	Fe^{3+}	4.28 µM and 0.83 µM for sensors **37** and **38**, respectively	99.7 to 101.9 ± <1.0 in bottled water, and 100.1 to 100.3 ± <0.8 in tap water	Electron/energy transfer	Metal ion sensor, water samples	104
39	Turn-on	Ethanol	298	350	Co^{2+}	0.782 µM	97.2 to 98.8 ± <3.5 in lake water, and 99.6 to 102.5 ± <2 in tap water	AIE phenomenon	Metal ion sensor, lake water, tap water	105
40	Turn-off	CH_3CN–H_2O (9/1, v/v)	384	429	Cu^{2+}	0.503 µM	102 ± 0.49 in tap water, and 100.5 ± 0.76 in drinking water	LMCT	Metal ion sensor, tap water, drinking water	106
41	Turn-off	DMSO	278	307	Cu^{2+}	0.037 µM	—	Electron transfer	Metal ion sensor	107
42	Turn-off	CH_3CN	296	542	Cu^{2+}	2.4 µM	—	—	Metal ion sensor	108

Table 2 (*continued*)

Sensor	Fluorescence response	Solvent	λ_{ex} (nm)	λ_{em} (nm)	Metal ion	LOD	Recovery rates (%) ± RSD (%) in the spiked samples	Mechanism	Application	Ref.
43	Turn-off, blue-shift	CH_3CN/H_2O (1 : 1, v/v)	310	435	Cu^{2+}	10 μM	—	Nitrogen coordination and cation–π interaction	Metal ion sensor	109
44	Turn-on	CH_3CN	340	369	Cu^{2+}	1.54 nM	—	ICT process, C═N isomerization and CHEF effect	Metal ion sensor	110
45	Turn-off	Aqueous medium	386	554	Cu^{2+}	0.35 μM	—	Electron transfer	Metal ion sensor	111
46 and **47**	Turn-on	DMF	364 and 365 for sensors **46** and **47**, respectively	411 and 416 for sensors **46** and **47**, respectively	Cu^{2+}	1 nM for sensor **47**	—	CHEF effect	Metal ion sensor	112
48	Turn-on	CH_3CN	298	335 and 381	Cu^{2+}	27.4 nM	—	ICT process and C═N isomerization	Metal ion sensor	113
49	Turn-off	CH_3CN/PBS (v/v =9/1)	365	624	Cu^{2+}	0.67 μM	—	Ligand to metal charge transfer (LMCT)	Metal ion sensor, fluorescence bio-imaging	114
50	Turn-on	Ethanol/HEPES buffer (95/5, v/v)	242	450	Zn^{2+}	0.5034 μM	—	(i) Restriction in rotation of the C═N group, (ii) blockage of the PET process, (iii) Zn^{2+} induced dis-aggregation of sensor **50**	Metal ion sensor, fluorescence bio-imaging	115
51	Turn-on	DMF	430	509	Zn^{2+}	8.6 nM	—	CHEF effect and C═N isomerization	Metal ion sensor	116
52	Turn-on	DMF–H_2O (9 : 1, v/v)	380	500	Zn^{2+}	2.59 μM	—	PET process and C═N isomerization	Metal ion sensor	117
53	Turn-on	Ethanol	430	498	Zn^{2+}	0.173 μM	—	PET process, C═N isomerization and CHEF effect	Metal ion sensor	118
54	Turn-on	Water–DMSO (3 : 1 v/v)	340	427	Ag^{+}	3.15 μM	—	PET process, and CHEF effect	Metal ion sensor, real samples	119
55	Turn-off, red-shift	DMSO-buffered H_2O (9/1, v/v)	365	500	Hg^{2+}	0.907 μM	—	Intramolecular charge transfer	Metal ion sensor, lake water, tap water, distilled water	120
56	Turn-on	Methanol/H_2O (8 : 2, v/v)	365	503	Hg^{2+}	20 μM	—	CHEF effect	Metal ion sensor	121
57	Turn-on	CH_3CN–H_2O (9/1, v/v)	349	415 and 473	Hg^{2+}	22.68 nM	—	ESIPT process and C═N isomerization	Metal ion sensor	122
58	Turn-on	Aqueous medium	355	417	Hg^{2+}	0.270 μM	99.5 to 101.0 ± <3 in drinking water and tap water	Metal induced chemical change	Metal ion sensor, drinking water, and tap water	123
61	Turn-on	10% methanol solution (v/v, 0.2 M PBS, pH 7.0)	246	425	Cd^{2+}	2.7 nM	—	Interaction between Cd^{2+} and nitrogen containing moieties in sensor **61**	Metal ion sensor	124
62	Turn-on	CH_3CN–H_2O (8 : 2, v/v)	380	510	Cd^{2+}	14.8 nM	99.5 to 100.5 ± <1.5 in double distilled water, and 99.2 to 101.0 ± <1.5 in tap water	CHEF effect and C═N isomerization	Metal ion sensor, double distilled water, and tap water	125
63	Turn-off	Ethanol	341	385	Ag^{+}, Cu^{2+} and Fe^{3+}	0.132 μM, 0.088 μM, and 0.037 μM, for Ag^{+}, Cu^{2+} and Fe^{3+}, respectively	99.43 ± 0.14, 100.65 ± 0.38, and 101.4 ± 0.39 for Ag^{+}, Cu^{2+} and Fe^{3+}, respectively.	PET process	Multi-metal ion sensor, water samples	126

Table 2 (*continued*)

Sensor	Fluorescence response	Solvent	λ_{ex} (nm)	λ_{em} (nm)	Metal ion	LOD	Recovery rates (%) ± RSD (%) in the spiked samples	Mechanism	Application	Ref.
64	Turn-off	THF/water (6 : 4, v/v)	259	622	Co^{2+}, Cu^{2+} and Hg^{2+}	3.26 nM, 89.1 pM and 0.387 nM for Co^{2+}, Cu^{2+} and Hg^{2+}, respectively	—	The heavy metal ion effect and paramagnetic behavior triggered non-radiative decay	Multi-metal ion sensor, distilled water, tap water	127
65	Turn-on with Hg^{2+} and turn-off with Co^{2+} and Cu^{2+}	DMSO–H_2O (9 : 1, v/v)	460	540	Co^{2+}, Cu^{2+} and Hg^{2+}	0.007 ppb, 0.29 ppb, and 0.20 ppb, respectively, for Co^{2+}, Cu^{2+} and Hg^{2+}	—	The coordination and desulfurization mechanism for Hg^{2+} and disruption of the intramolecular H-bond in the presence of Co^{2+} or Cu^{2+}	Multi-metal ion sensor, tap, lake, drink, ditch and ground water	128
66	Turn-on, red-shift	CH_3CN	355	500	Al^{3+}, Cr^{3+} and Fe^{3+}	0.117 μM, 0.111 μM and 0.106 μM for Al^{3+}, Cr^{3+} and Fe^{3+}	—	Excimer formation and PET process	Multi-metal ion sensor, multi-metal ion sensor, living cell imaging	129
67	Turn-on	Ethanol	510	572 and 580 for Zn^{2+} and Fe^{3+}, respectively	Zn^{2+}, Fe^{3+}	0.664 μM and 0.212 μM for Zn^{2+} and Fe^{3+}, respectively	—	Opening of the lactam ring	Multi-metal ion sensor, distilled water, lake water, running water, well water, and Yangtze river	130
68	Turn-off, red-shift	DMSO–H_2O (1 : 1, v/v)	310	550	Cu^{2+}, Hg^{2+}, Ag^{+}	64.8 μM, 52.7 μM and 63.7 μM for Cu^{2+}, Hg^{2+} and Ag^{+}	—	Coordination of Cu^{2+}, Hg^{2+}, and Ag^{+} with phenolic hydroxyl O, imine N atoms and thiol S, hydrogen bonding	Multi-metal ion sensor	131
69	Turn-off	DMF	341	393	Fe^{2+}, Fe^{3+} and Cu^{2+}	2.06 μM, 2.17 μM, and 2.48 μM for Fe^{2+}, Fe^{3+} and Cu^{2+}, respectively	—	CHEQ	Multi-metal ion sensor	132
70	Turn-on	Ethanol–HEPES buffer (9 : 1, v/v)	420 and 520 for Zn^{2+} and Fe^{3+}, respectively	490 and 583 for Zn^{2+} and Fe^{3+}, respectively	Zn^{2+} and Fe^{3+}	0.134 μM and 0.139 μM for Zn^{2+} and Fe^{3+}	—	PET process, CHEF effect for Zn^{2+} and opening of the spirolactam ring for Fe^{3+}	Multi-metal ion sensor, solid state sensor	133
71	Turn-on, red-shift	CH_3CN	350	539 and 565 for Zn^{2+} and Hg^{2+}, respectively	Zn^{2+} and Hg^{2+}	0.040 μM and 0.011 μM for Hg^{2+} and Zn^{2+}, respectively	—	ICT process and CHEF effect	Multi-metal ion sensor	134
72	Turn-on	DMSO–H_2O (1 : 99, v/v)	300	460 and 434 for Zn^{2+} and Ga^{3+}, respectively	Zn^{2+} and Ga^{3+}	0.32 μM and 0.01 μM for Zn^{2+} and Ga^{3+}, respectively	—	PET process	Multi-metal ion sensor	135
73	Turn-on	CH_3CN	333	536	Al^{3+} and Cr^{3+}	0.31 μM and 0.25 μM for Al^{3+} and Cr^{3+}	—	ESIPT process and $C{=}N$ isomerization	Multi-metal ion sensor	136
74	Turn-off response with Cu^{2+} and turn-on response with Hg^{2+}	THF–H_2O (7 : 3, v/v)	385	537	Cu^{2+} and Zn^{2+}	70.6 nM and 0.116 μM for Cu^{2+} and Zn^{2+}, respectively	—	ICT process, CHEQ for Cu^{2+} and PET process, CHEF for Hg^{2+}	Multi-metal ion sensor	137
75	Turn-on	CH_3CN	380	495	Fe^{3+} and Cr^{3+}	4.57 μM and 2.75 μM for Fe^{3+} and Cr^{3+}, respectively	—	ESIPT process and $C{=}N$ isomerization	Multi-metal ion sensor	138

Table 2 (*continued*)

Sensor	Fluorescence response	Solvent	λ_{ex} (nm)	λ_{em} (nm)	Metal ion	LOD	Recovery rates (%) ± RSD (%) in the spiked samples	Mechanism	Application	Ref.
77 and **78**	Turn-on	DMSO–H_2O (1 : 2, v/v)	405 for sensors **77** and 455 for sensor **78**	505 for sensors **77** and 509 for sensor **78**	Al^{3+}	14.8 nM and 42.3 nM for sensors **77** and **78**, respectively	—	ESIPT process, C=N isomerization and CHEF effect	Metal ion sensor, secondary sensor for F^- (turn-off), filter paper, cell imaging	139
79	Turn-on	DMSO–H_2O (1 : 9, v/v, HEPES buffered)	450	525	Zn^{2+}	0.52 μM	—	ICT	Metal ion sensor, secondary sensor for PPi (turn-off), test paper strips and bioimaging of intracellular Zn^{2+} in HeLa cells	140
80	Turn-off with Co^{2+} and Cu^{2+} and turn-on with Hg^{2+}	THF–H_2O (1 : 99)	360	620	Co^{2+}-Hg^{2+}-Cu^{2+}	0.0937 μM, 0.0221 μM, and 0.0988 μM for Co^{2+}, Hg^{2+} and Cu^{2+}, respectively		Metal ion binding in the cavity of the sensor through oxygen and nitrogen atoms	Multi-metal ion sensor, sequential sensor for Co^{2+}-Hg^{2+}-Cu^{2+}, test strip, living cell imaging	141
81	Turn-on	Ethanol–H_2O buffered (9 : 1, v/v)	330	511	Zn^{2+}	1.2 nM		PET process, C=N isomerization and CHEF effect	Metal ion sensor, secondary sensor for PPi (turn-off), INHIBIT type logic gate	142
82	Turn-off	H_2O–CH_3CN (1 : 1, v/v) PBS buffered	450	521	Cu^{2+}	24.0 nM	—	Sensor **82** carbonyl and imino group binding with Cu^{2+}	Metal ion sensor, secondary sensor for glutathione (turn-on), bioimaging of Cu^{2+} in living cells and zebrafish	143
83	Turn-on, blue-shift	Methanol–water (3 : 1, v/v)	315	512	Zn^{2+}	0.078 μM	—	ESIPT and PET process and CHEF effect	Metal ion sensor, secondary sensor for ATP (turn-off), live cell imaging	144
84	Turn-on	Aqueous medium	350	588	Al^{3+}	1.68 μM	—	Al^{3+} induced hydrolysis of sensor **84**, forming the free –CHO group	Metal ion sensor, secondary sensor for CN^- (turn-off), Al^{3+} detection in A549 cells through live cell imaging	145
85	Turn-off	DMSO–HEPES buffer (4 : 6, v/v)	338	419	Cu^{2+}	2.11 ppb	—	Cu^{2+} induced hydrolysis of the imine functionality of sensor **85**	Metal ion sensor, secondary sensor for PO_4^{3-} (turn-on), paper strips	146
86	Turn-on	90% aqueous methanol	410	520	Al^{3+}	1.62 μM	—	CHEF effect and C=N isomerization	Metal ion sensor, secondary sensor for nucleotides and phosphate ions (turn-off), live cell imaging	147
87	Turn-on, red-shift	Ethanol	400	500	Al^{3+}	63.0 nM	—	Schiff base hydrolysis and CHEF effect	Metal ion sensor, live cell imaging in living HeLa cells	148
88	Turn-on	Methanol/H_2O (9 : 1, v/v)	310	343	Al^{3+}	0.64 μM	—	ICT process, C=N isomerization and CHEF effect	Metal ion sensor, live cell imaging	149
89	Turn-on, red-shift	DMSO–H_2O (1 : 1, v/v) solution	393	467	Cu^{2+}	0.26 μM	—	Strong coordination of sensor **89** with Cu^{2+}	Metal ion sensor, live cell imaging	150
90	Turn-on	DMSO–H_2O (3/7, v/v) solution	346	472	Zn^{2+}	0.018 μM	—	ESIPT, CHEF effect	Metal ion sensor, living cell (African Monkey Vero cells) imaging	151
91	Turn-on	Ethanol–H_2O (1/1, v/v) solution	545	584	Fe^{3+}	28.1 nM	—	Opening of the spirolactam ring	Metal ion sensor, living cell (SMMC-7721 cells) imaging	152

Table 2 (*continued*)

Sensor	Fluorescence response	Solvent	λ_{ex} (nm)	λ_{em} (nm)	Metal ion	LOD	Recovery rates (%) ± RSD (%) in the spiked samples	Mechanism	Application	Ref.
94	Turn-off	CH_3CN/PBS (1 : 1, v/v)	450	540	Cu^{2+}	—	92.90 to 109.3 ± <2 in water samples	—	Metal ion sensor, live cell (MCF-7 and A549 cells) imaging	153
95	Turn-off	HEPES buffer	418	516	Cu^{2+}	0.16 μM	—	MLCT, LLCT	Metal ion sensor, two-photon fluorescence imaging of Cu^{2+} in cellular mitochondria and in the liver and intestine of larval zebrafish	154
96	Turn-on	Ethanol	400	458	Al^{3+}	1.11 nM	—	ESIPT	Metal ion sensor, cell (MCF-7) imaging	155
97	Turn-on	CH_3CN–water (8 : 2) mixture	440	530	Hg^{2+}	1 nM	—	PET and hydrolysis of the C═N group	Metal ion sensor, live cell (MCF-7 cells) imaging	156
98	Turn-on	Buffer solution (ethanol/Tris–HCl, v/v, 4/1)	380	458	Zn^{2+}	1.37 μM	—	PET process, C═N isomerization and CHEF effect	Metal ion sensor, live cell (A549) imaging	157
101	Turn-on	CH_3OH/HEPES buffer (3/7, v/v)	350	435	Al^{3+}	0.05 μM	—	CHEF effect and C═N isomerization	Metal ion sensor, fluorescence imaging in living cells (SW480 cells)	158
102	Turn-on	Ethanol (0.01%)–HEPES buffer	321	450	Al^{3+}	0.1 μM	—	ESIPT process, C═N isomerization and CHEF effect	Metal ion sensor, fluorescence imaging in living cells (HepG2 cells)	159
103	Turn-on	DMSO/H_2O (HEPES buffer, v/v = 3/7)	346	555	Zn^{2+}	60 nM	—	PET process, ESIPT process and CHEF effect	Metal ion sensor, living cell (Vero cells) imaging	160
104	Turn-on, red-shift	DMSO–H_2O (7 : 3, v/v)	347	445	Hg^{2+}	2.82 μM	—	Excimer formation and CHEF effect	Metal ion sensor, live cell (HeLa cells) imaging	161
105	Turn-on	CH_3CN	350	430	Cu^{2+}	86.3 nM	—	PET process and CHEF effect	Metal ion sensor, live cell (Raw264.7 cells) imaging	162
106	Turn-on	Methanol	373	517	Al^{3+}	0.12 μM	—	PET process	Metal ion sensor, live cell (HeLa cells) imaging	163
107	Turn-on	Methanol	307	430	Al^{3+}	0.137 μM	—	ESIPT process	Metal ion sensor, live cell (HeLa cells) imaging, *in vivo* bioimaging of Al^{3+} in zebrafish larvae	164
108	Turn-on	Phosphate buffer–ethanol (7 : 3, v/v) solution	480	516	Au^{3+}	60 nM	—	Metal induced chemical change	Metal ion sensor, PC12 cell and zebrafish imaging	165
109	Turn-on	Buffered CH_3CN–water (1 : 1)	370	450	Zn^{2+}	0.50 μM	—	Complexation of Zn^{2+} with oxygen, nitrogen and sulfur atoms of sensor **109**	Metal ion sensor, live cell (MCF-7 cells) imaging	166
110	Turn-off	Buffered ethanol–water (1 : 1, v/v)	400	566	Cu^{2+}	15.4 nM	—	Excited state energy/electron transfer	Metal ion sensor, live cell (HeLa cells) imaging	167
111	Turn-on	DMSO–H_2O (9 : 1, v/v)	377	479	Al^{3+}	9.79 nM	—	PET process and CHEF effect	Metal ion sensor, live cell (HeLa cells) imaging	168

Table 2 (*continued*)

Sensor	Fluorescence response	Solvent	λ_{ex} (nm)	λ_{em} (nm)	Metal ion	LOD	Recovery rates (%) ± RSD (%) in the spiked samples	Mechanism	Application	Ref.
112	Turn-on, red-shift	Aqueous medium	350	460	Zn^{2+}	10.4 nM	—	C=N isomerization	Metal ion sensor, bacterial cells, *viz. Staphylococcus aureus* and *E. coli*	169
113	Turn-on	Methanol–H_2O (1/9, v/v)	392	448	Al^{3+} and Zn^{2+}	0.804 μM	For Al^{3+}, 96.33 and 96.24 in water and suspension, respectively For Zn^{2+}, 98.60 and 95.05 in water and suspension, respectively	ESIPT, PET process, C=N isomerization and CHEF effect	Metal ion sensor, drug samples such as Gelucil and Zincovit, live cell (HeLa cells) imaging	170
114	Turn-on	Methanol–water (2 : 1, v/v)	340	442	Pb^{2+}	8 nM	105 ± 1.7, 117 ±1.6, and 93 ±1.3 in tap water, river water and urine samples, respectively	PET process and CHEF effect	Metal ion sensor, BSA medium, environmental samples such as tap water, river water and urine samples	171
115	Turn-on	CH_3CN–H_2O (1 : 1, v/v)	360	430	Al^{3+}	50 μM	—	PET process, CHEF effect	Metal ion sensor, BSA medium, live cell (human embryonic kidney (HEK)) imaging	172
116	Turn-on	Methanol–water (2 : 1, v/v)	310	373	Al^{3+}	0.903 μM	98.5% to 101.91% in food samples	PET process, C=N isomerization and CHEF effect	Metal ion sensor, BSA medium	173
117 and **118**	Turn-off	Aqueous medium	370	540	Cu^{2+}, Fe^{3+}	—	—	Host–guest interaction	Anticancer	174
119-124	-	DMSO–H_2O (2 : 8, v/v)	—	422 nm for **119-121**, and 474 nm for **122-124**	—	—	—	Energy dependent, antitumor mechanism of oxidation	Anticancer	175
125	Turn-on	Ethanol–H_2O (4 : 6, v/v)	397	550 nm	Fe^{3+}	0.8 ppb	—	ESIPT	Cancer cells	176
126	Turn-off	DMSO	360	475	Cu^{2+}	—	—	PET process and CHEF effect or due to structural change in the ligand upon complexation	Optical sensor, catalytic oxidation, and Lewis acid–base colour indicator	177
127	Turn-off	DMSO–H_2O (1 : 1, v/v)	414	549	Hg^{2+}	0.284 nM	118.5 to 154.0, 108.0 to 114.0, and 97.7 to 112.0 in lake water, tap water, and mineral water, respectively	Hg^{2+} interaction with the nitrogen atom of the imine group and with the oxygen atom	Adsorption, real water samples, and logic gate	178
128 and **129**	Turn-on	DMF–H_2O (*v*:*v* = 1 : 9)	360 and 300 for sensors **128** and **129**, respectively	483 and 467 for sensors **128** and **129**, respectively	Al^{3+}	3.2 nM and 29.0 nM with sensors **128** and **129**, respectively	—	PET and ESIPT process, CHEF effect	Metal ion sensor, lake water and tap water	179
130	Turn-off, hypsochromic shift	DMF/H_2O (2/3, v/v)	450	560	Cu^{2+}	28.1 nM	94 to 105 ± <2 in tap water, 106 to 117 ± <2.7 in river, and 87 to 93 ± <2.6 in simulated urine samples	Paramagnetic nature of Cu^{2+} and CHQF mechanism	Metal ion sensor, real samples such as water and food	180
131	Turn-on	Methanol	401	524	Al^{3+}	7.4 nM	100.96 to 101.84 ± <0.5 in ultrapure water and 100.0 to 100.10 ± <1.0 in tap water	ICT process and CHEF effect	Metal ion sensor, ultrapure water, tap water	181

Table 2 (*continued*)

Sensor	Fluorescence response	Solvent	λ_{ex} (nm)	λ_{em} (nm)	Metal ion	LOD	Recovery rates (%) ± RSD (%) in the spiked samples	Mechanism	Application	Ref.
132	Turn-on	CH_3CN	353	487 and 532	Mg^{2+}	19.1 ppb	—	C=N isomerization and CHEF effect	Metal ion sensor, tap, ground and lake water	182
133	Turn-off	$THF–H_2O$ (4/1, v/v)	428	565	Cu^{2+}	16.4 nM	99.10 to 102.90 ± <2.01 in lake water and 98.49 to 102.37 ± <2.07 in tap water	ESIPT process, LMCT	Metal ion sensor, running water, artificial lake	183
134	Turn-on	DMF–HEPES (1 : 1, v/v)	350	531	Al^{3+}	86.5 nM	99.7 to 101.7 ± <0.5 in yellow river and 99.0 to 103.4 ± <0.5 in tap water	PET process and CHEF effect	Metal ion sensor, yellow river and tap water	184
135	Turn-on	Tris–HCl buffer (1 : 1, v/v) solution	350	526	Al^{3+}	0.34 μM	100.5 to 102.3 ± <0.3 in yellow river and 99.5 to 102.8 ± <0.3 in tap water	PET process and CHEF effect	Metal ion sensor, yellow river and tap water	185
136	Turn-on	Ethanol–HEPES buffer (95 : 5, v/v)	273	473 and 499	Al^{3+}	0.108 μM	—	PET process	Metal ion sensor, live cell (HeLa cells) imaging, lake, river and distilled water	186
137	Turn-on, blue-shift	$THF–H_2O$ (1 : 1, v/v) mixture	490	550	Zn^{2+}	38.9 nM	—	ESIPT, PET, non-radiative process and CHEF effect	Metal ion sensor, inkless rewritable paper, self-erasing paper, live cell (SiHa cells) imaging	187
138	Turn-on	—	—	Strong emission band between 550 and 700		—	—	Enol to keto form photoisomerization	Rewritable paper and UV sensor	188
141	Turn-on	$CH_3CN–H_2O$ mixture	350	463	Cu^{2+}	0.23 μM		CHEF effect	Metal ion sensor, mechanochromic fluorescence	189
143	Turn-off	HEPES buffered methanol–H_2O (4/1, v/v)	432	508	Cu^{2+} and Zn^{2+}	0.212 μM and 71.9 nM for Cu^{2+} and Zn^{2+}, respectively	—	PET process	Multi-metal ion sensor, solid state piezochromic luminescence	190
145	Turn-on	$THF–H_2O$	367	408 and 481	—	—	—	AIE, ICT	Anti-counterfeiting and printed electronics	191
146 and **147**	Turn-on	DMSO	372	504 and 444 for sensors **146** and **147**, respectively	Zn^{2+}	—	—	ICT process	Color tunable	192
148–152	Turn-on	DMSO	365	447, 440, 436, 433, and 430 for complexes **148**, **149**, **150**, **151**, and **152**, respectively	Zn^{2+}	—	—	Relaxation due to intra-ligand transition	Organic white light emitting devices	193
153	Blue fluorescent	$CHCl_3$, THF, ethanol, CH_3CN, and solid state	345–370	430–460	Zn^{2+}	—	—	Combination of monomer–excimer emission	Blue fluorescent OLED	194

Table 2 (*continued*)

Sensor	Fluorescence response	Solvent	λ_{ex} (nm)	λ_{em} (nm)	Metal ion	LOD	Recovery rates (%) ± RSD (%) in the spiked samples	Mechanism	Application	Ref.
154	Turn-on	HEPES buffered ethanol–H_2O (9 : 1, v/v)	375	520	Zn^{2+}	1.59 μM	—	PET process, C=N isomerization and CHEF effect	Metal ion sensor, logic gate, TLC supported paper strips, and bioimaging of intracellular Zn^{2+} in Vero cells (African green monkey kidney cells)	195
155	Turn-on	Methanol–water (1 : 1, v/v)	370	464	Al^{3+}	10 μM	—	PET process	Metal ion sensor, secondary sensor for PO_4^{3-}, logic gate, BSA medium, live cell (rat L6 myoblast cells) imaging	196
156 and **157**	Turn-on	Methanol	375	465 and 464 for sensors **156** and **157**, respectively	Al^{3+}	0.525 μM and 2.38 μM for sensors **156** and **157**, respectively	—	CHEF effect	Metal ion sensor, logic gate	197
158	Turn-on	Aqueous medium	359	454	Zn^{2+}	0.477 μM	—	ESIPT process, C=N isomerization, and CHEF effect	Metal ion sensor, logic gate, keypad lock, and fluorescence imaging of Zn^{2+} in rice seedlings	198
159	Turn-on	DMSO–water (9 : 1, v/v)	482	With Zn^{2+} (545) and Cd^{2+} (560)	Zn^{2+} and Cd^{2+}	2.7 nM (for Zn^{2+}) and 6.6 nM (for Cd^{2+})	For Zn^{2+}, 83 to 91 in drinking water, and for Cd^{2+}, 103 to 104 in drinking water	CHEF effect	Multi-metal ion sensor, logic gate, TLC plates, and drinking water	199
160	Turn-on	CH_3CN	400	542	Ni^{2+}	8.67 nM	89 to 104.7 ± <0.2 in tap water, 94 to 98.7 ± <0.2 in river water, and 97.3 to 109.5 ± <0.2 in bottled water	CHEF effect	Metal ion sensor, logic gate, live cell imaging (HeLa cells), real samples	200
161	Turn-off	CH_3CN–H_2O (7 : 3)	344	531	Fe^{3+}	0.81 μM	98.56 ± 0.19, 98.81 ± 0.35, 97.91 ± 0.21, 98.81 ± 1.03, 98.46 ± 0.28, 97.96 ± 0.23, and 94.51 ± 0.26 in tap water, lake, well, mineral water, distilled water, purified water and human serum albumin, respectively	ICT process and C=N isomerization	Metal ion sensor, logic gate, test paper, water samples and fluorescent bioimaging	201

detection of Cu^{2+}.[72] In H_2O–DMF (1 : 1, v/v) solution, sensor **1** was weakly fluorescent (Fig. 2 and Table 2). In the presence of Cu^{2+}, sensor **1** displayed strong fluorescence enhancement (4.5-fold) at 455 nm (λ_{ex} = 370 nm). The LOD was 35 nM for Cu^{2+}. The recognition mechanism was attributed to Cu^{2+} induced self-assembly. TEM and SEM results confirmed the spherical particle morphology and aggregation of sensor **1** in the presence of Cu^{2+}.

2.2 Aggregation/disaggregation

Recently, Schiff base sensors with AIE properties have attracted tremendous attention for metal ion detection. Schiff base-based sensors are excellent AIE active molecules in which free rotation around the C=N band is restricted upon coordination with metal ions, leading to emission change. These sensors are weakly emissive in dilute solution but emit strongly upon aggregation assisted by probe–metal ion interaction in solution or in solid-state.

Singh *et al.* developed probe **2** with AIE and ESIPT properties for Cu^{2+} detection in an aqueous medium (Fig. 3A and Table 2).[73] On excitation at 390 nm, the fluorescence spectrum of probe **2** displayed green emission at 526 nm, attributed to the AIE + ESIPT process. Upon gradual addition of an increasing concentration of Cu^{2+}, the emission spectrum of probe **2** revealed quenching of emission intensity and saturation was

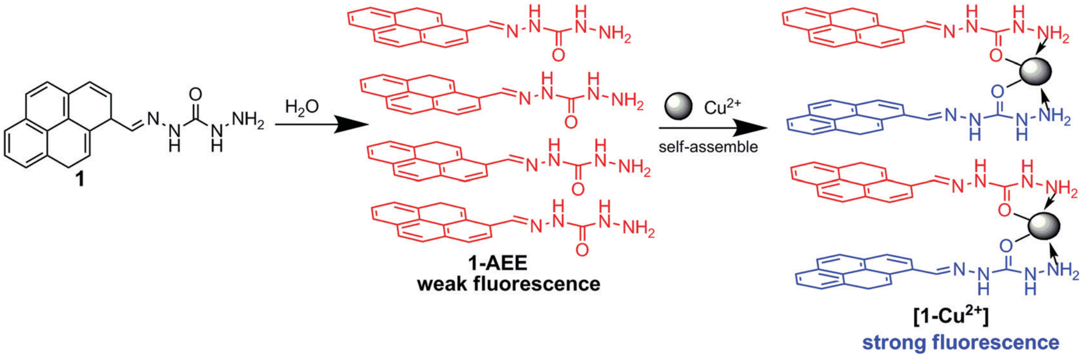

Fig. 2 The sensing mechanism for Cu^{2+} detection using sensor **1**. Reproduced with permission from ref. 72 Copyright 2018, Elsevier.

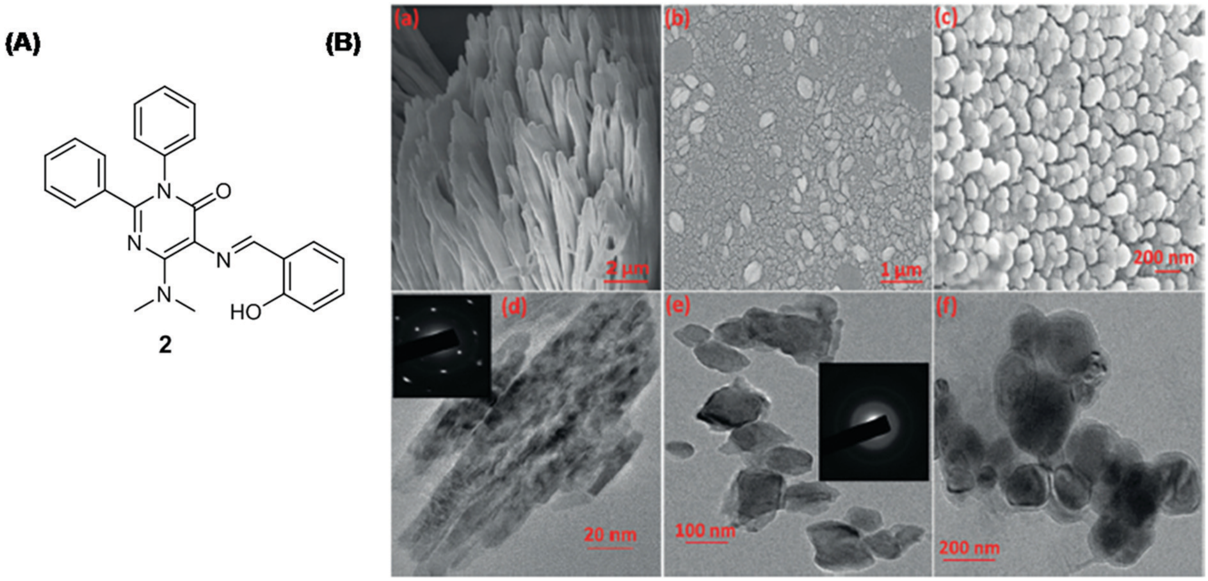

Fig. 3 (A) The chemical structure of sensor **2**. (B) SEM images of (a) sensor **2**; (b and c) sensor **2** + Cu^{2+}; TEM images of (d) sensor **2**; (e and f) sensor **2** + Cu^{2+}; (inset) SAED of aggregates. Reproduced with permission from ref. 73 Copyright 2016, Wiley-VCH Verlag GmbH & Co. KGaA, Weinheim.

achieved after the addition of 1 μM Cu^{2+}. The limit of detection was 0.261 ppb for Cu^{2+}. The coordination of probe **2** with Cu^{2+} resulted in the disassembly of self-assembled aggregates of probe **2** from self-assembled nanorods into smaller spherical nanostructures (Fig. 3B).

2.3 Photoinduced electron transfer (PET)

PET is a process where electron transfer occurs from the donor to the acceptor in the excited state. The coordination of metal ions with the Schiff base sensor may favor or disrupt the PET process, resulting in emission change.

Chakraborty *et al.* developed pyrene-based Schiff base **3** with AIE properties for fluorescence-based detection of Cu^{2+} (Fig. 4 and Table 2).[32] Sensor **3** was found to be selective for Cu^{2+} with an LOD of 2.5 μM. Sensor **3** was weakly fluorescent because of the PET process between the imine bond and the pyrene ring. The complexation of sensor **3** with Cu^{2+} blocked the PET process and resulted in fluorescence enhancement.

Wang *et al.* developed coumarin-based Schiff base **4** with AIRE (Aggregation induced ratiometric emission) properties and employed it as a turn-off sensor for Cu^{2+} detection (Fig. 5 and Table 2).[41] The complexation of Cu^{2+} with sensor **4** caused activation of the PET process between coumarin and the Cu^{2+} center, resulting in fluorescence quenching.

Dong *et al.* synthesized Schiff base **5** as a turn-on sensor for Zn^{2+} detection.[74] Sensor **5** showed excellent sensitivity for Zn^{2+} over other tested metal ions. In the off-state, the PET process occurs from the HOMO of the azomethine group to the HOMO of the conjugated aromatic ring, whereas in the on-state the PET process is inhibited due to coordination of Zn^{2+} with the nitrogen atom and oxygen atom of the azomethine group, and electron transfer occurs from the LUMO to the HOMO of the conjugated aromatic ring (Fig. 6A, B and Table 2).

2.4 Intra/intermolecular charge transfer (ICT)

In the ICT process, energy relaxation of the excited molecule occurs *via* the charge transfer phenomenon. Charge transfer

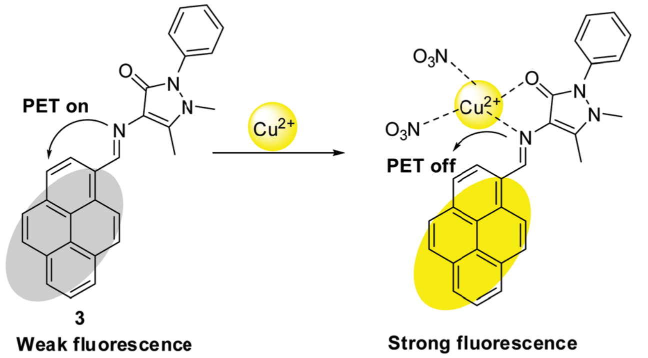

Fig. 4 PET-based mechanism for Cu^{2+} detection with sensor **3**. Reproduced with permission from ref. 32 Copyright 2018, Elsevier.

can be intramolecular where redistribution of charge occurs within the excited molecule or intermolecular in which charge is transferred from the excited donor molecule to the neighboring acceptor molecule.

Rout *et al.* designed triazole-based Schiff base **6** as a turn-on fluorescent sensor for Cu^{2+} and Pb^{2+} detection (Fig. 7 and Table 2).[75] In methanol–tris buffer (1 : 1) medium, the free sensor displayed weak emission at 440 nm (λ_{ex} = 340 nm), attributed to the PET process from the triazole and imine moiety to the fluorophore. In the presence of Cu^{2+}/Pb^{2+}, the fluorescence spectrum of sensor **6** displayed an increase in emission intensity attributed to blockage of the PET process and strengthening of the ICT process. The limit of detection was 1.2 μM and 0.9 μM for Cu^{2+} and Pb^{2+}, respectively.

2.5 Metal to ligand charge transfer (MLCT)

Pannipara *et al.* developed an AIE-active Schiff base **7** as a turn-off sensor for Cu^{2+} detection (Fig. 8 and Table 2).[76] In the THF–H_2O (9 : 1, v/v) mixture, sensor **7** showed intense emission at 484 nm. Upon addition of Cu^{2+} to the solution of sensor **7**, a significant decrease in fluorescence intensity was observed, attributed to metal to ligand charge transfer between Cu^{2+} and sensor **7**, resulting in the CHEQ effect.

2.6 Ligand to metal charge transfer (LMCT)

Bhardwaj *et al.* developed chromone-based fluorescent organic nanoparticles (FON-**8**) for Cu^{2+} and CN^- detection in an aqueous medium (Fig. 8 and Table 2).[77] The fluorescence spectrum of FON-**8** showed a gradual decrease in emission intensity at 517 nm (λ_{ex} = 405 nm) upon the addition of an increasing concentration of Cu^{2+}, attributed to ligand to metal charge transfer. The limit of detection was 12.3 nM for Cu^{2+}. From the DFT method, for sensor **8**, the HOMO was located on the naphthalene moiety and the LUMO was located on the whole sensor **8**. However, in the case of the **8**-Cu^{2+} complex, the LUMO was shifted toward the metal center, demonstrating ligand to metal charge transfer.

2.7 Förster resonance energy transfer (FRET)

FRET is a non-radiative process where energy transfer occurs from excited donors to acceptor molecules. The metal–Schiff base complexation may inhibit or trigger the FRET process resulting in emission change.

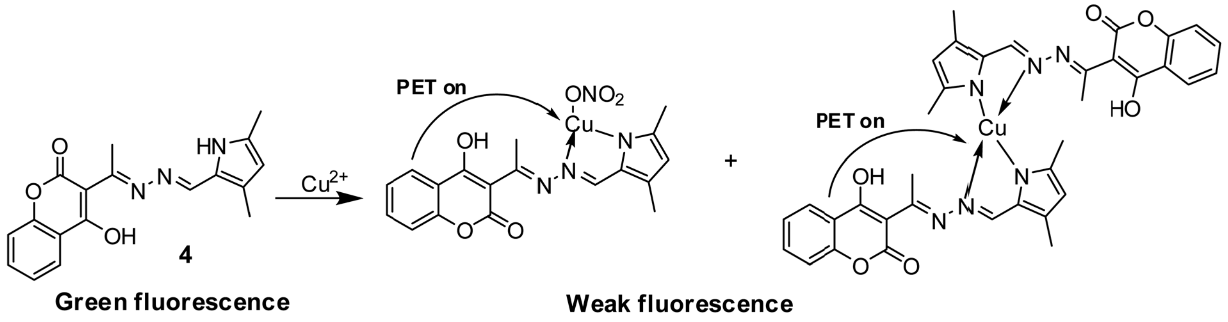

Fig. 5 PET-based mechanism for Cu^{2+} detection with sensor **4**. Reproduced with permission from ref. 41 Copyright 2018, Elsevier.

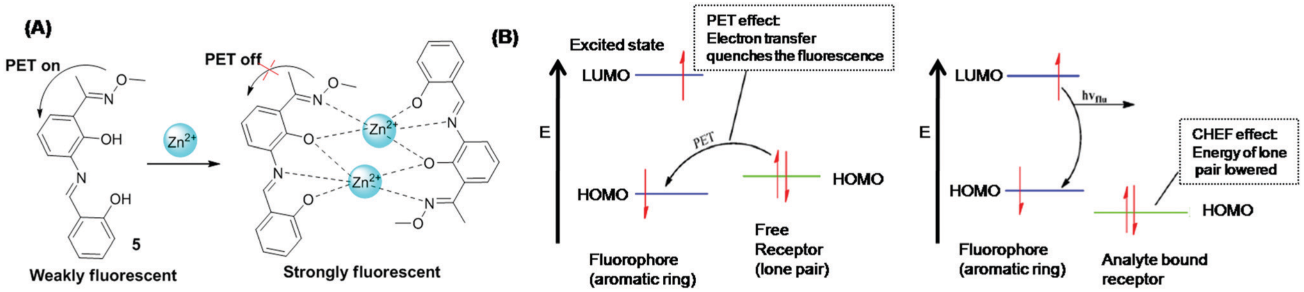

Fig. 6 (A) Sensing mechanism of sensor **5** for Zn^{2+} detection. (B) Orbital energy diagrams showing (a) fluorescence quenching by the PET process; (b) fluorescence enhancement due to the CHEF effect. Reproduced with permission from ref. 74 Copyright 2017, Elsevier.

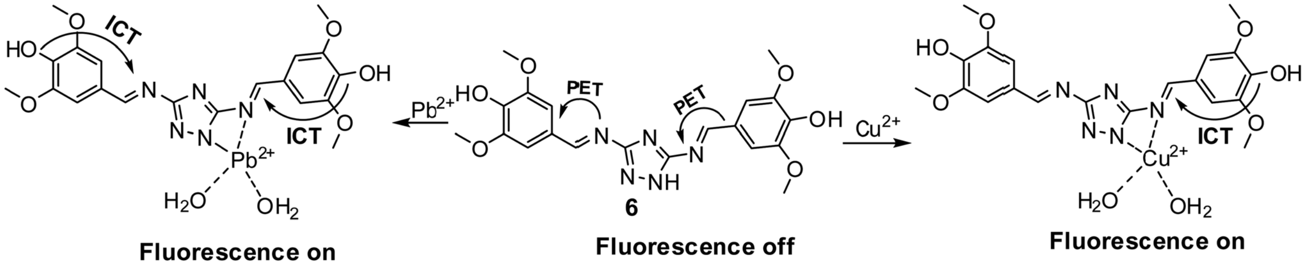

Fig. 7 ICT- and PET-based sensing mechanism for Pb^{2+} and Cu^{2+} detection with sensor **6**. Reproduced with permission from ref. 75 Copyright 2019, Royal Society of Chemistry.

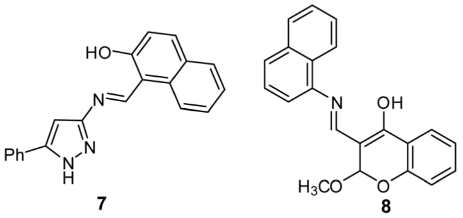

Fig. 8 Chemical structure of sensors **7** and **8**. Reproduced with permission from ref. 76 Copyright 2017, Elsevier.

Yang *et al.* developed a novel method for Cu^{2+} detection through the AIE and FRET strategy in an aqueous medium (Fig. 9 and Table 2).[78] The Schiff base sensor **9** exhibited AIE properties with green emission at 525 nm. In the presence of Cu^{2+}, sensor **9** underwent fluorescence quenching and the limit of detection was 0.132 μM. However, through the sensor **9**–NiR FRET system, the LOD for Cu^{2+} was reduced to 9.12 nM upon monitoring emission intensity at 620 nm.

2.8 Excited-state intramolecular proton transfer (ESIPT)

In the ESIPT process, generally, the transfer of protons occurs from the donor (NH, OH, *etc.*) to the acceptor (carbonyl, nitrogen, *etc.*). ESIPT based sensors generally show two emission bands, one due to the enol-form, and the other due to the tautomeric keto-form. Additionally, ESIPT based sensors show a large Stokes shift, high quantum yield, a low energy gap, *etc.* Usually, salicylimine type Schiff bases exhibit the ESIPT phenomenon because of keto–enol tautomerization.[48,49]

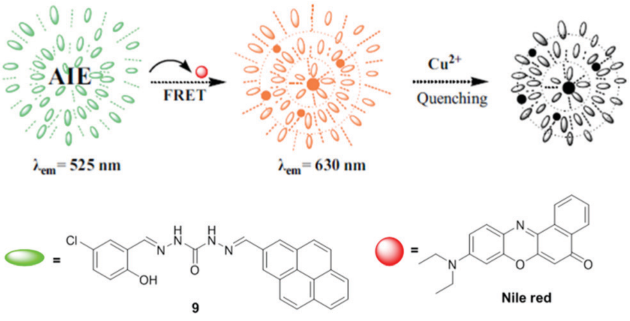

Fig. 9 FRET-based sensing mechanism for Cu^{2+} detection with sensor **9**. Reproduced with permission from ref. 78 Copyright 2019, Elsevier.

Puri *et al.* developed Schiff base sensor **10** with AIE properties for fluorescence-based detection of Al^{3+} in methanol solution.[79] On excitation at 360 nm, sensor **10** displayed emission at 548 nm accompanied by a large Stokes shift (188 nm), attributed to the ESIPT phenomena. Upon addition of Al^{3+} to the solution of sensor **10**, further enhancement in emission intensity was observed with emission maxima at 476 nm and a Stokes shift of 116 nm, attributed to metal–template aggregation (Fig. 10 and Table 2).

2.9 Inner filter effect (IFE)

The inner filter effect is a radiative process where the excitation and/or emission energy of the probe is absorbed by the absorber in the sensing system. Earlier, it was considered as a source of error in fluorescence measurements. Nowadays, researchers have shown more interest in developing IFE-based sensors because (i) this approach is simple and straightforward, *i.e.* it does not require sensor–analyte interaction, and (ii) absorber's absorbance change transforms exponentially into emission change, resulting in increased sensitivity. The basic requirement for IFE to act is spectral overlap between the absorber's absorbance band and the excitation and/or emission band of the sensor.[204]

Abbasi and Shakir *et al.* developed IFE-based Schiff base sensor **11** for Cr (VI) detection in an aqueous medium (Fig. 11A and Table 2).[80] On excitation at 350 nm, sensor **11** showed emission maxima at 438 nm. Upon addition of Cr(VI), the fluorescence of sensor **11** was adequately quenched. The sensing mechanism was attributed to IFE, based on the good overlap between the absorption band of Cr(VI) (centered at 260 nm, 350 nm, and 440 nm) and the excitation band (at 350 nm) and/or emission band (at 438 nm) of sensor **11** (Fig. 11B). The limit of detection for Cr(VI) was 0.175 μM.

2.10 Metal-induced chemical change and C═N isomerization

Sometimes, the interaction of metal ions with the sensor results in some chemical reaction that changes the chemical structure of the ligand, resulting in emission change.

Hu *et al.* developed fluorene-naphthalene-based Schiff base sensor **12** for Al^{3+} and Cr^{3+} detection.[81] In CH_3CN–H_2O (7 : 3, v/v) solution, free sensor **12** was weakly emissive (λ_{ex} = 305 nm). In the presence of Al^{3+} or Cr^{3+}, sensor **12** underwent fluorescence enhancement 722 times and 923 times, respectively. The

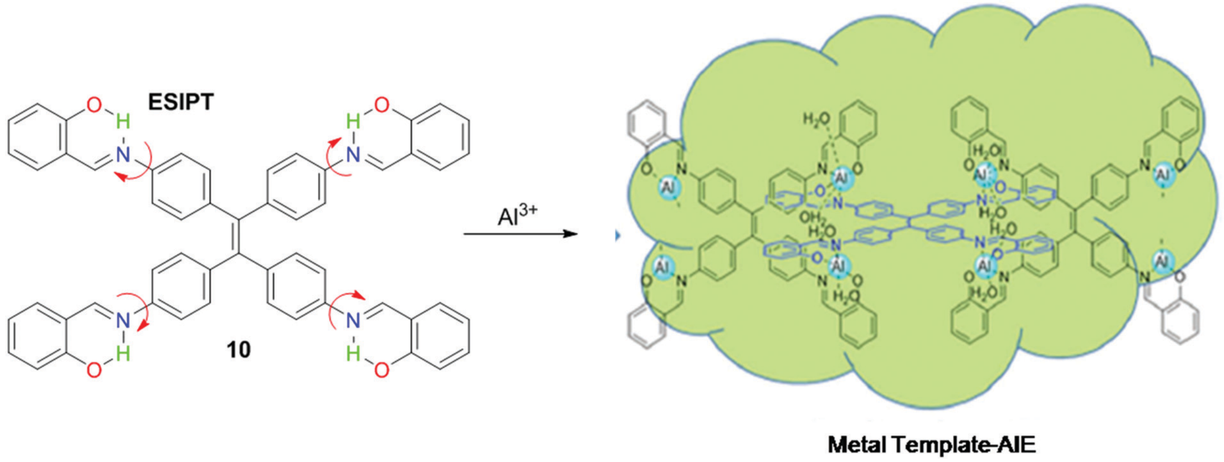

Fig. 10 ESIPT based sensing mechanism for Al^{3+} detection with sensor **10**. Reproduced with permission from ref. 79 Copyright 2018, Royal Society of Chemistry.

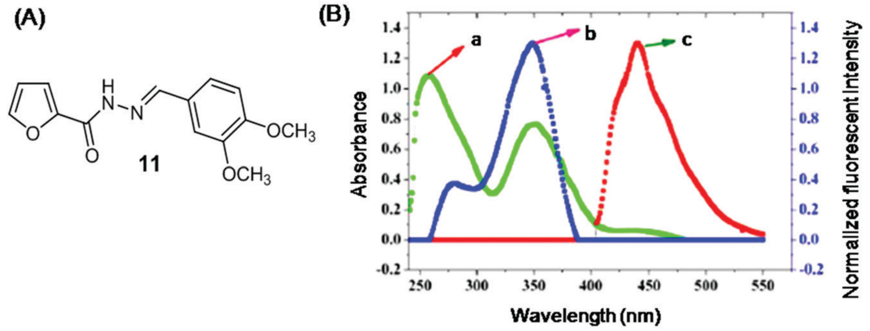

Fig. 11 (A) Chemical structure of sensor **11**. (B) (a) Absorbance spectrum of Cr(IV); normalized fluorescence (b) excitation and (c) emission spectrum of sensor **11**. Reproduced with permission from ref. 80 Copyright 2018, Royal Society of Chemistry.

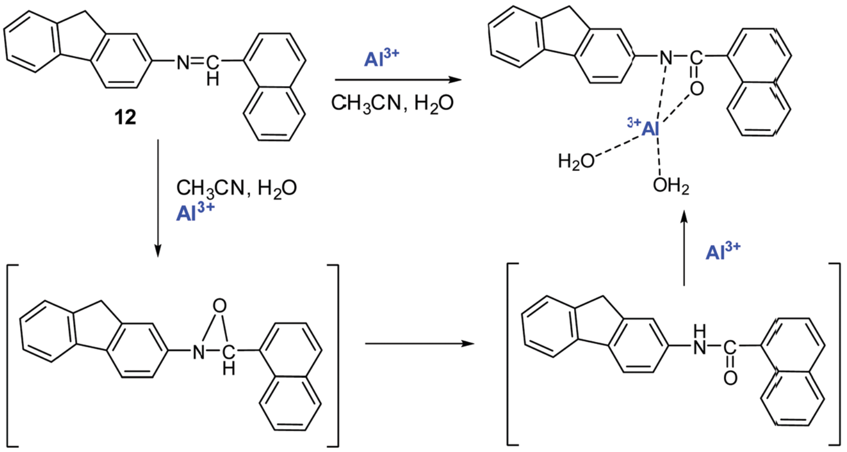

Fig. 12 Sensing mechanism of sensor **12** with Al^{3+}. Reproduced with permission from ref. 81 Copyright 2021, Elsevier.

limit of detection was 0.887 nM and 0.631 nM for Al^{3+} and Cr^{3+}, respectively. The recognition mechanism was a reaction-based process, wherein first oxidation of the C═N group of sensor **12** C═N to O = C-NH occurred in the presence of Al^{3+} or Cr^{3+}, and then coordination, which resulted in inhibition of C═N isomerization and in strong emission (Fig. 12 and Table 2).

3. Applications

3.1 Metal ion sensors

Some metal ions are very crucial for life such as Fe^{3+}, Zn^{2+}, K^{+}, *etc.*, whereas others such as Hg^{2+}, Pb^{2+}, Cd^{2+}, *etc.*, may cause serious environmental and health issues.[1] Accordingly, detection of metal ions present in trace amounts is important. Recently, fluorescent Schiff base sensors for metal ion detection have grabbed significant attention because of their simplicity, selectivity, sensitivity, real-time detection, fast response time, and non-destructive properties. In addition, Schiff bases are eminent hard bases and have electron-rich oxygen and nitrogen donor atoms for coordination with metal ions.

3.1.1 Mg^{2+} sensor. Magnesium is an essential mineral for human beings, playing several important functions such as blood pressure regulation, bone development, muscle contraction, immune system improvement, catalysis of many enzyme-driven biochemical reactions, acting as a cofactor for many enzymes, *etc.*[205] However, both excess intake or deficiency of magnesium ions results in serious diseases such as Alzheimer's disease, hypertension (due to excess intake of magnesium), and hypocalcemia, diabetes, migraine (due to deficiency of magnesium).[206,207] Thus, the detection of magnesium using fluorescent chemosensors is an interesting area of research.

Wang *et al.* developed Schiff base **13** as a turn-on sensor for fluorescence-based detection of Mg^{2+} (Fig. 13 and Table 2).[82] In

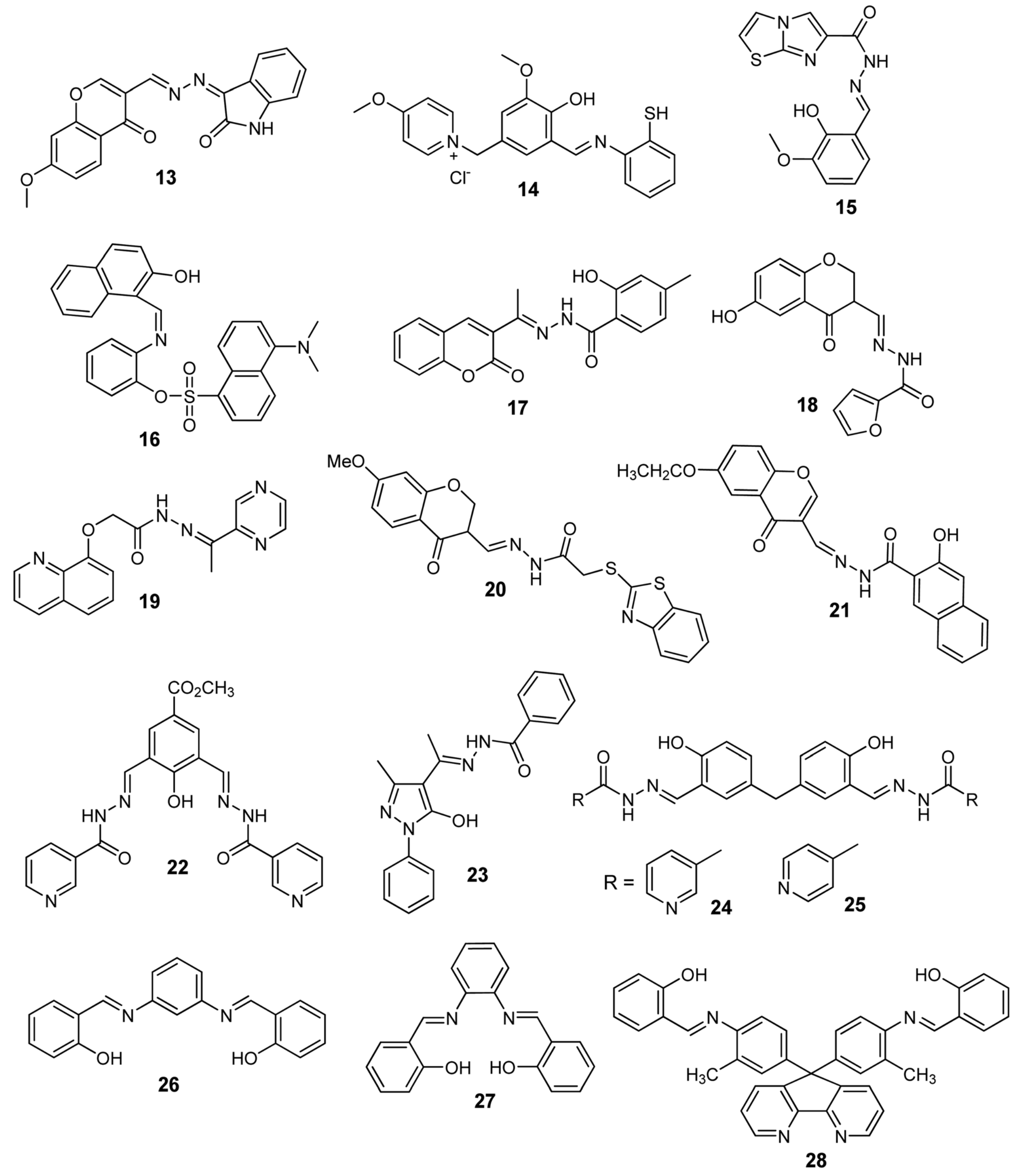

Fig. 13 Chemical structure of sensors **13–28**.

ethanol solution, sensor **13** displayed weak emission at wavelength 547 nm (λ_{ex} = 491 nm). Upon addition of Mg^{2+}, sensor **13** displayed a 70-fold increase in fluorescence intensity at 547 nm. The detection limit was 0.516 μM for Mg^{2+}. Job's plot showed 1 : 1 (**13**/Mg^{2+}) stoichiometry and the association constant was 3.33×10^4 M^{-1} as calculated using the Benesi–Hildebrand equation. The chelation of sensor **13** with Mg^{2+} through oxygen and nitrogen atoms resulted in blockage of the PET process, causing fluorescence enhancement through the CHEF effect.

3.1.2 Ca^{2+} sensor. Calcium ions play key roles in human biology, for example, signal transduction, muscle contraction, bone formation, *etc.* However, the abnormal concentration of calcium ions in the body is an indicator of serious health problems.[208] Excess calcium ion concentration (hypocalcaemia) in the body can cause hyperparathyroidism, sarcoidosis, and cardiac arrhythmias,[209] whereas its deficiency (hypocalcaemia) may lead to osteoporosis, vitamin D deficiency, and hypoparathyroidism.[210] Therefore, the use of fluorescent sensors for Ca^{2+} detection is a topic of immense interest for health monitoring and diagnostic purpose.

Saleh *et al.* reported Schiff base sensor **14** as a ratiometric fluorescent sensor for Ca^{2+} (Fig. 13 and Table 2).[83] In HEPES buffer solution (pH = 7.2), the free sensor showed a broad band with emission maxima at 545 nm (λ_{ex} = 370 nm). The fluorescence titration with Ca^{2+} revealed ratiometric fluorescence change with the simultaneous increase in emission intensity at 483 nm and decrease in emission intensity at 545 nm. The limit of detection was 0.3 μM Ca^{2+} and the stoichiometry of the complex was 1 : 1 (**14** : Ca^{2+}). The binding of Ca^{2+} with sensor **14** at the coordination sites, *i.e.*, OH, C=N, SH, decreases the ICT process present in the sensor and results in ratiometric fluorescence change.

3.1.3 Al^{3+} sensor[96,97,211–216]**.** Aluminum is the third most abundant element (8.3%) in the earth crust after oxygen and silicon. While aluminum has no biological role, over-exposure to aluminum may lead to neurotoxicity and Alzheimer's disease.[217,218] Al^{3+} is a hard acid and coordinates well with hard bases such as oxygen and nitrogen atoms of the Schiff base ligand.

Wang *et al.* synthesized an imidazo[2,1-*b*]thiazole-based Schiff base (**15**) as a turn-on sensor for Al^{3+} detection (Fig. 13 and Table 2).[84] In HEPES buffer solution, sensor **15** was almost non-fluorescent. Upon addition of Al^{3+}, the fluorescence spectrum of sensor **15** displayed emission enhancement at 488 nm (λ_{ex} = 365 nm) along with a color change of the solution from colorless to bluish-green (Fig. 14). The complexation stoichiometry was 1 : 1 (**15**/Al^{3+}). The limit of detection and the association constant for Al^{3+} were 15.0 nM and 7.42×10^4 M^{-1}, respectively. The sensing mechanism could be attributed to inhibition of the PET process and the CHEF effect.

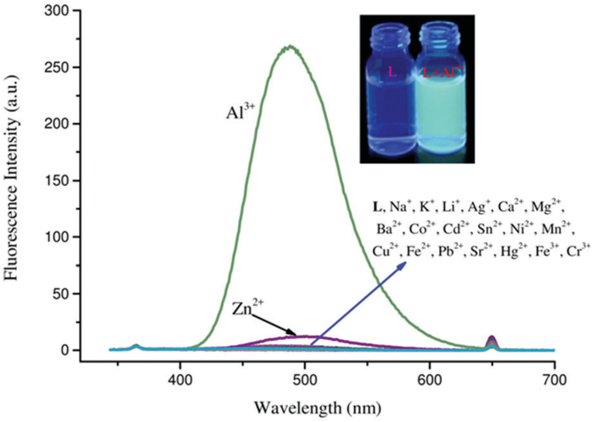

Fig. 14 Fluorescence spectrum of sensor **15** in the presence of different metal ions. Inset: photographs of **15** (**L**) and **15** + Al^{3+} solution under UV lamp illumination. Reproduced with permission from ref. 84 Copyright 2021, Wiley-VCH GmbH.

Chang *et al.* synthesized dansyl-based sensor **16** for fluorescence-based detection of Al^{3+} (Fig. 13 and Table 2).[85] In methanol solution, sensor **16** exhibited weak emission at 550 nm (λ_{ex} = 316 nm). Fluorescence titration with Al^{3+} revealed a prominent increase in emission intensity accompanied by a blue shift of the emission maxima from 550 nm to 448 nm ($\Delta\lambda_{shift}$ = 102 nm). Job's plot revealed the 1 : 1 (**16** : Al^{3+}) stoichiometry of the complex (Fig. 15A). The association constant was 9.40×10^6 M^{-1} and the limit of detection was 14 nM for Al^{3+}. In the ^1H NMR titration experiment, the presence of a broad peak at 9.9 ppm and two singlets of the imine protons suggested Al^{3+} coordination at the imine site, thus inhibiting C=N isomerization, causing the CHEF effect (Fig. 15B).

Hossain *et al.* developed coumarin-based Schiff base chemosensor **17** for Al^{3+} detection (Fig. 13 and Table 2).[86] Sensor **17** exhibited high selectivity for Al^{3+} among various other metal ions in DMF–H_2O (v/v, 9 : 1). Upon addition of Al^{3+}, sensor **17** underwent a ∼34-fold increase in fluorescence intensity at 490 nm (λ_{ex} = 390 nm). The stoichiometry of the complex was 1 : 1 (**17** : Al^{3+}) and the detection limit was 6.7 μM for Al^{3+}. The turn-on fluorescence response of sensor **17** with Al^{3+} was associated with the combined effect of ICT, CHEF, and C=N isomerization.

Li *et al.* designed and synthesized chromone-based sensor **18** as a turn-on sensor for Al^{3+} (Fig. 13 and Table 2).[87] In ethanol solution, sensor **18** showed weak emission in the range of 440–690 nm. Among various metal ions, sensor **18** underwent 171-fold fluorescence enhancement with Al^{3+} at 502 nm (λ_{ex} = 428 nm) and to a lesser extent with Mg^{2+} and Zn^{2+}, whereas other metal ions had an insignificant effect on the fluorescence spectrum of sensor **18**. The limit of detection was 38.7 nM for Al^{3+}. The binding constant was 1.74×10^7 M^{-1} and the stoichiometry of the complex was 1 : 1 (**18** : Al^{3+}). The turn-on mechanism could be ascribed to the deactivation of the PET phenomenon upon chelation of Al^{3+} with sensor **18**, forming a rigid system, and causing the CHEF effect.

Li *et al.* prepared pyrazine-based sensor **19** for fluorescence-based detection of Al^{3+} (Fig. 13 and Table 2).[88] Sensor **19** was weakly fluorescent with emission at 391 nm (λ_{ex} = 350 nm) in ethanol solution. Upon addition of various metal ions, *viz.* Al^{3+}, Ca^{2+}, Ba^{2+}, Mg^{2+}, Fe^{3+}, Cr^{3+}, Co^{2+}, Cu^{2+}, Ni^{2+}, Pb^{2+}, Hg^{2+}, Cd^{2+} and Zn^{2+}, sensor **19** showed a drastic increase in fluorescence intensity at 488 nm with Al^{3+} and to a lesser extent with Fe^{3+}

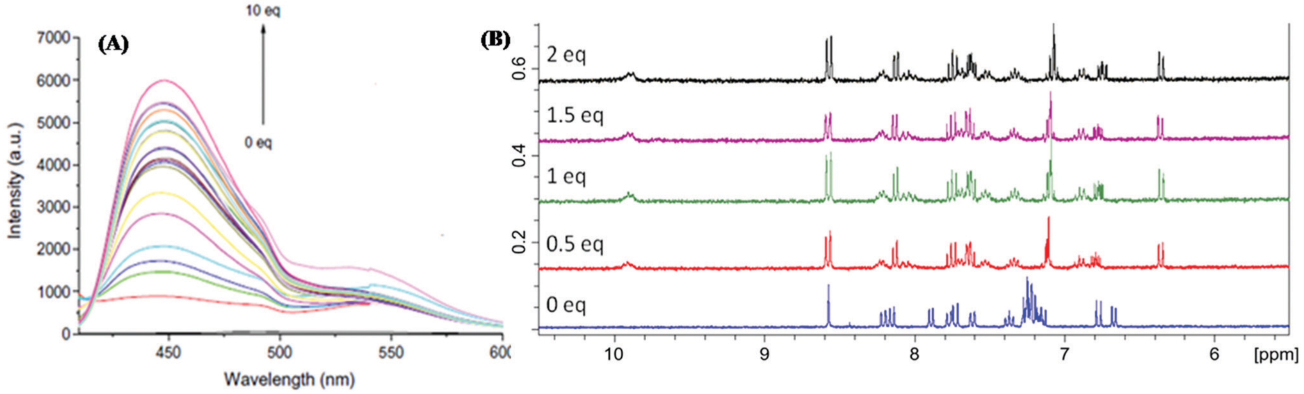

Fig. 15 (A) Fluorescence titration of sensor **16** with the increasing concentration of Al^{3+} in CH_3OH. (B) ^1H NMR titration of sensor **16** with the increasing concentration of Al^{3+} in CD_3OH. Reproduced with permission from ref. 85 Copyright 2015, Elsevier.

and Cr^{3+} ions, whereas other metal ions had an insignificant effect. The binding constant was 1.35×10^4 M^{-1} as calculated using the Benesi–Hildebrand equation. The detection limit was 0.1 μM. Job's plot revealed the 1 : 1 (**19** : Al^{3+}) stoichiometry of the complex. The complexation of Al^{3+} with sensor **19** caused the deactivation of the PET process and resulted in turn-on emission through the CHEF effect.

Liu *et al.* synthesized chromone-based Schiff base sensor **20** and evaluated it for Al^{3+} detection (Fig. 13 and Table 2).[89] In ethanol solution, sensor **20** (λ_{ex} = 410 nm) was non-fluorescent. On addition of various metal ions to the solution of sensor **20**, only Al^{3+} caused significant (~500-fold) fluorescence enhancement at 480 nm. The association constant of the complex was 1.21×10^4 M^{-1} as calculated using the Benesi–Hildebrand equation. The detection limit was 31.9 nM for Al^{3+}. Job's plot and ESI mass spectra revealed the 1 : 1 (**20** : Al^{3+}) stoichiometry of the complex. The coordination of Al^{3+} caused inhibition of the PET phenomenon and resulted in turn-on fluorescence through the CHEF effect.

Liu and Yang further synthesized chromone-based Schiff base sensor **21** for Al^{3+} detection (Fig. 13 and Table 2).[90] Sensor **21** exhibited high selectivity and sensitivity for Al^{3+} detection among various other metal ions. In ethanol-H_2O (v/v, 3 : 1), upon addition of Al^{3+}, sensor **21** underwent a drastic increase in fluorescence intensity at 475 nm and 508 nm (λ_{ex} = 420 nm). The detection limit was 0.182 μM for Al^{3+}. Job's plot revealed 2 : 1 (**21** : Al^{3+}) stoichiometry and the association constant was 9.24×10^3 M^{-1}. Sensor **21** coordinates with Al^{3+} through two nitrogen atoms of azomethine groups forming a 2 : 1 (**21**:Al^{3+}) complex, which inhibits the PET process and results in a turn-on fluorescence response. Sensor **21** also found potential application in the detection of Al^{3+} in solid-state.

Qin and Yang prepared bis-Schiff base sensor **22** for Al^{3+} detection (Fig. 13 and Table 2).[91] In an aqueous solution, free sensor **22** was weakly fluorescent with emission maxima at 506 nm (λ_{ex} = 389 nm). Among various metal ions, sensor **22** displayed strong fluorescence enhancement only with Al^{3+} and to a lesser extent with Zn^{2+}. Fluorescence titration with Al^{3+} showed an increase in fluorescence intensity with a blue shift of the emission maxima from 506 nm to 460 nm ($\Delta\lambda_{shift}$ = 40 nm). The detection limit was 0.69 μM for Al^{3+}. Job's plot revealed 1 : 1 (**22** : Al^{3+}) stoichiometry and the binding constant was 1.67×10^4 M^{-1}. The turn-on fluorescence response could be attributed to the inhibition of the ICT phenomenon due to the chelation of sensor **22** with Al^{3+} through imine nitrogen, the oxygen atom of the carboxylate group, and the oxygen atom of the phenolic hydroxyl group.

Qin *et al.* designed Schiff base sensor **23** for fluorescence-based detection of Al^{3+} (Fig. 13 and Table 2).[92] In ethanol solution, the fluorometric behavior of sensor **23** toward various metal ions revealed high selectivity only for Al^{3+}. The detection limit was 0.2 μM. The complexation stoichiometry was 1 : 1 (**23** : Al^{3+}) and the binding constant was 7.54 M^{-1}. In the presence of Al^{3+}, sensor **23** underwent a drastic increase in emission intensity at 420 nm (λ_{ex} = 363 nm). The sensing mechanism could be attributed to the inhibition of the PET phenomenon due to the chelation of the –C=N– group nitrogen atom with Al^{3+}, causing the CHEF effect.

Ruo *et al.* synthesized 5,5′-methylenebis(salicylaldehyde)-based Schiff base sensors **24** and **25** for Al^{3+} detection (Fig. 13 and Table 2).[93] In DMSO-H_2O solution, both sensors **24** and **25** are weakly fluorescent with emission at 491 nm and 473 nm, respectively. Among various metal ions, sensors **24** and **25** displayed a 70-fold and 40-fold increase in fluorescence intensity at 493 nm and 476 nm, respectively, only with Al^{3+}. The binding constants of sensors **24** and **25** with Al^{3+} were 2.01×10^4 M^{-1} and 5.46×10^5 M^{-1}, respectively, and the stoichiometry of the complex was 1 : 1 (**24**/**25** : Al^{3+}). The detection limit of sensors **24** and **25** for Al^{3+} was 14.9 nM and 15.1 nM, respectively. The ^1H NMR titration experiment revealed that sensors **24** and **25** chelated with Al^{3+} through the nitrogen atom of the imine moiety and the oxygen atom of the hydroxyl group, which resulted in deactivation of the PET process and fluorescence enhancement through the CHEF effect.

Shoora *et al.* synthesized Schiff base sensors **26** and **27** for fluorescence-based detection of Al^{3+} (Fig. 13 and Table 2).[94] Both sensors **26** and **27** are weakly fluorescent in methanol solution. Among various metal ions, both sensors **26** and **27** showed strong fluorescence enhancement with Al^{3+} and to a lesser extent with Zn^{2+} and Cr^{3+}, whereas other metal ions had an insignificant effect. Fluorescence titration of sensors **26** and **27** with Al^{3+} revealed an increase in emission intensity at 506 nm (λ_{ex} = 410 nm) and 489 nm (λ_{ex} = 410 nm), respectively. The increase in fluorescence intensity was associated with a change in the color of the solution from colorless to blue, which can be detected by the naked eye under UV lamp illumination. The detection limit of sensors **26** and **27** for Al^{3+} was 47.9 nM and 82.8 nM, respectively. Job's plot indicated 1 : 1 (**26**/**27** : Al^{3+}) complex stoichiometry and the stability constant was 1.41×10^4 M^{-1} and 1.59×10^4 M^{-1} for sensors **26** and **27**, respectively. The mechanism of sensing could be ascribed to the CHEF process.

Zhang *et al.* synthesized Schiff base sensor **28** as a fluorescence turn-on sensor for Al^{3+} (Fig. 13 and Table 2).[95] In ethanol solution, free sensor **28** was weakly fluorescent with emission at 478 nm (λ_{ex} = 394 nm). Among various metal ions, sensor **28** showed 200-fold fluorescence enhancement at 478 nm only with Al^{3+}, whereas other metal ions had an insignificant effect. The fluorescence change was associated with a change in the color of the solution from colorless to blue, which can be detected by the naked eye under UV lamp illumination. The limit of detection was 4.2 ppm for Al^{3+}. The association constant was 1.4×10^7 M^{-1} and the complex stoichiometry was 1 : 1 (**28** : Al^{3+}). The coordination of Al^{3+} with sensor **28** caused the CHEF effect.

Kumar *et al.* prepared 4-(*N*,*N*-diethylamino)salicylaldehyde-based Schiff base sensor **29** for Al^{3+} detection in DMF solution.[96] Upon the addition of Al^{3+}, sensor **29** displayed a turn-on fluorescence response (cyan color, λ_{em} = 481 nm) toward Al^{3+} over other tested metal ions. Sensor **29** binds with Al^{3+} in a 2 : 1 manner, forming a six coordinated Al^{3+}-complex, and resulting in inhibition of the ICT process and leading to turn-on emission through the CHEF effect (Fig. 16, 17 and Table 2).

Wang *et al.* synthesized tetrastyrene based sensor **30** (AIE-active) for fluorescence-based detection of Al^{3+} in methanol–H_2O (9 : 1, v/v) solution (Fig. 18, Table 2).[97] The free sensor **30** was weakly fluorescent. With the addition of Al^{3+}, the fluorescence spectrum of sensor **30** displayed an increase in emission intensity at 521 nm (λ_{ex} = 334 nm) and a good linear relationship (0–1.8×10^{-5} M). The binding ratio and the binding constant were 1 : 1 (**30** : Al^{3+}) and 2.24×10^4 M^{-1}, respectively. The sensing mechanism was attributed to inhibition of the PET process and the CHEF effect. From the ^1H NMR titration experiment, with the addition of Al^{3+}, the disappearance of proton signals at 10.97 ppm (–OH), a slight shift of proton signals at 12.17 ppm (–CH═N–), and splitting of proton signals at 9.10 ppm (–CH═N–) indicated chelation of Al^{3+} with the nitrogen atom of the imine group, the oxygen atom of the phenol hydroxyl group and the oxygen atom of aldehyde in sensor **30**.

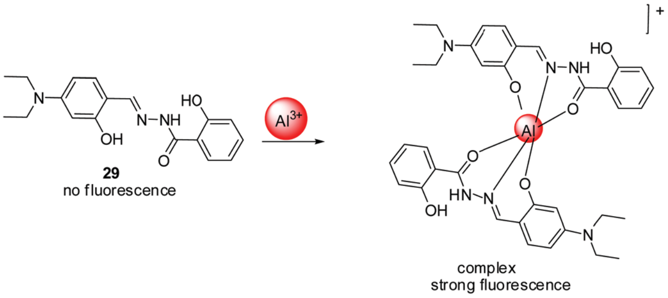

Fig. 16 Sensing mechanism for Al^{3+} detection with sensor **29**. Reproduced with permission from ref.96 Copyright 2022, Elsevier.

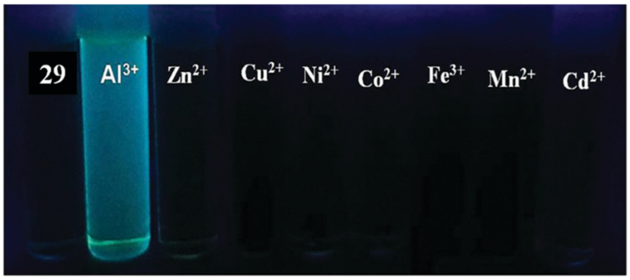

Fig. 17 Photographs of sensor **29** solution in the presence of different metal ions under 364 nm UV light illumination. Reproduced with permission from ref. 96 Copyright 2022, Elsevier.

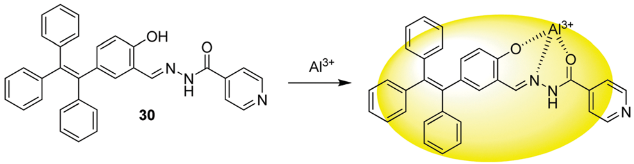

Fig. 18 Sensing mechanism for Al^{3+} detection with sensor **30**. Reproduced with permission from ref. 97 Copyright 2021, Elsevier.

3.1.4 Sn^{2+} sensor. Sn(II) is an essential trace mineral for the human body.[219] In our daily life, stannous chloride ($SnCl_2$) is widely used in food manufacturing and processing, and to conserve soft drinks. According to the World Health Organization, the maximum limit of tin in canned food is 250 μg per kg. However, tin consumption above 200 μg per kg can damage living cells and can lead to serious gastrointestinal problems.[2,220]

Kolcu *et al.* designed and synthesized sensor **31** as a turn-on sensor for Sn(II) (Fig. 19 and Table 2).[98] In DMSO–H_2O (1 : 1, v/v) solution, sensor **31** was non-fluorescent due to C═N isomerization and the PET process. However, in the presence of Sn^{2+}, the fluorescence spectrum of sensor **31** displayed a strong emission band at 460 nm (λ_{ex} = 320 nm) along with a color change of the solution from yellow to deep blue under a UV lamp. The chelation of Sn^{2+} with sensor **31** resulted in inhibition of the PET process and C═N isomerization, resulting in fluorescence enhancement through the CHEF effect. The complexation stoichiometry was 1 : 2 (**31**/Sn^{2+}) and the binding constant was 6.8×10^9 M^{-2}. The limit of detection was 0.314 μM for Sn^{2+}.

3.1.5 Cr^{3+} sensor. Cr^{3+} is an essential micronutrient of our balanced diet. In the human body, Cr^{3+} is involved in various

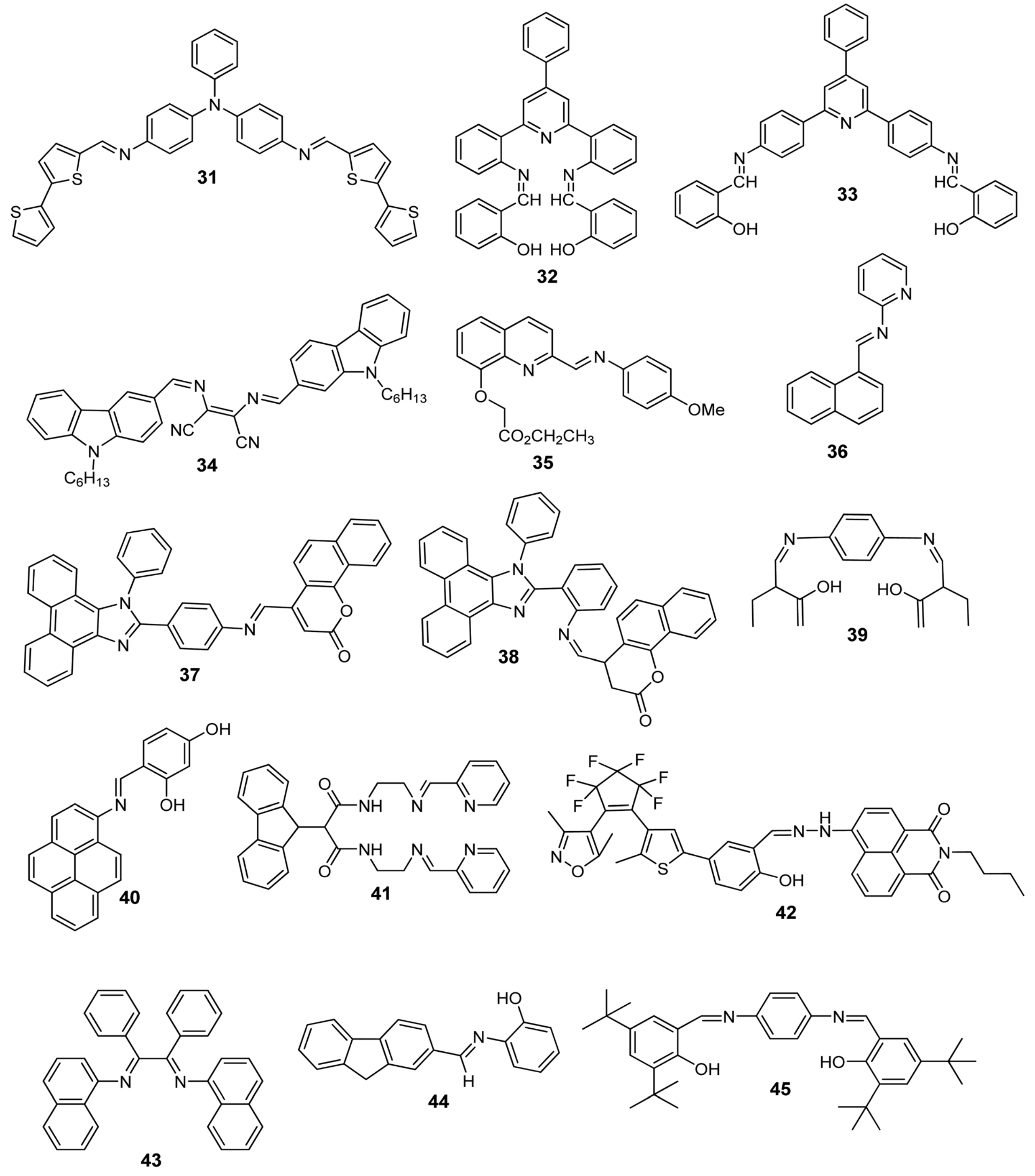

Fig. 19 Chemical structure of sensors **31–45**.

processes such as maintaining insulin balance, metabolism of carbohydrates, proteins and fats, *etc.* However, excess concentration of Cr^{3+} leads to genotoxic diseases, whereas deficiency of Cr^{3+} causes cardiovascular diseases and diabetes.[221] Therefore, the development of a fluorescent sensor for Cr^{3+} detection is an interesting field of research.

Chalmardi *et al.* utilized Schiff base sensor **32** for Cr^{3+} detection (Fig. 19 and Table 2).[99] In acetonitrile–water (95/5%), sensor **32** displayed high selectivity for Cr^{3+} over other metal ions. In the presence of Cr^{3+}, sensor **32** underwent fluorescence enhancement at 537 nm (λ_{ex} = 273 nm). The complex stoichiometry was 1 : 1 (**32** : Cr^{3+}). The binding constant was 8.77×10^4 M^{-1} as calculated using the Benesi–Hildebrand equation. The limit of detection was 0.22 μM for Cr^{3+}. The sensing mechanism could be ascribed to the blockage of the PET process due to coordination of Cr^{3+} with the imine moiety and the phenolic hydroxyl group of sensor **32**, causing fluorescence enhancement through the CHEF effect.

The same group further reported another Schiff base sensor **33** for Cr^{3+} detection (Fig. 19 and Table 2).[100] In acetonitrile–water (95/5%), free sensor **33** was weakly fluorescent. In the presence of Cr^{3+}, sensor **33** showed a rapid turn-on fluorescence response at 663 nm (λ_{ex} = 360 nm). The stoichiometry of the complex was 1 : 1 (**33** : Cr^{3+}) and the association constant was 2.28×10^5 M^{-1}. The detection limit was 0.13 μM for Cr^{3+}. The mechanism of detection was inhibition of the PET phenomenon because of Cr^{3+} coordination with sensor **33**, causing turn-on fluorescence through the CHEF effect.

3.1.6 Fe^{2+}/Fe^{3+} sensor[222–224]. Iron is one of the essential elements and it plays a very significant role in living systems such as in oxygen uptake, oxygen metabolism, the electron transfer process, and as a cofactor in various enzymatic reactions. However, an unbalanced concentration of iron in living systems is connected with serious diseases such as anaemia, heart failure, cell damage, liver damage, *etc.* Therefore, detection of iron is important for monitoring health problems and illness diagnosis. Though iron exists in Fe^{2+} and Fe^{3+} forms, comparatively Fe^{3+} is more stable and highly studied as an analyte based on the fluorescent sensor.[225]

He *et al.* designed carbazole-based Schiff base **34** as an on–off sensor for Fe^{3+} detection (Fig. 19 and Table 2).[101] Upon excitation at 280 nm, the fluorescence spectrum of **34** displayed emission in the range of 330–520 nm in DMF solution. Sensor **34** exhibited high selectivity for Fe^{3+} among various other metal ions. 60% quenching in fluorescence intensity of sensor **34** was observed with 10 equivalents of Fe^{3+}. Job's plot revealed 1 : 1 (**34**/Fe^{3+}) complex stoichiometry. The binding constant was 7.98×10^{-6} M^{-1} and the limit of detection was 37.5 nM. The mechanism of interaction could be attributed to the charge transfer process (LMCT) from sensor **34** to Fe^{3+}.

Li *et al.* developed quinoline-based sensor **35** for fluorescence-based detection of Fe^{3+} (Fig. 19 and Table 2).[102] In an aqueous solution, free sensor **35** was non-fluorescent. Upon addition of Fe^{3+}, sensor **35** underwent a 44-fold increase in emission intensity at 505 nm (λ_{ex} = 256 nm). Various other tested metal ions had insignificant effects on the fluorescence spectrum of sensor **35**. Job's plot indicated 1 : 1 (**35**/Fe^{3+}) binding stoichiometry. The binding constant was 7.22×10^4 M^{-1} and the detection limit was 4.8×10^{-8} M for Fe^{3+}. The coordination of Fe^{3+} with sensor **35** resulted in blockage of the PET process and turn-on emission through the CHEF effect.

Santhoshkumar *et al.* reported naphthalene pyridine-based Schiff base **36** as a fluorescent sensor for Fe^{2+} detection (Fig. 19 and Table 2).[103] Sensor **36** was weakly fluorescent in acetonitrile–H_2O (1 : 1, v/v) solution. In the presence of Fe^{2+} (λ_{ex} = 300 nm), sensor **36** underwent fluorescence enhancement along with red-shift in emission wavelength from 345 nm to 370 nm. In comparison with other metal ions, sensor **36** exhibited selective fluorescence response with Fe^{2+} only. Job's plot indicated 2 : 1 (**36**/Fe^{2+}) binding stoichiometry and the binding constant was 5.02×10^4 M^{-1}. The limit of detection was 0.15 μM for Fe^{2+}. The coordination of Fe^{2+} with sensor **36** through the imine moiety inhibited the ICT process present in free sensor **36** and caused fluorescence enhancement through the CHEF effect. Sensor **36** found potential application in Fe^{2+} detection in real samples.

Zhao *et al.* designed phenanthro[9,10-*d*]imidazole-coumarin-based Schiff bases **37** and **38** as fluorescent sensors for Fe^{3+} detection (Fig. 19 and Table 2).[104] In DMF/HEPES buffer (7 : 3, v/v) solution, the fluorescence spectrum of free sensors **37** and **38** displayed emission maxima at 446 nm (λ_{ex} = 318 nm) and 426 nm (λ_{ex} = 304 nm), respectively. Among various metal ions, both sensors **37** and **38** underwent fluorescence quenching only with Fe^{3+}. The detection limit of sensors **37** and **38** was 4.28 μM and 0.83 μM, respectively, for Fe^{3+}. The binding constant of sensors **37** and **38** with Fe^{3+} was 1.52×10^5 M^{-1} and 7.69×10^4 M^{-1}, respectively. The binding stoichiometry was 1 : 1 (**37**/**38** : Fe^{3+}). The observed fluorescence quenching could be attributed to electron/energy transfer from Fe^{3+} to sensors **37** and **38** because of the paramagnetic nature of Fe^{3+}. Both sensors **37** and **38** found potential application in Fe^{3+} detection in real water samples.

3.1.7 Co^{2+} sensor. Co^{2+} is an essential trace element in the human body. It is an active center of vitamin B_{12} and enzymes. It is also used in lithium-ion batteries, alloys, *etc.* Co-60 is an important radioisotope used for gamma ray production and in radioactive tracer studies.[226,227] However, an increase/decrease in the concentration of cobalt ions from normal in humans and animals causes adverse effects on the respiratory system and central nervous system, kidney failure, anaemia, *etc.*[228] Therefore research on the development of fluorescent sensors which can selectively and sensitively coordinate with Co^{2+} is of immense interest.[229]

Zhang *et al.* synthesized salicylal derived Schiff base sensor **39** for fluorescence-based detection of Co^{2+} (Fig. 19 and Table 2).[105] Among various metal ions, sensor **39** showed high selectivity only for Co^{2+} in ethanol solution (Fig. 20). Fluorescence titration of sensor **39** with Co^{2+} revealed an increase in emission intensity at 350 nm (λ_{ex} = 298 nm). The plot of fluorescence intensity *vs* the concentration of Co^{2+} was linear in the range of 8.0×10^{-7} to 2.0×10^{-6} M. The limit of detection was 0.782 μM for Co^{2+}. Job's plot revealed the 1 : 4

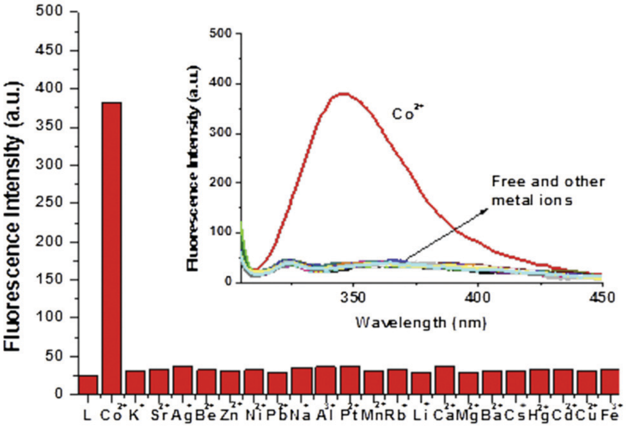

Fig. 20 Fluorescence response of sensor **39** with different metal ions in ethanol solution. Reproduced with permission from ref. 105 Copyright 2017, Elsevier.

(**39** : Co^{2+}) stoichiometry of the complex. ^1H NMR studies in the absence and presence of Co^{2+} suggested the involvement of the nitrogen atom of the N═C–H group and the phenolic O–H group in coordination with Co^{2+}. Sensor **39** could be used for Co^{2+} monitoring in environmental systems.

3.1.8 Cu^{2+} sensor[108,110,114,230–236]. Cu^{2+} is an essential trace dietary element in the human body and participates in various physiological processes, for example in normal functioning of the immune system, nervous system and cardiovascular system.[237,238] The unbalanced concentration of Cu^{2+} is associated with diseases such as Wilson's diseases, hypoglycemia, liver damage, *etc.* Furthermore, due to excessive use of copper in industry and agriculture, copper is a major pollutant of the environment.[239] Thus, development of selective and sensitive methods for Cu^{2+} detection is a challenging area of research.

Dalbera *et al.* developed pyrene-based Schiff base sensor **40** for Cu^{2+} detection (Fig. 19 and Table 2).[106] In CH_3CN–H_2O (9/1, v/v), the fluorescence experiment revealed the high selectivity of sensor **40** towards Cu^{2+} over other metal ions, *viz.* K^+, Na^+, Ni^{2+}, Pb^{2+}, Hg^{2+}, Zn^{2+}, Al^{3+}, Co^{2+}, and Fe^{3+}. Upon gradual addition of Cu^{2+}, sensor **40** underwent a 93% decrease in emission intensity at 429 nm (λ_{ex} = 384 nm). The fluorescence quenching could be ascribed to the reduction of π-conjugation in sensor **40** upon coordination with Cu^{2+}, because of sensor **40** to metal charge transfer (LMCT). Job's plot indicated 2 : 2 (**40** : Cu^{2+}) stoichiometry and the detection limit was 0.503 μM for Cu^{2+}. The quenching constant as calculated using the Stern–Volmer equation was $1.38 \times 10^5\ M^{-1}$. The binding constant as obtained using the Benesi–Hildebrand equation was $5.65 \times 10^5\ M^{-1}$. Sensor **40** also found potential application in Cu^{2+} detection in real water samples such as tap water and drinking water.

Carlos *et al.* prepared fluorene-based Schiff base sensor **41** and utilized it for metal ion detection in DMSO solutions (Fig. 19 and Table 2).[107] Among various metal ions, sensor **41** exhibited significant fluorescence quenching at 307 nm (λ_{ex} = 278 nm) with Cu^{2+}. The stoichiometry of the complex was 2 : 1 (Cu^{2+}/**41**). The Stern–Volmer constant (K_{sv}) and the binding constant of sensor **41** with Cu^{2+} were $2.26 \times 10^{12}\ M^{-1}$ and $1.74 \times 10^{12}\ M^{-1}$, respectively. The detection limit was 0.037 μM for Cu^{2+}. The coordination of one Cu^{2+} through the imine group as well as the nitrogen atom of the amide group and the second Cu^{2+} through the pyridine ring nitrogen atom as well as oxygen atoms from solvent molecules facilitated electron transfer from Cu^{2+} to sensor **41** and resulted in fluorescence quenching.

Fu *et al.* synthesized Schiff base sensor **42** using diarylethene and the 1,8-naphthalimide unit (Fig. 19 and Table 2).[108] In acetonitrile solution, sensor **42** showed significant fluorescence and color change with Cu^{2+} in comparison with other metal ions. Sensor **42** underwent fluorescence quenching at 542 nm (λ_{ex} = 296 nm) with Cu^{2+} and the color of the solution changed from bright green to dark. Job's plot and the mass spectrum revealed 1 : 1 (**42**/Cu^{2+}) stoichiometry. The binding constant was $3.13 \times 10^4\ M^{-1}$ as calculated using the modified Benesi–Hildebrand equation. The limit of detection was 2.4 μM.

Kumar *et al.* reported naphthylamine and benzyl-derived sensor **43** for Cu^{2+} detection (Fig. 19 and Table 2).[109] In CH_3CN/H_2O (1 : 1, v/v) solution, the fluorescence spectrum of sensor **43** displayed emission at 435 nm (λ_{ex} = 310 nm). Upon addition of Cu^{2+}, sensor **43** underwent a decrease in fluorescence intensity associated with the blue shift of the emission maxima from 435 nm to 410 nm. The plot of fluorescence intensity ratio *vs* the concentration of Cu^{2+} was linear in the range of 5×10^{-5} to 3×10^{-4} M. The detection limit was 10^{-5} M. The Stern–Volmer constant (K_{sv}) was $1.1 \times 10^4\ M^{-1}$. The binding constant was $\log\beta$ = 6.4. The stoichiometry of the complex was 1 : 2 (**43**/Cu^{2+}). One Cu^{2+} coordinates with the nitrogen atom of the imine moiety and the second Cu^{2+} binds to benzyl rings through cation–π interaction.

Moghadam *et al.* designed fluorene-based Schiff base sensor **44** and utilized it for fluorescence-based detection of Cu^{2+} (Fig. 19 and Table 2).[110] Sensor **44** was non-fluorescent in acetonitrile solution. In the presence of Cu^{2+}, sensor **44** showed strong fluorescence enhancement at 369 nm (λ_{ex} = 340 nm). The binding constant was $2.84 \times 10^5\ M^{-1}$ as calculated using the Benesi–Hildebrand equation. The limit of detection was 1.54 nM for Cu^{2+}. Job's plot revealed 1 : 1 (**44**/Cu^{2+}) stoichiometry. The chelation of sensor **44** with Cu^{2+} resulted in the formation of a more rigid system because of blocking of the ICT process and restriction in C═N isomerization, causing turn-on emission through the CHEF effect. Sensor **44** found practical application in the detection of copper in electroplating wastewater.

Torawane *et al.* prepared Schiff base sensor **45** as a turn-off sensor for Cu^{2+} detection (Fig. 19 and Table 2).[111] Among various tested metal ions, sensor **45** underwent instant fluorescence quenching only with Cu^{2+} at emission wavelength 554 nm (λ_{ex} = 386 nm) in an aqueous solution. The detection limit of sensor **45** was 0.35 μM for Cu^{2+}. The association constant was $2.67 \times 10^5\ M^{-1}$ as determined using the non-linear curve fitting method and the binding stoichiometry was 1 : 1 (**45**/Cu^{2+}). The mechanism of sensing could be ascribed to the excited state electron transfer from sensor **45** to Cu^{2+}.

Wang *et al.* synthesized imidazole- and benzimidazole-based Schiff base sensors **46** and **47**, respectively, for Cu^{2+} detection (Fig. 22 and Table 2).[112] In DMF solution, sensors **46** and **47** displayed emission at wavelength 411 nm and 416 nm, respectively. Both sensors **46** and **47** exhibited specificity for Cu^{2+} over other tested metal ions and underwent fluorescence enhancement with Cu^{2+}. The detection limit of Sensor **47** was 1 nM for Cu^{2+}. The coordination of Cu^{2+} with sensors **46** and **47** through the –C═N– group and the imidazole ring resulted in the formation of a rigid structure and caused fluorescence enhancement through the CHEF effect. On comparison, sensor **47** was found to be more selective than sensor **46** for Cu^{2+} because of its large conjugated rigid structure.

Yin *et al.* designed carbazole-based Schiff base sensor **48** for fluorescence-based detection of Cu^{2+} in acetonitrile solution (Fig. 22 and Table 2).[113] On excitation at 298 nm, sensor **48** displayed weak emission at wavelength 335 nm and 381 nm. Among various tested metal ions, sensor **48** showed strong fluorescence enhancement only with Cu^{2+}. On gradual addition of an increasing concentration of Cu^{2+}, sensor **48** displayed an increase in fluorescence intensity at 450 nm and reached a plateau after the addition of 6 equivalents of Cu^{2+}. The binding

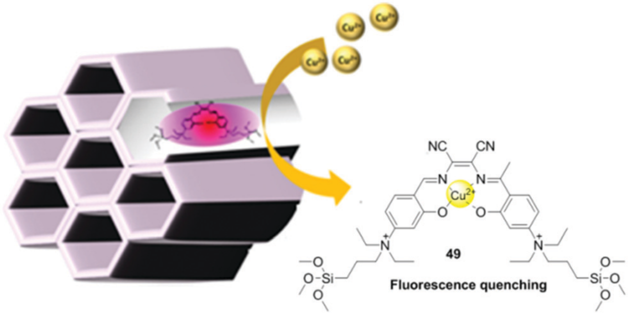

Fig. 21 Chemical structure of Schiff base **49** and the sensing mechanism of Cu^{2+} with **49**-PMO. Reproduced with permission from ref.114 Copyright 2021, Wiley.

constant (K_a) was 1.26×10^{-6} M^{-1} and the binding stoichiometry was 1 : 1 (**48**/Cu^{2+}). The detection limit was 27.4 nM for Cu^{2+}. The sensing mechanism could be ascribed to the coordination of Cu^{2+} with sensor **48** through the diaminomalenonitrile unit, causing inhibition of the ICT process and C═N isomerization, resulting in fluorescence enhancement.

Gao *et al.* incorporated Schiff base-based sensor **49** into the pore of periodic mesoporous organosilica (**49**-PMO) for fluorescence-based detection of Cu^{2+} (Fig. 21 and Table 2).[114] Upon the addition of Cu^{2+}, the fluorescence spectrum of **49**-PMO revealed fluorescence quenching, and the detection limit was 0.67 μM for Cu^{2+}. The sensing mechanism was attributed to ligand to metal charge transfer (LMCT).

3.1.9 Zn^{2+} sensor[240–244]

Zinc is an essential trace element, involved in several important functions in the human body such as metabolism of RNA and DNA, cell apoptosis, reproduction, immune system function, protein metabolism, *etc.*[245] Deficiency of zinc results in serious diseases such as growth retardation, a weak immune system, Parkinson's disease, Alzheimer's disease, *etc.* On the other hand, excess intake of zinc may lead to health problems.[246–248] In addition, zinc is an important pollutant of the environment, having toxic effects on aquatic microorganisms, plants, and invertebrates. Therefore, environmental monitoring and detection of zinc in a biological system constitute an interesting and challenging field of research.

Zhu *et al.* developed 2-hydroxy-1-naphthaldehyde and 2-benzylthio-ethanamine based Schiff base sensor **50** for Zn^{2+} detection (Fig. 22 and Table 2).[115] In ethanol/HEPES buffer (95/5, v/v) solution, sensor **50** hardly displayed detectable fluorescence (λ_{em} = 450 nm, λ_{ex} = 242 nm). Among various

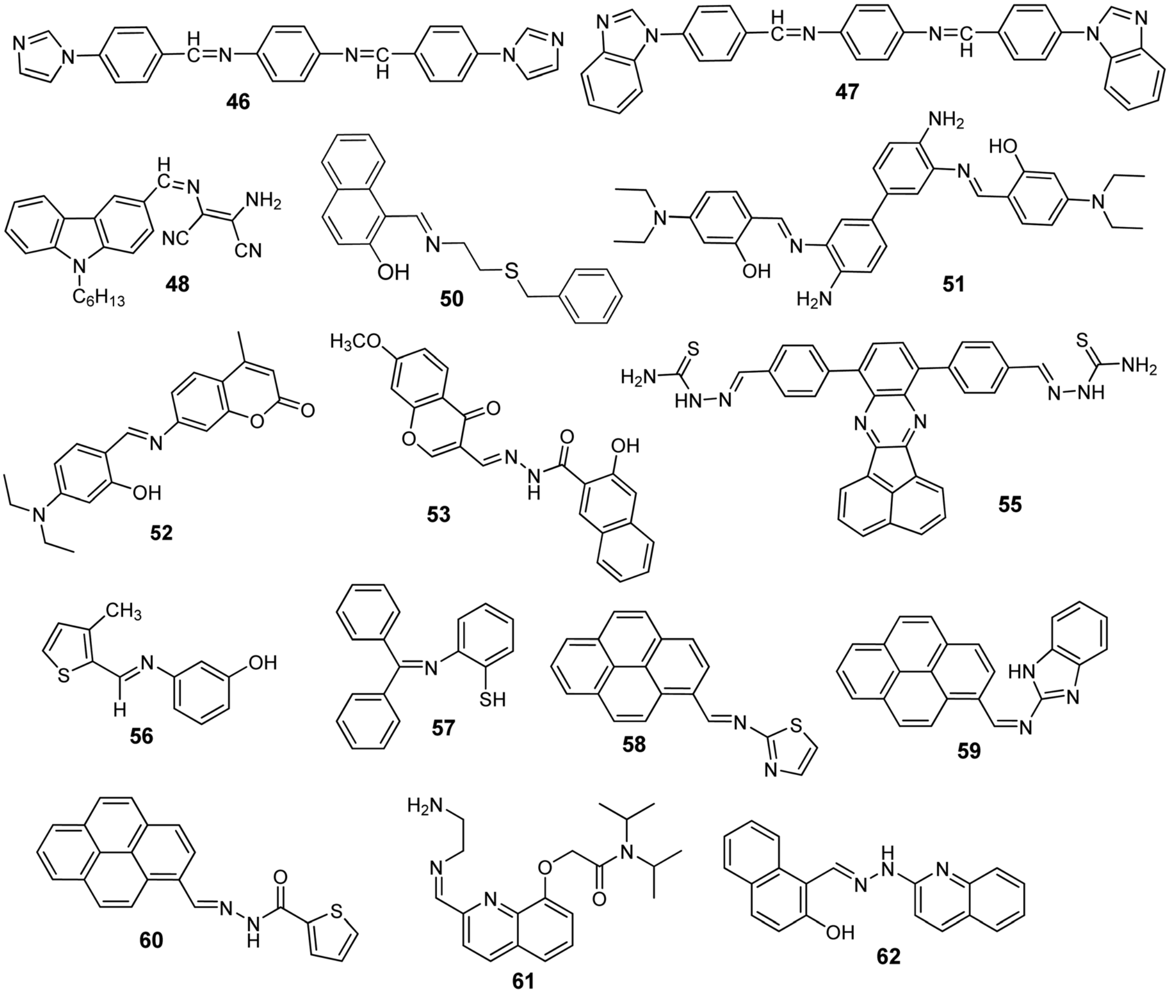

Fig. 22 Chemical structure of sensors **46–62**.

tested metal ions, sensor **50** displayed superb fluorescence enhancement (19-fold) only with Zn^{2+}. The binding stoichiometric ratio was 2 : 1 (**50** : Zn^{2+}) and the binding constant was 85.7 M^{-2}. The detection limit of sensor **50** was 0.5034 μM. The sensing mechanism could be attributed to (i) restriction in rotation of the C═N group, (ii) blockage of the PET process, and (iii) Zn^{2+} induced disaggregation of sensor **50**.

Kumar *et al.* synthesized diaminobenzidine-based Schiff base sensor **51** for Zn^{2+} detection (Fig. 22 and Table 2).[116] In DMF solution, sensor **51** displayed selective fluorescence enhancement only with Zn^{2+} over various other competing metal ions such as Cd^{2+}, Ni^{2+}, Co^{2+}, Cu^{2+}, Mn^{2+}, Fe^{3+}, and Al^{3+}. Fluorescence titration of sensor **51** with Zn^{2+} showed a progressive increase in emission intensity at 509 nm (λ_{ex} = 430 nm). The detection limit was 8.6 nM for Zn^{2+}. Job's plot revealed 1 : 1 (**51**/Zn^{2+}) binding stoichiometry and the binding constant was 7.8×10^4 M^{-1}. The chelation of sensor **51** with Zn^{2+} and inhibition of –C═N– isomerization upon coordination with Zn^{2+} resulted in a turn-on fluorescence response through the CHEF effect.

Qin *et al.* synthesized coumarin-based Schiff base **52** as a two-photon fluorescent sensor for Zn^{2+} detection (Fig. 22 and Table 2).[117] On excitation at 380 nm, sensor **52** displayed weak emission at 500 nm in DMF–H_2O (9 : 1, v/v) solution. Fluorescence titration of sensor **52** with Zn^{2+} showed a gradual increase in fluorescence intensity at 500 nm which reached a plateau after the addition of 0.5 equivalent of Zn^{2+}. The binding stoichiometry was 2 : 1 (**52**/Zn^{2+}) and the binding constant (log *K*) was 6.04. The limit of detection was 2.59 μM for Zn^{2+}. The sensing mechanism could be ascribed to the inhibition of the PET process and restriction in –C═N– isomerization upon coordination of Zn^{2+} with sensor **52**.

Yan *et al.* developed Schiff base sensor **53** for Zn^{2+} detection in ethanol solution (Fig. 22 and Table 2).[118] Among various metal ions under investigation, sensor **53** underwent strong fluorescence enhancement at 498 nm (λ_{ex} = 430 nm) only with Zn^{2+}. The stoichiometry of the complex was 1 : 1 (**53**/Zn^{2+}) and the detection limit was 0.173 μM for Zn^{2+}. The association constant (K_a) was 2.0×10^4 M^{-1} as calculated using the Benesi–Hildebrand equation. The complexation of Zn^{2+} with sensor **53** makes the system more rigid by inhibiting the PET process and C═N isomerization, resulting in fluorescence enhancement through the CHEF effect.

3.1.10 Ag^+ sensor.

Ag^+ is a heavy metal ion and has been widely utilized in various industrial processes such as photography, batteries, and electrical industries. However, intake of Ag^+ directly/indirectly from industrial waste has a toxic impact on living beings. Thus, detection of Ag^+ is important, which is challenging. Recently, thiophene appended cyclotriphosphagene-based sensor **54** has been developed for Ag^+ detection (Fig. 23 and Table 2).[119] Sensor **54** showed a turn-on fluorescence response toward Ag^+ over other competitive metal ions. The coordination of sensor **54** with Ag^+ in a 1 : 1 manner resulted in inhibition of the PET process and the CHEF effect. The LOD was 3.15 μM for Ag^+. Interestingly, sensor **54** found practical application in the determination of Ag^+ in real samples.

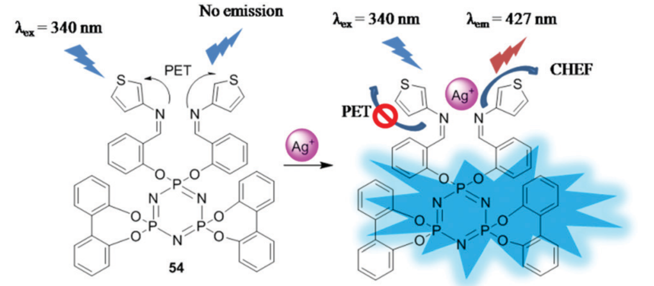

Fig. 23 Sensing mechanism of Ag^+ with sensor **54**. Reproduced with permission from ref.119 Copyright 2021, Wiley-VCH GmbH, Weinheim.

3.1.11 Hg^{2+} sensor[249,250].

Among heavy metal ions, mercury has an extremely toxic impact on living beings and the environment. Exposure to Hg^{2+} can lead to liver, kidney, and brain damage, neurological problems, *etc.* The main sources of mercury contamination are industry and mining activities. Therefore, the detection of mercury in biological systems and the environment is important. Because of the high affinity of mercury for sulfur, chelating agents such as 2,3-dimercapto-1-propanesulfonic acid (DMPS) and dimercaptosuccinic acid (DMSA) have been used for treating acute mercury poisoning.[251] Generally, most of the sensors for mercury ion detection contain sulfur, pyridine, thymine, and quinoline groups as binding sites.

Lei *et al.* synthesized thiosemicarbazone-based Schiff base **55** as an on–off sensor for Hg^{2+} detection in DMSO-buffered water (9/1, v/v) (Fig. 22 and Table 2).[120] Among various metal ions, the fluorescence spectrum of sensor **55** displayed dramatic fluorescence quenching only with Hg^{2+} and to a lesser extent with Cu^{2+}, whereas other metal ions had an insignificant effect on the fluorescence spectrum of sensor **55**. Upon addition of Hg^{2+}, the color of the solution of sensor **55** changed from colorless to light yellow and from yellow-green to light red under natural light and UV lamp illumination, respectively. Fluorescence titration of sensor **55** with Hg^{2+} revealed a decrease in emission intensity at 500 nm (λ_{ex} = 365 nm) along with a red-shift of the emission wavelength by 50 nm. The detection limit was 0.907 μM for Hg^{2+}. Job's plot revealed 1 : 2 (**55**/Hg^{2+}) complex stoichiometry. The complexation constant was 2.51×10^5 M^{-1} as calculated using the Benesi–Hildebrand equation. The downfield shift of protons of the thiosemicarbazone moiety and the low field shift of protons of the benzoquinoxaline moiety in the ^1H NMR titration experiment suggested the involvement of the thiosemicarbazide group and the imine group in coordination with Hg^{2+}.

Singhal *et al.* designed thiophene-based Schiff base **56** as a turn-on sensor for Hg^{2+} detection (Fig. 22 and Table 2).[121] Sensor **56** was weakly fluorescent in methanol/H_2O (8 : 2, v/v) solution. On excitation at 365 nm, sensor **56** showed a turn-on fluorescence response at 503 nm with Hg^{2+}, whereas other tested metal ions had an insignificant effect. The complexation of Hg^{2+} with sensor **56** caused fluorescence enhancement through the CHEF effect. The binding constant as calculated using Hill's method was log β = 13.36 and the limit of detection was 20 μM for Hg^{2+}. The job's plot and ^1H NMR titration experiment revealed 2 : 1 (**56**/Hg^{2+}) binding stoichiometry.

Su *et al.* reported benzophenone and aminobenzenethiol based Schiff base sensor **57** for Hg^{2+} detection (Fig. 22 and Table 2).[122] In the CH_3CN-H_2O (9/1, v/v) mixture, sensor **57** displayed weak fluorescence at 415 nm (λ_{ex} = 349 nm). In the presence of Hg^{2+}, sensor **57** showed an increase in fluorescence intensity at 415 nm along with the formation of a new emission band at 473 nm. The sensing mechanism could be attributed to the inhibition of the ESIPT process and C=N isomerization due to the coordination of Hg^{2+} with sensor **57** through the nitrogen atom and the sulfur atom of the imine group and the thiophenol moiety, respectively, forming a five-membered ring structure. The complex stoichiometry was 2 : 1 (**57**/Hg^{2+}) and the association constant was 4.48 × 10^5 M^{-1} as obtained from the Benesi–Hildebrand method. The limit of detection for Hg^{2+} was 22.68 nM.

Tekuri *et al.* synthesized pyrene-based Schiff base chemodosimeters **58**, **59**, and **60** for Hg^{2+} detection in aqueous medium (Fig. 22 and Table 2).[123] Among sensors **58**, **59**, and **60**, only sensor **58** displayed high selectivity for Hg^{2+} over other tested metal ions. Fluorescence titration of sensor **58** with Hg^{2+} exhibited an increase in fluorescence intensity at 417 nm (λ_{ex} = 355 nm). The binding constant was 5.8 × 10^{-2} M^{-1} and the complex stoichiometry was 2 : 1 (**58**/Hg^{2+}). The limit of detection was 0.270 μM for Hg^{2+}. The sensing mechanism could be ascribed to the Hg^{2+} induced hydrolysis of sensor **58** resulting in the formation of more fluorescent pyrene carboxyaldehyde molecules.

3.1.12 Cd^{2+} sensor[35,124,252,253].

Cadmium is an extremely hazardous metal ion that is widely utilized in industrial processes, for example in electroplating, fabrication of batteries, *etc.* Human exposure to Cd^{2+} may occur through industrial discharge and excessive use of fertilizers. Inside the human body, Cd^{2+} may damage the respiratory system, liver, kidney, *etc.*[11] Therefore, detection of cadmium ions in biological fluids (such as blood samples and urine samples) and in real samples (such as water and food) is important for early identification of cadmium poisoning.

Wan *et al.* utilized quinoline-based Schiff base sensor **61** for Cd^{2+} detection (Fig. 22 and Table 2).[124] In 10% methanol solutions, sensor **61** displayed high selectivity only for Cd^{2+} among various other metal ions. In the presence of Cd^{2+}, sensor **61** showed a 40 times increase in fluorescence intensity at 425 nm (λ_{ex} = 246 nm). The limit of detection was 2.7 nM for Cd^{2+}. Job's plot revealed 1 : 1 (**61** : Cd^{2+}) stoichiometry. ^1H NMR analysis of sensor **61** in the presence and absence of Cd^{2+} demonstrated the participation of –C=N–, quinoline, the nitrogen atom of ethylenediamine, and the oxygen atom of ester in complexation with Cd^{2+}.

Mohanasundaram *et al.* synthesized quinoline-based Schiff base sensor **62** for Cd^{2+} detection (Fig. 22 and Table 2).[125] In CH_3CN–H_2O (8 : 2, v/v) solution, free sensor **62** showed weak emission at 510 nm (λ_{ex} = 380 nm). Among various tested metal ions, sensor **62** underwent fluorescence enhancement only with Cd^{2+} (37-fold) and Zn^{2+} (14-fold), whereas other metal ions had an insignificant effect. Sensor **62** also exhibited color change from colorless to yellow under UV light illumination. The binding stoichiometry was 2 : 1 (**62**/Cd^{2+}) and the association constant was 1.77 × 10^5 M^{-1}. The limit of detection was 14.8 nM for Cd^{2+}. The coordination mechanism of sensor **62** with Cd^{2+} could be the combined effect of restriction in C=N isomerization and the CHEF effect. Furthermore, sensor **62** demonstrated potential application in the quantification of Cd^{2+} in different water samples.

3.2 Multi-metal ion sensors[57,254–264]

Nowadays, the development of sensors with multiple ion recognition sites is a challenging and emerging area of interest, because of the advantages of such systems such as cost reduction and faster analytical processing.

Hammud *et al.* synthesized Schiff base sensor **63** for fluorescence-based detection of Ag^+, Cu^{2+}, and Fe^{3+} in ethanol solution (Fig. 24 and Table 2).[126] On excitation at 341 nm, sensor **63** exhibited strong fluorescence at emission wavelength 385 nm. Fluorescence titration of sensor **63** with Ag^+, Cu^{2+}, and Fe^{3+} revealed a linear decrease in fluorescence intensity with the addition of an increasing concentration of these ions. The detection limit was 0.132 μM, 0.088 μM, and 0.037 μM, respectively, for Ag^+, Cu^{2+}, and Fe^{3+}. The Stern–Volmer constant (K_{sv}) value was 9.575 × 10^2 M^{-1}, 8.273 × 10^2 M^{-1} and 23.2 × 10^2 M^{-1} for Ag^+, Cu^{2+}, and Fe^{3+}, respectively. The stoichiometry of the complex was 2 : 1 (**63**/Ag^+ or Cu^{2+}) and 1 : 2 (**63**/Fe^{3+}). The Benesi–Hildebrand plot revealed a binding constant value of 1.4062 × 10^3 M^{-1}, 1.111 × 10^3 M^{-1} and 1.2909 × 10^4 M^{-1} with Ag^+, Cu^{2+}, and Fe^{3+}, respectively. The mechanism of fluorescence quenching could be attributed to the initiation of the PET process upon binding with metal ions. Sensor **63** found analytical application in the detection of Ag^+, Cu^{2+}, and Fe^{3+} in real water samples.

Saleem *et al.* developed triazole-based Schiff base sensor **64** for fluorescence-based detection of Co^{2+}, Cu^{2+}, and Hg^{2+} (Fig. 24 and Table 2).[127] In THF/water (6 : 4, v/v) solution, sensor **64** displayed emission at 622 nm (λ_{ex} = 259 nm). Among various metal ions, sensor **64** exhibited strong fluorescence quenching only with Hg^{2+} and to a lesser extent with Co^{2+} and Cu^{2+}, whereas other metal ions had an insignificant effect. The quenching constant (K_{sv}) value was 9.25 × 10^7, 1.829 × 10^7 and 1.14 × 10^7 M^{-1} for Co^{2+}, Cu^{2+}, and Hg^{2+}, respectively. The association constant value was 1.52 × 10^8 M^{-1}, 5.47 × 10^{11} M^{-1}, and 1.16 × 10^8 M^{-1} for Co^{2+}, Cu^{2+}, and Hg^{2+}, respectively. The limit of detection was 3.26 nM, 89.1 pM, and 0.387 nM for Co^{2+}, Cu^{2+}, and Hg^{2+}, respectively. The stoichiometry of the complex was 1 : 1 (**64** : Co^{2+}/Cu^{2+}/Hg^{2+}). The heavy metal ion effect and paramagnetic behavior triggered non-radiative decay could be responsible for the observed fluorescence quenching.

Sie *et al.* synthesized Schiff base sensor **65** for fluorometric and colorimetric detection of Co^{2+}, Cu^{2+}, and Hg^{2+} (Fig. 24, 25 and Table 2).[128] In DMSO–H_2O (9 : 1, v/v) solution, sensor **65** exhibited emission at wavelength 540 nm (λ_{ex} = 460 nm). The fluorescence titration of sensor **65** with Hg^{2+} showed first a

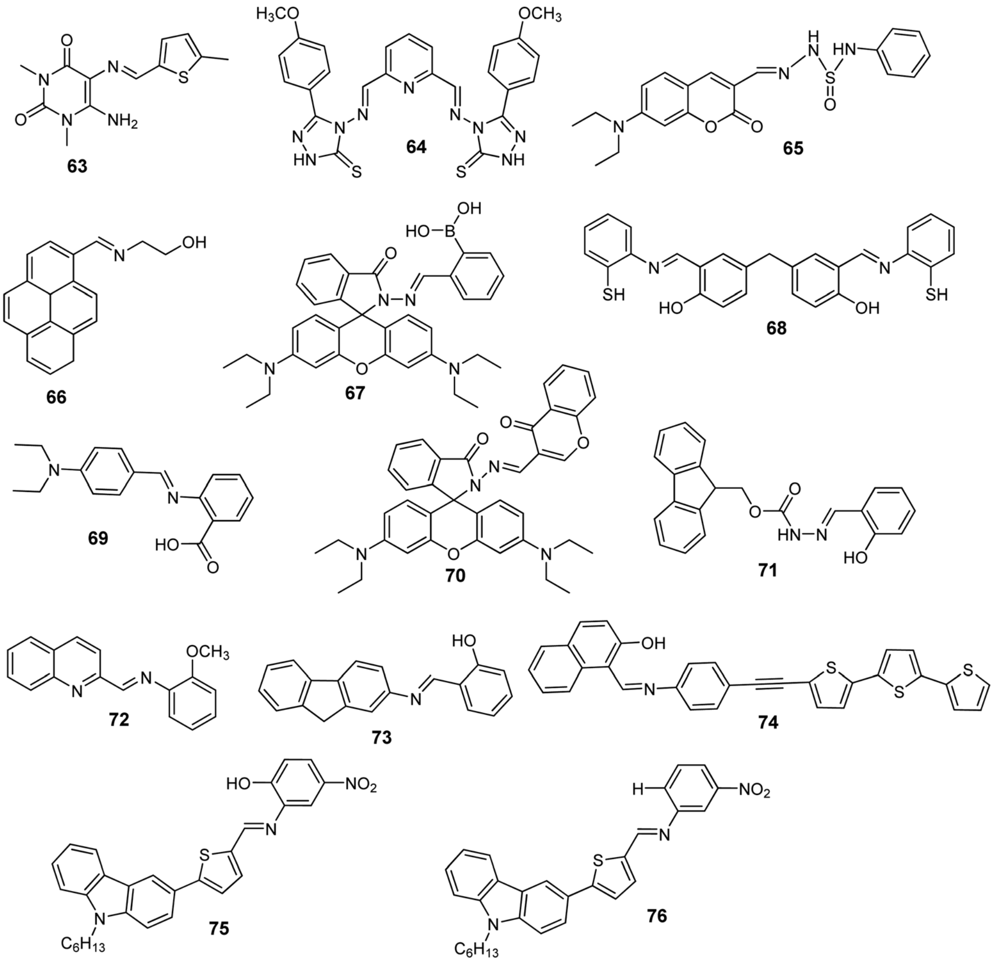

Fig. 24 Chemical structure of sensors **63–76**.

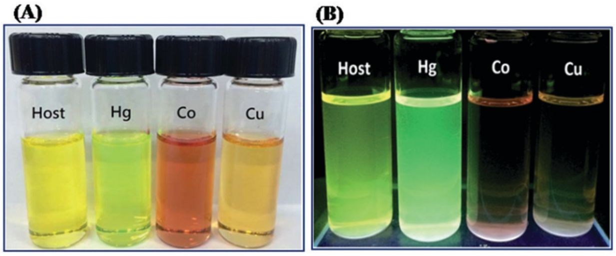

Fig. 25 Color change of sensor **65** (host) upon addition of Hg^{2+}, Co^{2+}, and Cu^{2+} (5 equiv.): (A) naked eye detectable color change; (B) under UV light illumination. Reproduced with permission from ref. 128 Copyright 2017, Royal Society of Chemistry.

decrease (4–12 μM), then an increase (16–40 μM), and again a gradual decrease (60–800 μM) in emission intensity with the addition of an increasing concentration of Hg^{2+}. Coordination and desulfurization could be the possible mechanism of the observed fluorescence change of sensor **65** with Hg^{2+}. Upon addition of an increasing concentration of Co^{2+} or Cu^{2+}, sensor **65** showed a decrease in emission intensity at 540 nm. The disruption of the intramolecular H-bond in the presence of Co^{2+} or Cu^{2+} could be responsible for the observed fluorescence quenching. The association constant was 3.52×10^{6} M^{-1}, 5.69×10^{5} M^{-1}, and 1.85×10^{4} M^{-1}, respectively, for Co^{2+}, Cu^{2+}, and Hg^{2+}. The stoichiometry of the complex was 1 : 1 (**65** : Co^{2+}/Cu^{2+}/Hg^{2+}). The limit of detection was 0.007 ppb, 0.29 ppb, and 0.20 ppb, respectively, for Co^{2+}, Cu^{2+}, and Hg^{2+}. Sensor **65** showed potential for Co^{2+}, Cu^{2+}, and Hg^{2+} detection in real water samples.

Simon *et al.* developed pyrene-based Schiff base **66** as an off–on sensor for Al^{3+}, Cr^{3+}, and Fe^{3+} in acetonitrile solution (Fig. 24 and Table 2).[129] Among various metal ions, sensor **66** showed turn-on fluorescence response only with trivalent metal ions such as Al^{3+}, Cr^{3+}, and Fe^{3+} along with red-shift of the emission maxima from 417 nm to 500 nm (λ_{ex} = 355 nm). The complexation stoichiometry was 2 : 1 (**66** : Al^{3+}/Cr^{3+}/Fe^{3+}). The association constant value was 2.26×10^{6} M^{-2}, 2.24×10^{6} M^{-2} and 2.25×10^{6} M^{-2} for Al^{3+}, Cr^{3+}, and Fe^{3+} ions, respectively. The detection limits were 0.117 μM, 0.111 μM, and 0.106 μM for Al^{3+}, Cr^{3+}, and Fe^{3+}, respectively. The turn-on sensing mechanism was explained by means of excimer formation and the PET process. Sensor **66** found application in Al^{3+}, Cr^{3+}, and Fe^{3+} detection in living cells.

Tang *et al.* synthesized rhodamine B derivative-based Schiff base sensor **67** for Zn^{2+}, Fe^{3+}, and Cu^{2+} (Fig. 24 and Table 2).[130] In ethanol solution, sensor **67** displayed fluorescence enhancement (λ_{ex} = 510 nm) at 572 nm (125-fold) and at 580 nm (150-fold) along with a change in the fluorescence color of the solution from colorless to orange with Zn^{2+} and from colorless to red with Fe^{3+}, respectively, whereas other metal ions had an insignificant effect (Fig. 26A and B). In ethanol–H_2O (1 : 1, v/v) solution, sensor **67** behaved as a colorimetric sensor for Cu^{2+} with a naked-eye detectable color change of the solution from colorless to pink. Job's plot revealed a complexation ratio of 1 : 1 (**67**/Zn^{2+}), 2 : 1 (**67**/Fe^{3+}) and 1 : 1 (**67**/Cu^{2+}). The binding constant was 1.53×10^3 M^{-1}, 4.57×10^4 M^{-1} and 2.62×10^3 M^{-1} for Zn^{2+}, Fe^{3+}, and Cu^{2+}, respectively. The detection limit was 0.664 μM, 0.212 μM and 82.7 nM for Zn^{2+}, Fe^{3+}, and Cu^{2+}, respectively. The turn-on response could be attributed to the opening of the lactam ring of sensor **67** upon binding with Zn^{2+} and Fe^{3+}, leading to the formation of a more conjugated system. However, in the case of Cu^{2+}, the naked-eye detectable color change could be due to electron transfer from Cu^{2+} to sensor **67**. Sensor **67** found application in Zn^{2+}, Fe^{3+}, and Cu^{2+} detection in real water samples and in the fluorescence imaging of Fe^{3+} in biological cells.

Zhang *et al.* developed Schiff base sensor **68** for colorimetric and fluorometric detection of Cu^{2+}, Hg^{2+}, and Ag^{+} (Fig. 24 and Table 2).[131] In DMSO–H_2O (1 : 1, v/v) solution, sensor **68** showed emission maxima at 527 nm (λ_{ex} = 310 nm). In the presence of Cu^{2+}, Hg^{2+}, and Ag^{+}, sensor **68** displayed fluorescence quenching along with a red-shift of the emission maxima from 527 to 550 nm. The binding ratio was 1 : 2 (**68** : Cu^{2+}/Hg^{2+}/Ag^{+}). The plot of fluorescence intensity ratio *vs* the concentration of Cu^{2+}, Hg^{2+}, and Ag^{+} revealed a good linear range between 0 and 20 μM. The detection limit was 64.8 μM, 52.7 μM, and 63.7 μM for Cu^{2+}, Hg^{2+}, and Ag^{+}, respectively. The association constant value was 1.64×10^5 M^{-1}, 9.27×10^4 M^{-1}, and 1.37×10^5 M^{-1} for Cu^{2+}, Hg^{2+}, and Ag^{+}, respectively, as calculated using the Benesi–Hildebrand equation. From the FT-IR spectra of complexes [**68**–Cu^{2+}], [**68**–Hg^{2+}], and [**68**–Ag^{+}], a new band at 3462, 3427, and 3437 cm^{-1}, respectively, and the low-frequency shift of $\nu_{C{=}N}$ and $\nu_{C\text{–}S}$, the high-frequency shift of the $\nu_{C\text{–}O}$ stretching band, and disappearance of the $\delta_{O\text{–}H}$ band indicated coordination of Cu^{2+}, Hg^{2+}, and Ag^{+} with sensor **68** through the nitrogen atom of the imine group, the sulfur atom of thiol and the oxygen atom of the phenolic hydroxyl group.

Zhu *et al.* developed Schiff base sensor **69** for Fe^{2+}, Fe^{3+} and Cu^{2+} detection in DMF solution (Fig. 24 and Table 2).[132] Among various metal ions, sensor **69** showed selectivity only for Fe^{2+}, Fe^{3+}, and Cu^{2+} and naked eye detectable color change from colorless to yellow with Cu^{2+} and colorless to light brown with Fe^{2+} and Fe^{3+}, and fluorescence color change from purple to colorless with Fe^{2+}, Fe^{3+}, and Cu^{2+} under UV light. On excitation at 341 nm, sensor **69** displayed emission at wavelength 393 nm. In the presence of Fe^{2+}, Fe^{3+}, and Cu^{2+}, sensor **69** underwent fluorescence quenching (∼98% with Fe^{2+} and Fe^{3+} and ∼92% with Cu^{2+}). The fluorescence quenching mechanism could be attributed to the CHEQ effect of paramagnetic Fe^{2+}, Fe^{3+}, and Cu^{2+}. The detection limit was 2.06 μM, 2.17 μM, and 2.48 μM for Fe^{2+}, Fe^{3+}, and Cu^{2+}, respectively. Job's plot revealed 1 : 1 (**69** : Fe^{2+}/Fe^{3+}/Cu^{2+}) stoichiometry. The association constant value was 3.61×10^5 M^{-1}, 3.82×10^5 M^{-1}, and 3.93×10^5 M^{-1} for Fe^{2+}, Fe^{3+}, and Cu^{2+}, respectively.

Xue *et al.* developed rhodamine-chromone-based Schiff base sensor **70** for Zn^{2+} and Fe^{3+} detection (Fig. 24 and Table 2).[133] In ethanol-HEPES buffer (9 : 1, v/v) solution, sensor **70** showed 66-fold fluorescence enhancement at 490 nm (λ_{ex} = 420 nm) with Zn^{2+} over other tested metal ions. In contrast, in DMSO–ethanol (2/3, v/v) solution, sensor **70** exhibited 51-fold fluorescence enhancement at 583 nm (λ_{ex} = 520 nm) with Fe^{3+} over other metal ions. The fluorescence responses of sensor **70** with Zn^{2+} could be due to inhibition of the PET process and the CHEF effect. The fluorescence enhancement at 583 nm could be due to the opening of the spirolactam ring of rhodamine upon coordination with Fe^{3+}. The complexation stoichiometry was 1 : 1 (**70** : Zn^{2+}/Fe^{3+}). The limit of detection was 0.134 μM and

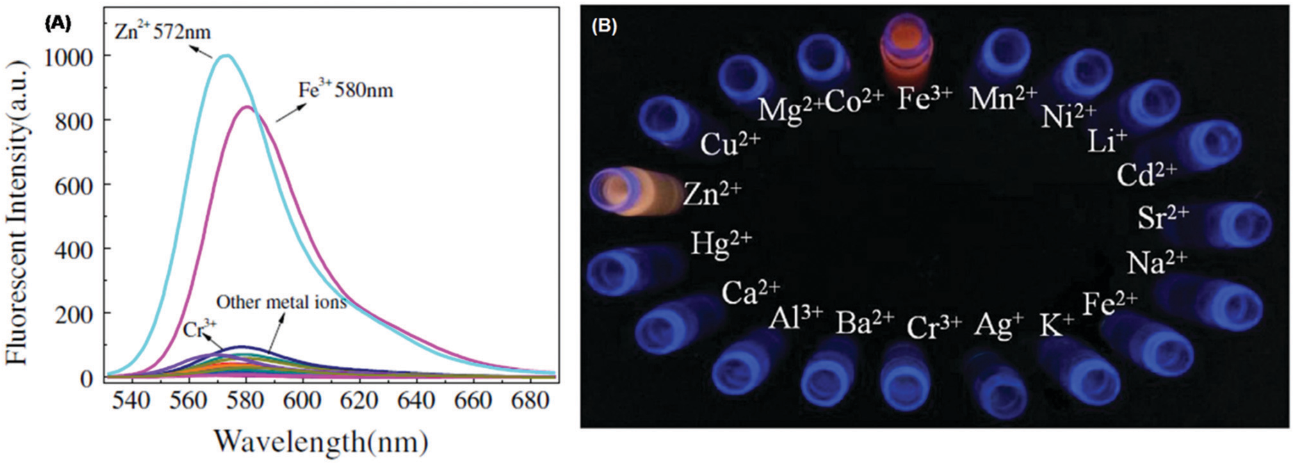

Fig. 26 Fluorescence change of sensor **67** in the presence of various tested metal ions: (A) emission spectrum; (B) visible color change under 365 nm UV lamp irradiation. Reproduced with permission from ref. 130 Copyright 2017, Elsevier.

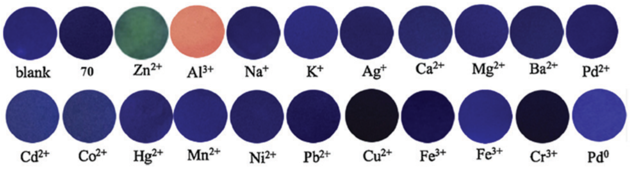

Fig. 27 Photographs of test strips coated with sensor **70** and after addition of different metal ions under 365 nm UV lamp irradiation. Reproduced with permission from ref. 133 Copyright 2019, Elsevier.

0.139 μM for Zn^{2+} and Fe^{3+}, respectively. The binding constant was 5.82 × 10^4 M^{-1} and 5.85 × 10^3 M^{-1} for Zn^{2+} and Fe^{3+}, respectively. A test strip coated with sensor **70** displayed yellow-green color with Zn^{2+} and pink color with Al^{3+}, demonstrating the application of sensor **70** as a solid-state sensor (Fig. 27).

Lee *et al.* developed salicylaldehyde- and fluorene-based Schiff base sensor **71** for fluorescence-based detection of Zn^{2+} and Ga^{3+} (Fig. 24 and Table 2).[134] In acetonitrile solution, free sensor **71** was weakly fluorescent. Compared with other tested metal ions, sensor **71** (λ_{ex} = 300 nm) exhibited fluorescence enhancement with Zn^{2+} and Ga^{3+} at 460 nm and 434 nm, respectively. The binding ratio was 1 : 1 (**71** : Zn^{2+}/Ga^{3+}). The binding constant was 7.0 × 10^4 M^{-1} and 1.0 × 10^4 M^{-1} for Zn^{2+} and Ga^{3+} ions, respectively. The limit of detection was 0.32 μM and 0.01 μM for Zn^{2+} and Ga^{3+}, respectively. The turn-on fluorescence response of sensor **71** with Zn^{2+} and Ga^{3+} could be due to the suppression of the PET process.

Dong *et al.* developed quinoline-based Schiff base **72** as a turn-on sensor for Zn^{2+} and Hg^{2+} (Fig. 24 and Table 2).[135] In the DMSO–H_2O (1 : 99, v/v) mixture, sensor **72** showed weak emission at 473 nm (λ_{ex} = 350 nm). Among various metal ions, sensor **72** exhibited turn-on response with red-shift of the emission maxima from 473 to 539 ($\Delta\lambda_{shift}$ = 57 nm) with Hg^{2+}, and from 473 to 565 nm ($\Delta\lambda_{shift}$ = 92 nm) with Zn^{2+}, whereas other metal ions had an insignificant effect. Under UV light, sensor **72** displayed color change from colorless to yellowish-green with Hg^{2+}, and from colorless to intense yellow with Zn^{2+} (Fig. 28A and B). Job's plot indicated 1 : 1 (**72** : Hg^{2+}/Zn^{2+}) stoichiometry. The limit of detection was 0.040 μM and 0.011 μM for Hg^{2+} and Zn^{2+}, respectively. The association constant was 1.41 × 10^5 M^{-1} and 1.52 × 10^5 M^{-1} for Hg^{2+} and Zn^{2+}, respectively. The sensing mechanism could be attributed to the lowering of the energy gap between HOMO and LUMO of sensor **72** as well as increased structural rigidity upon complexation with Hg^{2+} and Zn^{2+}.

Tajbakhsh *et al.* developed fluorene-based Schiff base **73** as a turn-on sensor for Al^{3+} and Cr^{3+} (Fig. 24 and Table 2).[136] In acetonitrile solution, sensor **73** exhibited emission at 536 nm (λ_{ex} = 333 nm). In the presence of Al^{3+} or Cr^{3+}, sensor **73** displayed fluorescence enhancement at 536 nm. The binding ratio was 2 : 1 (**73** : Al^{3+}/Cr^{3+}) and the binding constant was 5.44 × 10^4 M^{-1} and 8.33 × 10^4 M^{-1} for Al^{3+} and Cr^{3+} ions, respectively. The detection limit was 0.31 μM and 0.25 μM for Al^{3+} and Cr^{3+}, respectively. The chelation of sensor **73** with Al^{3+} and Cr^{3+} resulted in inhibition of C=N isomerization and the ESIPT process, causing fluorescence enhancement (Fig. 29).

Zhang *et al.* developed phenylamine-oligothiophene-based Schiff base sensor **74** for fluorescence-based detection of Cu^{2+} and Zn^{2+} (Fig. 24 and Table 2).[137] In THF–H_2O (7 : 3, v/v) solution, sensor **74** displayed emission at 537 nm (λ_{ex} = 385 nm). Compared with other metal ions, sensor **74** exhibited a turn-off response with Cu^{2+} and a turn-on response with Hg^{2+}. Under 365 nm UV light, the fluorescence color of sensor **74** changed from light green to dark green (with Cu^{2+}), and to bright yellow-green (with Hg^{2+}). The binding stoichiometry was 1 : 1 (**74** : Cu^{2+}/Hg^{2+}). The association constant was 9.40 × 10^4 M^{-1} and 8.69 × 10^4 M^{-1} for Cu^{2+} and Zn^{2+}, respectively. The detection limit was 70.6 nM and 0.116 μM for Cu^{2+} and Zn^{2+}, respectively. The turn-on fluorescence response of sensor **74** with Hg^{2+} could be due to inhibition of the PET process upon coordination and the CHEF effect. The turn-off fluorescence response of sensor **74** with Cu^{2+} could be ascribed to paramagnetic characteristics of Cu^{2+} and the ICT process, resulting in the CHEQ effect (Fig. 30).

Zhu *et al.* synthesized carbazole-based Schiff base sensors **75** and **76** for Fe^{3+} and Cr^{3+} detection in acetonitrile solution (Fig. 24 and Table 2).[138] Among various metal ions, sensor **75** displayed significant fluorescence enhancement selectively

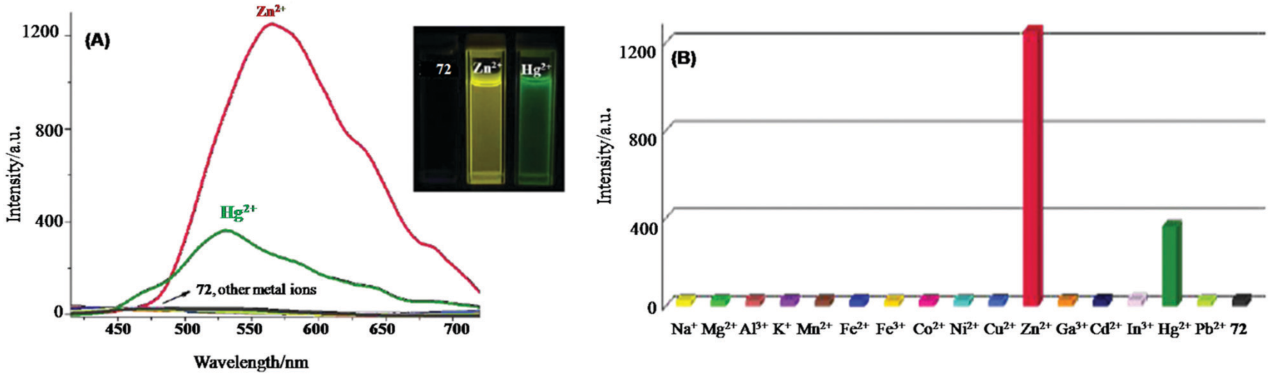

Fig. 28 Fluorescence change of sensor **72** in the absence and presence of different metal ions: (A) emission spectrum; (B) plot of fluorescence intensity change. Inset: Photographs of sensor **72**, **72** + Zn^{2+} and **72** + Hg^{2+} under 365 nm UV lamp irradiation. Reproduced with permission from ref. 135 Copyright 2017, Royal Society of Chemistry.

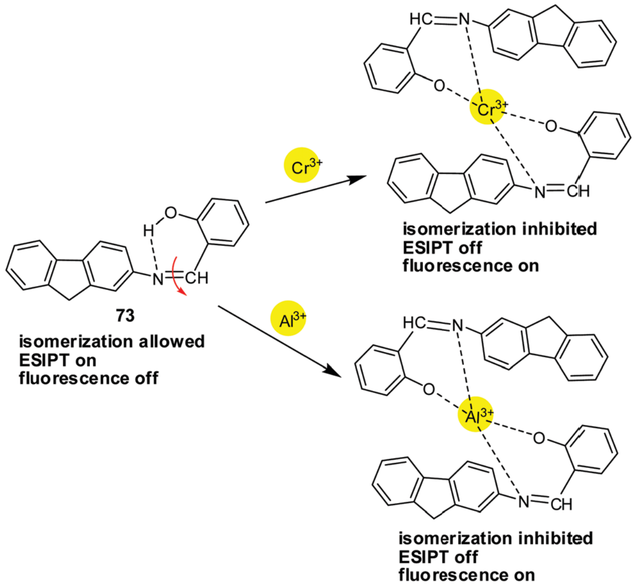

Fig. 29 Sensing mechanism of sensor **73** with Al^{3+}. Reproduced with permission from ref. 136 Copyright 2018, Elsevier.

with Fe^{3+} and Cr^{3+}, credited to inhibition of the ESIPT process and C=N isomerization. Sensor **75**, without the *o*-OH group, lacks selectivity towards tested metal ions. Fluorescence titration of sensor **75** with Fe^{3+} and Cr^{3+} showed a gradual increase in fluorescence intensity with the increasing concentration of Fe^{3+}/Cr^{3+} at 495 nm (λ_{ex} = 380 nm) along with red-shift from 495 nm to 502 nm. The detection limit was 4.57 μM and 2.75 μM for Fe^{3+} and Cr^{3+}, respectively. The binding stoichiometry was 2 : 1 (**75** : Fe^{3+}/Cr^{3+}) and the association constant was 4.67 × 10^4 M^{-1} and 5.97 × 10^4 M^{-1} for Fe^{3+} and Cr^{3+}, respectively.

3.3 Schiff-base–metal ion ensembles as a sequential sensor for ions[265,266]

Nowadays, researchers are working on the design and synthesis of Schiff-base–metal ion ensembles as a sequential sensor for the detection of various analytes, *viz.* anions, cations, and metal ions. Generally, the interaction of the ensemble with metal ions results in recovery of the original fluorescence of the Schiff base, illustrating the reusability of the Schiff base sensor.

Fu *et al.* developed 8-hydroxyquinoline based Schiff base sensors **77** and **78** for Al^{3+} detection (Fig. 31 and Table 2).[139] In DMSO-H_2O (1 : 2, v/v) solution, both sensors **77** (λ_{ex} = 405 nm) and **78** (λ_{ex} = 455 nm) are non-fluorescent. In the presence of Al^{3+}, sensors **77** and **78** exhibited a 270-fold and 460-fold increase in emission intensity at 505 nm and 509 nm, respectively. The complexation of sensor **77** or **78** with Al^{3+} inhibited the ESIPT process and C=N isomerization and resulted in fluorescence enhancement through the CHEF effect. The binding constant of sensors **77** and **78** with Al^{3+} was 9.40 × 10^4 M^{-1} and the limit of detection was 14.8 nM and 42.3 nM, respectively. The complexation stoichiometry was 1 : 1 (**77**/**78** : Al^{3+}). Further, the **77**–Al^{3+} and **78**–Al^{3+} complexes displayed fluorescence quenching selectively with F^-. The limit of detection of the **77**–Al^{3+} and **78**–Al^{3+} complexes was 0.164 μM and 35.8 nM for F^-, respectively. Both sensors **77** and **78** found practical application in Al^{3+} and F^- detection using filter paper and in the bioimaging of Al^{3+} and F^- in living cells.

Gomathi *et al.* synthesized benzoxazole appended Schiff base **79** for fluorescence-based detection of Zn^{2+} and PPi (Fig. 31 and Table 2).[140] In the DMSO–H_2O (1 : 9, v/v, HEPES buffered) solvent system, sensor **79** showed weak emission maxima at 525 nm (λ_{ex} = 450 nm). On addition of different metal ions to the solution of sensor **79**, no significant change in the fluorescence spectrum was observed, except for Zn^{2+}. Fluorescence titration of sensor **79** with Zn^{2+} displayed a gradual increase in fluorescence intensity with the addition of an increasing concentration of Zn^{2+} and saturation was reached after the addition of 50 μM Zn^{2+}. The binding stoichiometry was 1 : 1 (**79**/Zn^{2+}) and the binding constant was 4.53 × 10^4 M^{-1}. The detection limit was 0.52 μM for Zn^{2+}. Further the sensor **79**–Zn^{2+} ensemble showed significant fluorescence quenching selectively with PPi over other ions. The detection limit of the sensor **79**-Zn^{2+} ensemble was 0.58 μM for PPi and the binding ratio was 1 : 1. Test strips coated with sensor **79** exhibited a greenish-yellow color with Zn^{2+} under UV lamp illumination.

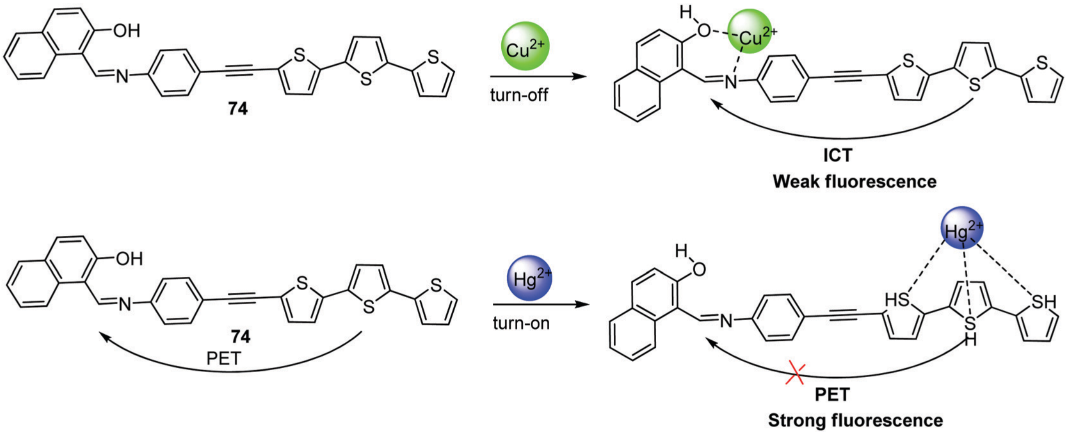

Fig. 30 Sensing mechanism of sensor **74** for Cu^{2+} and Hg^{2+}. Reproduced with permission from ref. 137 Copyright 2017, Elsevier.

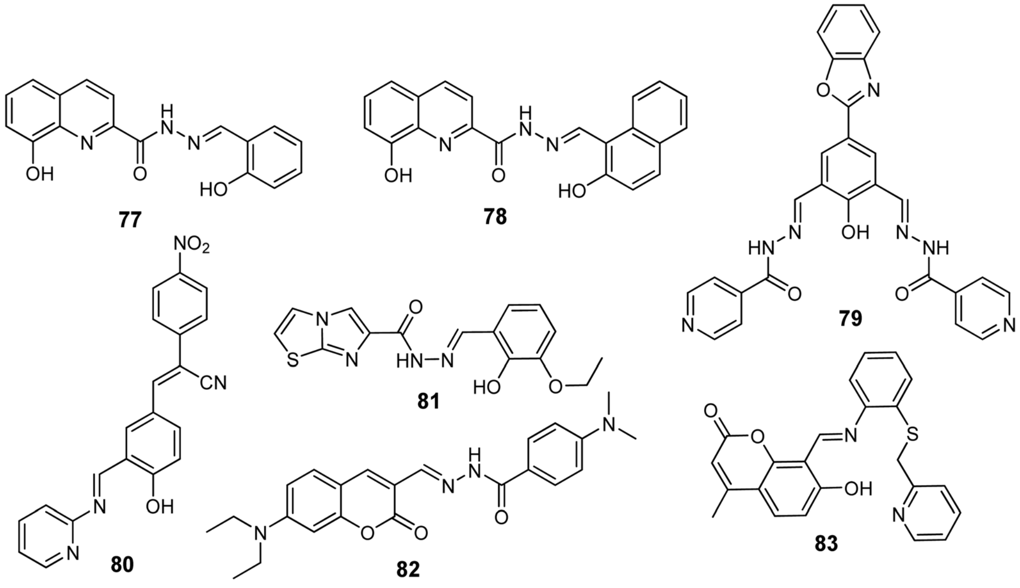

Fig. 31 Chemical structure of chemosensors **77–83**.

Sensor **79** was also applied for monitoring intracellular Zn^{2+} in HeLa cells.

Qiu *et al.* synthesized diphenylacrylonitrile- and pyridine-based Schiff base **80** for fluorescence-based detection of Co^{2+}–Hg^{2+}–Cu^{2+} sequentially (Fig. 31, 32 and Table 2).[141] In the THF–H_2O (1 : 99) mixture, sensor **80** displayed AIE property and red fluorescence at emission wavelength 620 nm (λ_{ex} = 360 nm). Compared with various other tested metal ions, sensor **80** exhibited fluorescence quenching with Co^{2+} and Cu^{2+}, and a slight blue-shift with Ag^+ and Hg^{2+}, whereas other metal ions had an insignificant effect. From the interference experiment, the quenched fluorescence of sensor **80** + Co^{2+} could be recovered with Hg^{2+} addition and quenched again by the addition of Cu^{2+}. The limit of detection was 0.0937 μM, 0.0221 μM, and 0.0988 μM for Co^{2+}, Hg^{2+} and Cu^{2+}, respectively. The binding stoichiometry ratio was 2 : 1 (**80** : Co^{2+}/Hg^{2+}/Cu^{2+}). The binding constant value was 4.06×10^{11} M^{-1}, 2.23×10^{13} M^{-1}, and 2.87×10^{13} M^{-1} for Co^{2+}, Hg^{2+} and Cu^{2+}, respectively. In the ^1H NMR spectra of sensor **80** + Cu^{2+}, the low field shift of CH═N protons and the disappearance of OH group protons suggested the complexation of Cu^{2+} with sensor **80** through nitrogen and oxygen atoms. Sensor **80** found application in test paper detection and bio-imaging of living cells.

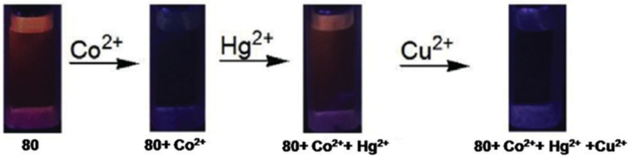

Fig. 32 Photographs of sensor **80** solutions showing sequential detection of Co^{2+}–Hg^{2+}–Cu^{2+} under 365 nm UV light irradiation. Reproduced with permission from ref. 141 Copyright 2019, Elsevier.

Xu *et al.* developed imidazo[2,1-*b*]thiazole-based Schiff base sensor **81** for Zn^{2+} and PPi detection (Fig. 31 and Table 2).[142] In ethanol–H_2O buffered (9 : 1, v/v) solution, sensor **81** showed turn-on fluorescence only with Zn^{2+} as well as a color change of the solution from colorless to yellow-green under a UV lamp, whereas other metal ions displayed insignificant change. Upon gradual addition of an increasing concentration of Zn^{2+} to the solution of sensor **81**, the fluorescence intensity increased gradually with emission maxima at 511 nm (λ_{ex} = 330 nm) and reached a plateau after the addition of 6×10^{-5} M concentration of Zn^{2+}. The binding ratio was 1 : 1 (**81** : Zn^{2+}) and the association constant value was 2.2×10^5 M^{-1}. The lowest detection limit was 1.2 nM for Zn^{2+}. The sensing mechanism could be credited to snapping of the PET process and C═N isomerization upon coordination of sensor **81** with Zn^{2+}, leading to turn-on fluorescence through the CHEF process. The sensor **81**–Zn^{2+} ensemble exhibited fluorescence quenching selectively with PPi over other tested ions. The detection limit of the ensemble was 1.9 nM for PPi. Additionally, INHIBIT type logic gates were constructed using the fluorescence signal of sensor **81** at the molecular level.

Wang *et al.* synthesized coumarin-based Schiff base **82** and utilized it as a fluorometric/colorimetric sensor for Cu^{2+} and glutathione detection (Fig. 31 and Table 2).[143] In H_2O–CH_3CN (1 : 1, v/v) PBS buffered solution, sensor **82** exhibited emission maxima at 521 nm (λ_{ex} = 450 nm). Compared with different metal ions, sensor **82** underwent selective fluorescence quenching (89.8% quenching) with Cu^{2+}, credited to the paramagnetic nature of Cu^{2+} (Fig. 33A). Further, the **82**–Cu^{2+} ensemble showed 9.2-fold fluorescence enhancement with glutathione through the Cu^{2+} displacement approach (Fig. 33B). The lowest detection limit of sensor **82** for Cu^{2+} and the **82**–Cu^{2+} ensemble for glutathione was 24.0 nM and 0.129 μM, respectively. The binding constant was 2.63×10^5 M^{-1} for the 2 : 1 (**82**/Cu^{2+})

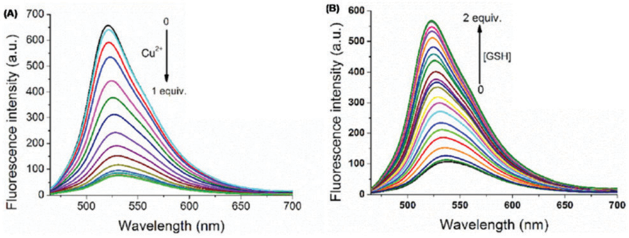

Fig. 33 Fluorescence titration spectrum of (A) sensor **82** with Cu^{2+}; (B) **82** + Cu^{2+} system with GSH. Reproduced with permission from ref. 143 Copyright 2020, Elsevier.

complex. Sensor **82** and the **82**–Cu^{2+} ensemble found application in the bio-imaging of Cu^{2+} and glutathione, respectively, in living cells and zebrafish.

Patra *et al.* synthesized hydroxycoumarin-pyridylthioether-based Schiff base **83** for fluorescence-based detection of Zn^{2+} and ATP (Fig. 31 and Table 2).[144] In methanol–water (3 : 1, v/v) solution, sensor **83** exhibited poor yellow emission at 555 nm (λ_{ex} = 315 nm), assigned to activation of the ESIPT and PET processes. In the presence of Zn^{2+}, sensor **83** displayed ~240 times enhancement in fluorescence along with the blue shift of the emission maxima from 555 nm to 512 nm, credited to inhibition of the ESIPT and PET processes and the CHEF effect. The binding constant was $6.49 \times 10^4\ M^{-1}$ for 1 : 1 (**83**/Zn^{2+}) stoichiometry. Additionally, the **83**–Zn^{2+} ensemble displayed fluorescence quenching selectively with ATP, compared with other anions. The detection limit of sensor **83** and the **83**–Zn^{2+} ensemble for Zn^{2+} and ATP was 0.078 μM and 6.6 μM, respectively. Sensor **83** demonstrated application in bio-imaging and intracellular Zn^{2+} detection in RAW 264.7 cells.

Mehta *et al.* synthesized rhodamine-based Schiff base **84** as a fluorometric sensor for Al^{3+} detection in an aqueous medium (Fig. 34 and Table 2).[145] Upon addition of various metal ions to the solution of sensor **84**, turn-on emission with emission maxima at 588 nm (λ_{ex} = 350 nm) was observed only with Al^{3+} along with the color change of the solution from colorless to bright pink under UV light. Further, the addition of cyanide ions into the solution of the **84**–Al^{3+} ensemble resulted in fluorescence quenching at 588 nm. The limit of detection of sensor **84** and the **84**–Al^{3+} ensemble for Al^{3+} and CN^- was 1.68 μM and 0.815 μM, respectively. The binding constant was $3.98\ mM^{-1}$ for a 1 : 1 (**84**/Al^{3+}) binding ratio. The sensing mechanism could be attributed to Al^{3+} induced hydrolysis of sensor **84**, forming the free –CHO group, and the further nucleophilic attack of CN^- on the free –CHO group of the ensemble resulting in the removal of Al^{3+} and closing of the spirolactam ring by the charge transfer process. Sensor **84** found application in Al^{3+} detection in A549 cells.

Kaur *et al.* synthesized Schiff base sensor **85** for fluorescence-based detection of Cu^{2+} and PO_4^{3-} *via* the complexation/decomplexation approach (Fig. 35 and Table 2).[146] In

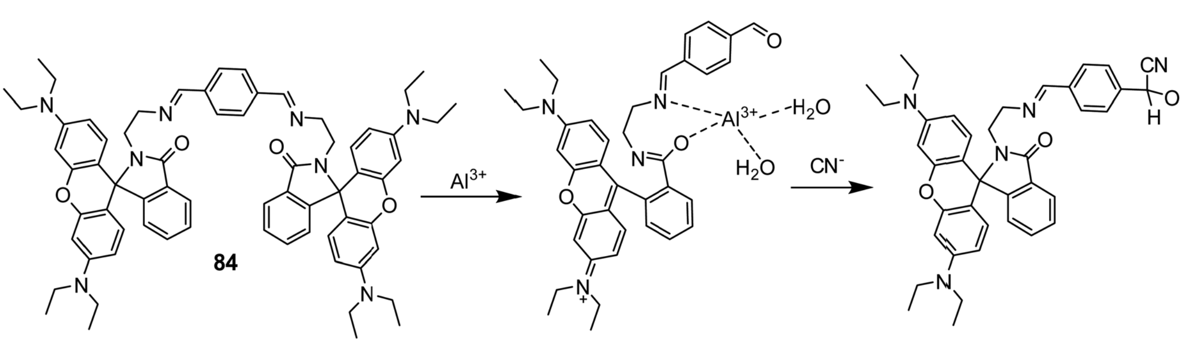

Fig. 34 The binding mechanism of Al^{3+} and CN^- to sensor **84** and the **84**–Al^{3+} complex, respectively. Reproduced with permission from ref. 145 Copyright 2019, Elsevier.

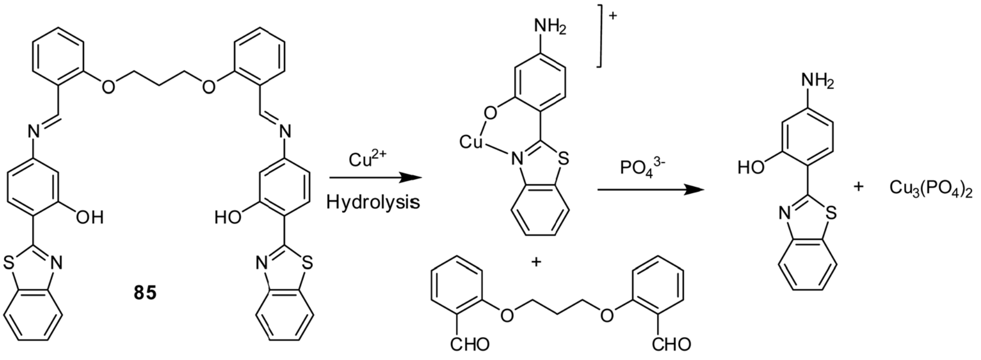

Fig. 35 The sensing mechanism of sensor **85** for the sequential detection of Cu^{2+} and PO_4^{3-}. Reproduced with permission from ref. 146 Copyright 2018, Elsevier.

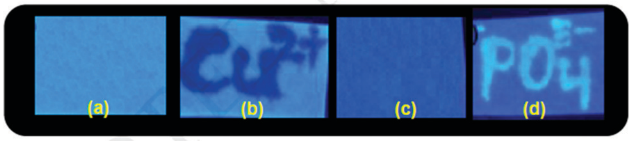

Fig. 36 Photographs of paper strips showing fluorescence change of sensor **85** for the sequential detection of Cu^{2+} and PO_4^{3-} under 365 nm UV light illumination. Reproduced with permission from ref. 146 Copyright 2018, Elsevier.

DMSO–HEPES buffer (4 : 6, v/v) solution, sensor **85** showed fluorescence quenching only with Cu^{2+} over other tested metal ions. Fluorescence titration of sensor **85** with Cu^{2+} (λ_{ex} = 338 nm) revealed a continuous decrease in fluorescence intensity with the addition of an increasing concentration of Cu^{2+}, which reached stabilization after the addition of 73.0 μM Cu^{2+}. The sensing mechanism could be attributed to Cu^{2+} ion-induced hydrolysis of the imine functionality, forming the sensor **85**–Cu^{2+} complex. Furthermore, the addition of PO_4^{3-} to the **85**–Cu^{2+} ensemble solution resulted in turn-on emission at 422 nm *via* the decomplexation process. The detection limit of sensor **85** and the **85**–Cu^{2+} ensemble for Cu^{2+} and PO_4^{3-} was 2.11 ppb and 31.6 ppb, respectively. Sensor **85** demonstrated practical application in Cu^{2+} detection and subsequently PO_4^{3-} detection using paper strips (Fig. 36).

Sheet *et al.* synthesized coumarin-based Schiff base **86** as a light-up probe for Al^{3+} detection (Fig. 37 and Table 2).[147] In 90% aqueous methanol solution, sensor **86** exhibited weak emission at 520 nm (λ_{ex} = 410 nm). Among various metal ions, sensor **86** showed ∼7-fold fluorescence enhancement only with Al^{3+} along with the color change from colorless to bright green under a UV lamp. Fluorescence titration of sensor **86** with Al^{3+} revealed a gradual increase in fluorescence intensity along with the blue shift of the emission maxima from 520 nm to 510 nm (Fig. 38). The binding constant was $(9.9 \pm 0.04) \times 10^3$ M^{-1} for the 1 : 1 (**86**/Al^{3+}) complex. The lowest detection limit was 1.62 μM for Al^{3+}. The complexation of Al^{3+} with sensor **86** makes the system more rigid by inhibiting C=N isomerization, leading to fluorescence enhancement through the CHEF effect. Additionally, the **86**–Al^{3+} ensemble acted like an on–off type fluorescent sensor for biologically important nucleotides and phosphate ions. Sensor **86** also found application in exogenous Al^{3+} detection in living cells.

3.4 Biomedical applications

3.4.1 Fluorescence imaging[267,268]. Fluorescence imaging permits monitoring of various processes in cells, tissues, and organelles in real-time *via* fluorescence microscopy. In the literature, the various instrumental methods for metal ion detection such as atomic absorption spectrometry, inductively coupled plasma mass spectrometry, electrochemical voltammetry, *etc.* when applied in live-cell imaging have resulted in cell damage.[269,270] However, fluorescent sensors proved to be an effective tool for live-cell imaging because of their selective, sensitive, and rapid operation and ability to provide non-damaging images of living cells.

Mu *et al.* developed Schiff base sensor **87** based on carbazole and the triphenylamine unit for Al^{3+} detection (Fig. 39 and Table 2).[148] In ethanol solution, sensor **87** displayed weak fluorescence at 455 nm (λ_{ex} = 400 nm). Upon gradual addition of an increasing concentration of Al^{3+}, sensor **87** underwent an increase in fluorescence intensity along with a red-shift of the emission maxima from 455 nm to 500 nm. The limit of detection was 63.0 nM for Al^{3+}. The stoichiometry of the complex was 2 : 1 (**87**/Al^{3+}). In ^{1}H NMR titration, the appearance of a new peak at 9.83 ppm upon addition of Al^{3+} to the solution of sensor **87** suggested Schiff base hydrolysis and fluorescence enhancement through the CHEF effect. Sensor **87** found potential application in live-cell imaging in living HeLa cells.

Salarvand *et al.* designed and synthesized Schiff base sensor **88** based on 2-hydroxynaphthalene as an off–on sensor for Al^{3+} detection (Fig. 39 and Table 2).[149] In methanol/water (9 : 1, v/v) solution, sensor **88** displayed weak emission at 343 nm (λ_{ex} = 310 nm). Fluorescence titration of sensor **88** with Al^{3+} showed a gradual increase in fluorescence intensity which reached a plateau after the addition of one equivalent of Al^{3+}. The binding stoichiometry was 1 : 1 (**88**/Al^{3+}) and the binding constant was 1.546×10^5 M^{-1} as calculated using the Benesi–Hildebrand equation. The detection limit was 0.64 μM for Al^{3+}. The chelation of sensor **88** with Al^{3+} inhibited the ICT process and C=N isomerization, resulting in fluorescence enhancement through the CHEF effect. Sensor **88** showed no cytotoxicity to living cells as evaluated using MTT assay on MCF-7 cell lines and found potential application in imaging and tracing Al^{3+} in living cells.

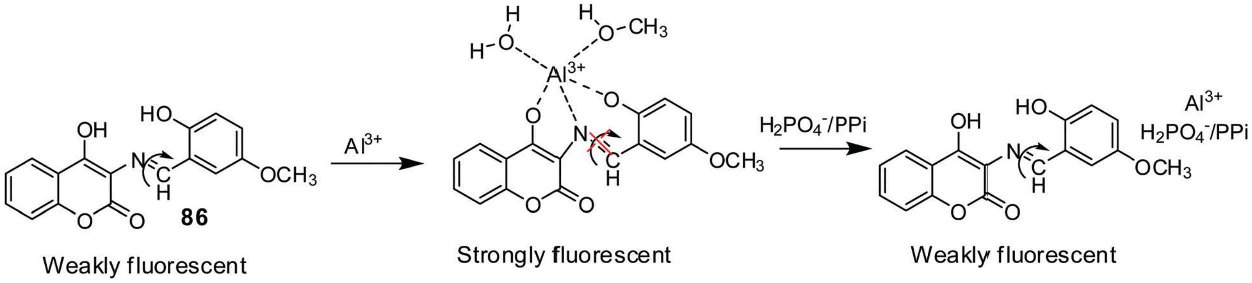

Fig. 37 The binding mechanism of Al^{3+} and $H_2PO_4^-$/PPi to sensor **86** and **86**–Al^{3+}, respectively. Reproduced with permission from ref. 147 Copyright 2017, Elsevier.

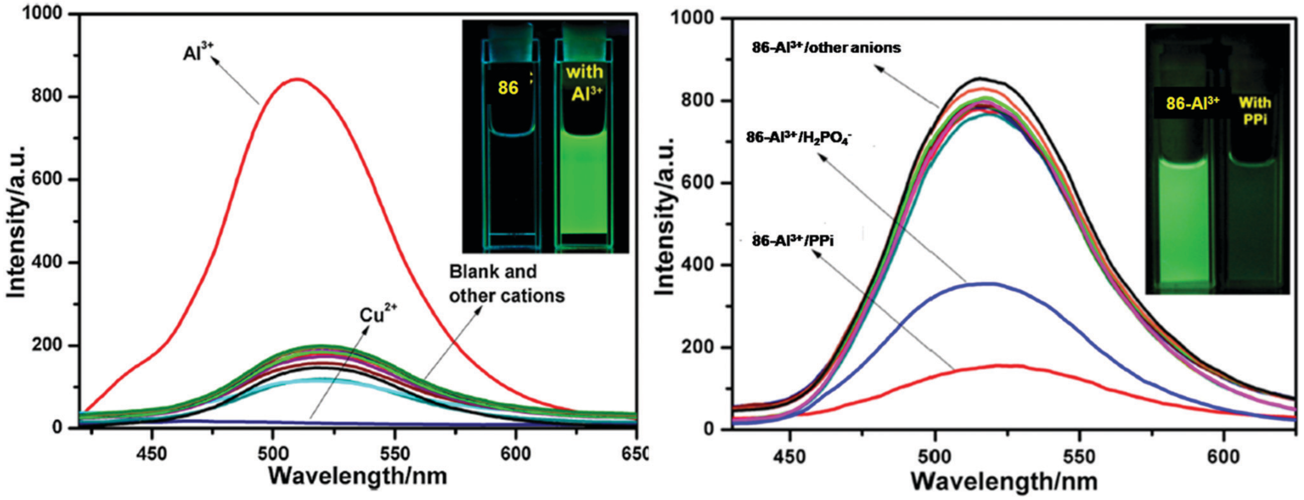

Fig. 38 (A) Fluorescence spectrum of sensor **86** in the absence and presence of different metal ions. Inset: Visible color change of sensor **86** in the absence and presence of Al^{3+}. (B) Fluorescence spectrum of the sensor **86**–Al^{3+} ensemble in the absence (left) and presence (right) of different anions. Inset: visible color change of the sensor **86**–Al^{3+} ensemble in the absence (left) and presence of PPi ions (right). Reproduced with permission from ref. 147 Copyright 2017, Elsevier.

Saravanan *et al.* synthesized pyrene-based sensor **89** and utilized it for fluorescence-based detection of Cu^{2+} inside living cells (Fig. 39 and Table 2).[150] In DMSO–water (1 : 1, v/v) solution, sensor **89** displayed weak emission at 463 nm (λ_{ex} = 393 nm). Upon addition of an increasing concentration of Cu^{2+}, sensor **89** underwent fluorescence enhancement along with red-shift of the emission maxima from 463 nm to 467 nm. Job's plot revealed 1 : 1 (**89**/Cu^{2+}) stoichiometry and the association constant was 1.16 × 10^4 M^{-1}. The detection limit was 0.26 μM for Cu^{2+}. From the DFT calculation, the huge energy difference (−44637.828 eV) between sensor **89** and the sensor **89**–Cu^{2+} (1 : 1) complex suggested strong coordination of sensor **89** with Cu^{2+}. The bioimaging study of sensor **89** in living RAW 264.7 cells showed the good biocompatibility and cell permeability of sensor **89** and proved it to be an excellent biosensor for Cu^{2+} detection inside living RAW 264.7 cells.

Bhanja *et al.* developed vanillinyl-based Schiff base **90** and utilized it for fluorescence-based detection of Zn^{2+} (Fig. 39 and Table 2).[151] In DMSO–water (3/7, v/v) solution, sensor **90** exhibited turn-on fluorescence response only with Zn^{2+} among various other metal ions studied. The fluorescence titration of sensor **90** with Zn^{2+} displayed a significant increase in fluorescence intensity at 472 nm (λ_{ex} = 346 nm), which became saturated after the addition of ∼1.1 equivalent of Zn^{2+}. The binding stoichiometry was 1 : 1 (**90**/Zn^{2+}) and the binding constant was 13.22 × 10^4 M^{-1}. The detection limit was 0.018 μM for Zn^{2+}. The sensing mechanism could be attributed to Zn^{2+} induced deprotonation and the CHEF effect. Sensor **90** found potential application in the examination of Zn^{2+} in living cells (African Monkey Vero cells) by a fluorescence-based cell imaging procedure.

Chen *et al.* synthesized rhodamine-based Schiff base sensors **91**, **92**, and **93** for fluorescence-based detection of Fe^{3+} (Fig. 39 and Table 2).[152] In ethanol–water (1/1, v/v) solution, all the three sensors **91**, **92**, and **93** underwent fluorescence enhancement selectively with Fe^{3+} over various tested metal ions. Among sensors **91**, **92**, and **93**, sensor **91** displayed 1.5-fold higher fluorescence enhancement with Fe^{3+} in comparison with sensors **92** and **93**. The fluorescence titration of sensor **91** with Fe^{3+} displayed a gradual increase in fluorescence intensity at 584 nm (λ_{ex} = 545 nm). The complexation stoichiometry was 1 : 1 (**91**/Fe^{3+}) and the binding constant was 7.66 × 10^4 M^{-1}. The limit of detection was 28.1 nM for Fe^{3+}. The sensing mechanism could be attributed to the opening of the spirolactam ring upon coordination of sensor **91** with Fe^{3+} through the oxygen and nitrogen atom of benzoylhydrazine and the oxygen atom of the oxole unit. Sensor **91** found potential application in Fe^{3+} detection in living cells. SMMC-7721 cells incubated with sensor **91** displayed bright red fluorescence (λ_{ex} = 545 nm) upon the addition of Fe^{3+} (Fig. 40a and b).

Feng *et al.* synthesized coumarin based sensor **94** for Cu^{2+} detection in CH_3CN/PBS (1 : 1, v/v) medium (Fig. 39 and Table 2).[153] On excitation at 450 nm, sensor **94** displayed strong emission at wavelength 540 nm. On gradual addition of an increasing concentration of Cu^{2+}, sensor **94** underwent fluorescence quenching and reached a plateau after the addition of 5 equivalents of Cu^{2+}. In the mass spectrum, the intense peak at *m*/*z* = 454.05 due to $[94 + Cu^{2+}–H]^+$ suggested 1 : 1 binding stoichiometry. Sensor **94** showed good biocompatibility and low cytotoxicity to MCF cells and A549 cells as determined by the CCK8 assay. Sensor **94** found potential application in Cu^{2+} detection in real water samples, and in living cells through confocal microscopy. The A549 cells and MCF-7 cells incubated with sensor **94** displayed strong fluorescence, and when treated with Cu^{2+} showed diminished fluorescence (Fig. 41).

Hu *et al.* reported Schiff base **95** as a two-photon fluorescent sensor for Cu^{2+} detection (Fig. 39 and Table 2).[154] In HEPES

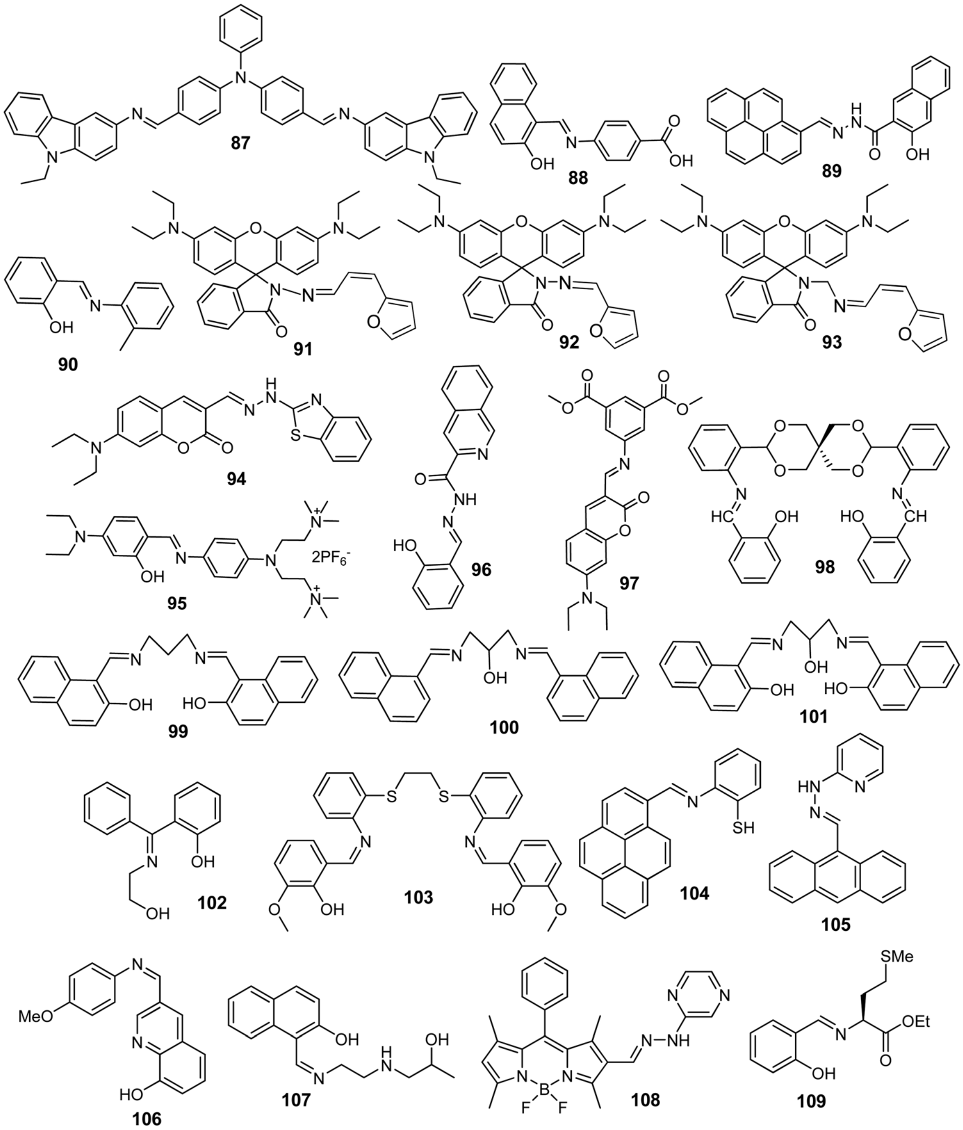

Fig. 39 Chemical structure of sensors **87–109**.

buffer solution, the one-photon fluorescence spectrum of sensor **95** displayed emission at wavelength 516 nm (λ_{ex} = 418 nm). Fluorescence titration of sensor **95** with Cu^{2+} revealed a decrease in emission intensity upon the addition of an increasing concentration of Cu^{2+}. The detection limit was 0.16 μM for Cu^{2+}. The binding stoichiometry was 2 : 1 (**95**/Cu^{2+}) and the binding constant was 1.02×10^{-5} M^{-1}. The coordination of sensor **95** with Cu^{2+} through the nitrogen atom of the imine group and the oxygen atom of the phenolic hydroxyl moiety in a 2 : 1 (**95** : Cu^{2+}) manner resulted in fluorescence quenching as confirmed from ^{1}H NMR titration, mass spectra, and DFT calculations. Sensor **95** found practical application in the two-photon fluorescence imaging of Cu^{2+} in cellular mitochondria and in the liver and intestine of larval zebrafish (Fig. 42).

Huang *et al.* developed isoquinoline-based Schiff base **96** as a turn-on sensor for Al^{3+} detection (Fig. 39 and Table 2).[155] In ethanol solution, sensor **96** displayed a gradual increase in fluorescence intensity at 458 nm (λ_{ex} = 400 nm) with the addition of an increasing concentration of Al^{3+}. The limit of detection was 1.11 nM for Al^{3+}. The binding constant was 2.78×10^6 M^{-1} and the binding stoichiometry was 2 : 1 (**96**/Al^{3+}). The sensing mechanism could be attributed to inhibition of the ESIPT process upon coordination of Al^{3+} with sensor **96.** Sensor **96** found potential application in the examination of intracellular Al^{3+} concentration in cells.

Jiao *et al.* synthesized Schiff base sensor **97** and utilized it as a dual emissive ratiometric fluorescent sensor for Hg^{2+} detection (Fig. 39 and Table 2).[156] In the acetonitrile–water (8 : 2) mixture, sensor **97** was weakly emissive with emission at 530 nm (λ_{ex} = 440 nm) because of the PET process. The fluorescence titration of sensor **97** with Hg^{2+} showed a 20-fold increase in fluorescence intensity (530 nm to 490 nm) upon excitation at 440 nm, and 60-fold fluorescence enhancement (530 nm to 415 nm) upon excitation at 315 nm. The emission

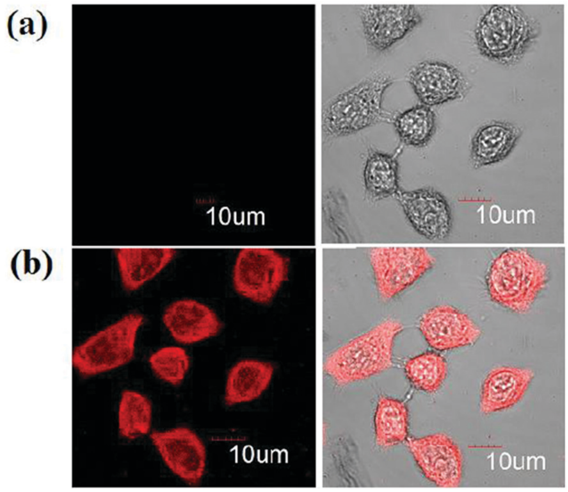

Fig. 40 Confocal fluorescence images of SMMC-7721 cells incubated with sensor **91** in the (a) absence and (b) presence of Fe^{3+}. Reproduced with permission from ref. 152 Copyright 2018, Elsevier.

maxima at 490 nm and 415 nm could be attributed to inhibition of the PET process and hydrolysis of the C=N group following the addition of Hg^{2+}. The detection limit was 1 nM for Hg^{2+}. Sensor **97** displayed potential for Hg^{2+} determination in living cells at nano-molar concentration through confocal microscopy. As shown in Fig. 43, MCF-cells stained with sensor **97** when exposed to Hg^{2+} demonstrated green fluorescence (410–470 nm) and red fluorescence (490–590 nm).

Li *et al.* reported Schiff base **98** as a turn-on sensor for Zn^{2+} (Fig. 39 and Table 2).[157] In buffer solution (ethanol/Tris–HCl, v/v, 4/1), sensor **98** underwent fluorescence enhancement at 458 nm (λ_{ex} = 380 nm) with the addition of an increasing concentration of Zn^{2+} and reached a plateau after the addition of 4 equivalents of Zn^{2+}. The complex stoichiometry was 1 : 1 (**98**/Zn^{2+}) and the binding constant was 4.457 × 10^5 M^{-1} as calculated using the Benesi–Hildebrand equation. The limit of detection was 1.37 μM for Zn^{2+}. The coordination of Zn^{2+} with sensor **98** through imine nitrogen and the oxygen atom of the phenolic group makes the system more rigid by inhibiting C=N isomerization and the PET process, causing turn-on fluorescence through the CHEF effect. Sensor **98** found potential application in Zn^{2+} detection in living cells. The lung cancer A549 cells treated with sensor **98** exhibited a significant fluorescence response to Zn^{2+}.

Liu *et al.* synthesized naphthol-based sensors **99**, **100**, and **101** for Al^{3+} detection (Fig. 39 and Table 2).[158] Among sensors **99**, **100**, and **101**, sensor **101** proved to be the best for Al^{3+} detection over other tested metal ions in CH_3OH/HEPES buffer (3/7, v/v). Fluorescence titration of sensor **101** with Al^{3+} revealed 140-fold fluorescence enhancement at emission wavelength 435 nm (λ_{ex} = 350 nm) upon addition of 1.0 equivalent of Al^{3+}. The stoichiometry of the complex was 1 : 1 (**101**/Al^{3+}) and the binding constant was 1.01 × $10^{6.5}$ M^{-1}. The detection limit was 0.05 μM for Al^{3+}. The sensing mechanism could be attributed to inhibition of C=N isomerization upon coordination of Al^{3+} with sensor **101** through the nitrogen atom of the imine group and the oxygen atom of the –OH group, forming two saturated 5-membered rings and two unsaturated 6-membered rings, resulting in fluorescence enhancement through the CHEF effect. Sensor **101** showed potential for imaging intracellular Al^{3+} in living cells. The colon cancer SW480 cells stained with sensor **101** exhibited bright blue fluorescence with intracellular Al^{3+}.

Naskar *et al.* developed benzophenone-derived Schiff base sensor **102** for Al^{3+} detection by a fluorometric method (Fig. 39 and Table 2).[159] In ethanol (0.01%)–HEPES buffer (50 mM) solution, sensor **102** (Φ_F = 0.067) exhibited weak fluorescence at 450 nm (λ_{ex} = 321 nm). In the presence of Al^{3+}, sensor **102** underwent fluorescence enhancement (Φ_F = 0.237) at 450 nm. Job's plot showed 1 : 2 (Al^{3+}/**102**) stoichiometry and the binding constant was 10.188 × 10^3 M^{-1}. The limit of detection was 10^{-7} M for Al^{3+}. The complexation of sensor **102** with Al^{3+} resulted in the formation of sensor **102**–Al^{3+} aggregates, which in turn caused inhibition of C=N isomerization and the ESIPT

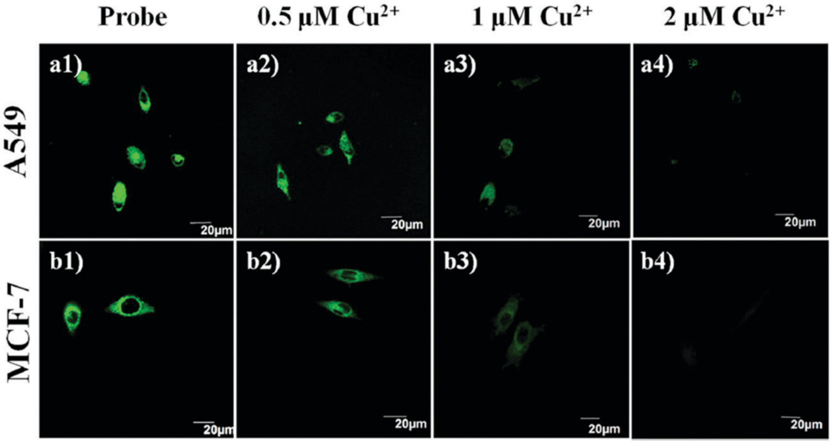

Fig. 41 Confocal fluorescence images of A549 cells incubated with sensor **94** (probe) in the (a1) absence and (a2–a4) presence of Cu^{2+}. Confocal fluorescence images of MCF-7 cells incubated with sensor **94** in the (b1) absence and (b2–b4) presence of Cu^{2+}. Reproduced with permission from ref. 153 Copyright 2019, Elsevier.

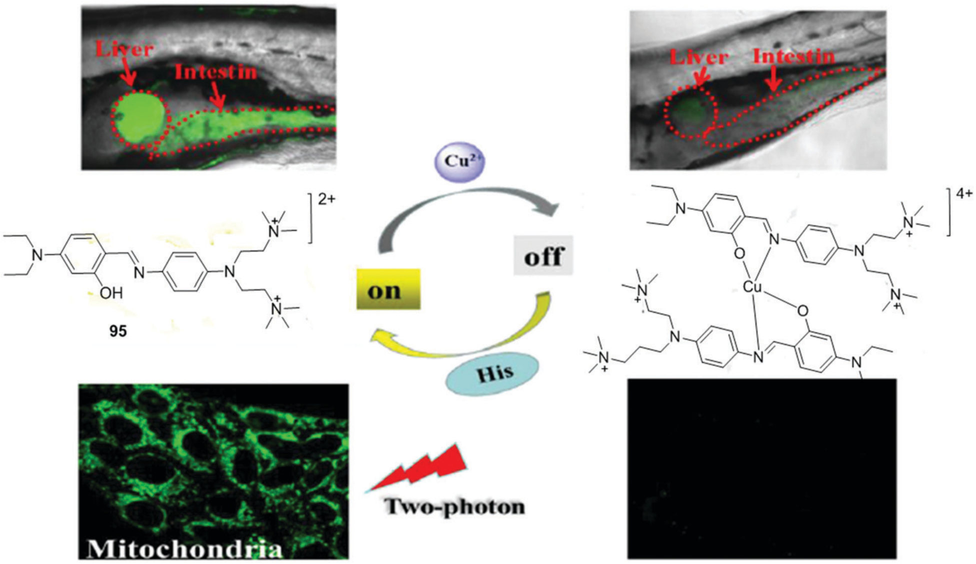

Fig. 42 Practical application of sensor **95** in two-photon fluorescence imaging of Cu^{2+} in cellular mitochondria and in the liver and intestine of larval zebrafish. Reproduced with permission from ref. 154 Copyright 2017, Elsevier.

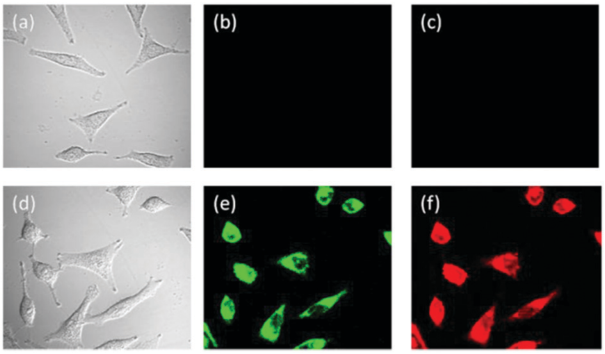

Fig. 43 Confocal microscope images of MCF-cells incubated with sensor **97** (a) under bright field; (b) green channel; (c) red channel; and further incubated with Hg^{2+} (d) under bright field; (e) green channel; (f) red channel. Reproduced with permission from ref. 156 Copyright 2017, Elsevier.

process, leading to the CHEF effect. Sensor **102** displayed no cytotoxicity up to 40 μM as analyzed by MTT assay. The non-fluorescent HepG2 cells stained with sensor **102** exhibited bright blue fluorescence upon binding with intracellular Al^{3+}.

Patra *et al.* reported vanillinyl thioether-based Schiff base **103** as a turn-on sensor for Zn^{2+} detection (Fig. 39 and Table 2).[160] On excitation at 346 nm, sensor **103** (Φ_F = 0.0051) displayed weak emission at 411 nm in DMSO/H_2O (HEPES buffer, v/v = 3/7) solution. In the presence of Zn^{2+}, sensor **103** exhibited new emission at 555 nm and its intensity gradually increased with the increasing concentration of Zn^{2+} from 0 to ~1 mol equiv. (Φ_F = 0.0399). The complexation of sensor **103** with Zn^{2+} caused blockage of the PET process, inhibition of the ESIPT process through deprotonation of the phenolic hydroxyl group and turn-on emission through the CHEF effect. The complexation stoichiometry was 1 : 1 (**103**/Zn^{2+}) and the binding constant was 3.9×10^4 M^{-1}. The detection limit was 60 nM for Zn^{2+}. Vero cells treated with sensor **103** exhibited strong fluorescence when exposed to Zn^{2+}, demonstrating the potential of sensor **103** for imaging intracellular Zn^{2+} in living cells (Fig. 44).

Shellaiah *et al.* synthesized pyrene-based Schiff base **104** and utilized it as a turn-on sensor for Hg^{2+} detection by a fluorometric method (Fig. 39 and Table 2).[161] In DMSO–H_2O (7 : 3, v/v) solution, sensor **104** showed selective turn-on fluorescence response with Hg^{2+} over other metal ions. Fluorescence titration of sensor **104** with Hg^{2+} displayed a 31-fold increase in fluorescence intensity along with a red-shift of the emission maxima from 427 nm to 445 nm (λ_{ex} = 347 nm). The stoichiometry of the complex was 2 : 1 (**104**/Hg^{2+}) and the association constant was 7.36×10^4 M^{-1}. The limit of detection was 2.82 μM for Hg^{2+}. The turn-on sensing mechanism could be attributed to excimer formation (**104**–**104***) and the CHEF effect (Fig. 45A). Sensor **104** displayed potential for imaging Hg^{2+} in living cells using a confocal microscope. The non-fluorescent HeLa cells incubated with sensor **104** exhibited bright blue fluorescence upon treatment with Hg^{2+} (Fig. 45B).

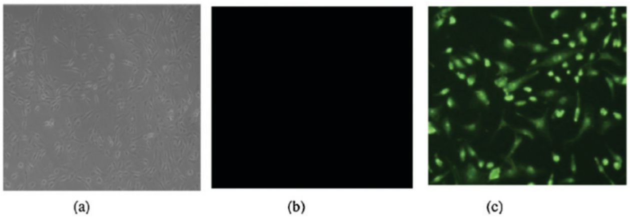

Fig. 44 Confocal microscope images of (a) Vero cells; (b) cells stained with sensor **103**; (c) cells stained with Zn^{2+} and then exposed to sensor **103** for 10 minutes. Reproduced with permission from ref. 160 Copyright 2016, Elsevier.

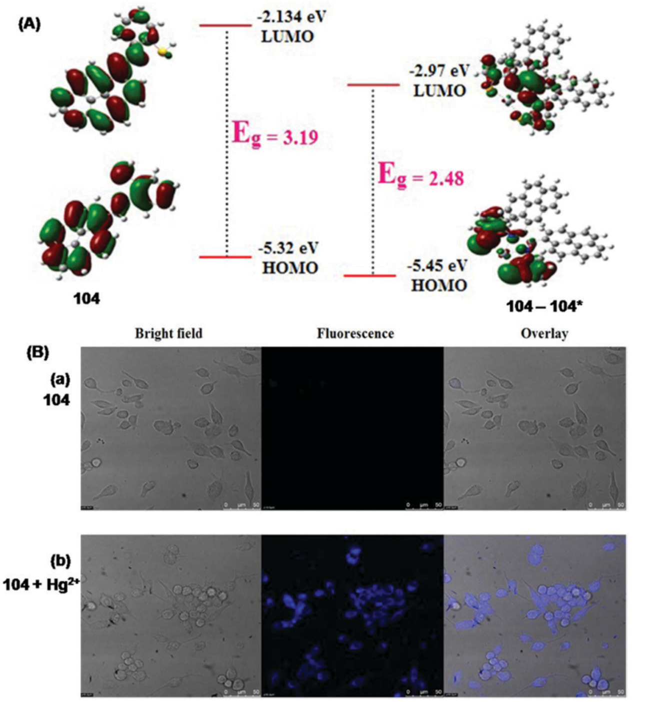

Fig. 45 (A) HOMOs, LUMOs and the energy gap of sensor **104** and **104** + Hg^{2+} (**104**–**104***) complexes. (B) Confocal microscope images of HeLa cells treated with (a) sensor **104** and (b) sensor **104** + Hg^{2+}. Reproduced with permission from ref. 161 Copyright 2015, Royal Society of Chemistry.

Simon *et al.* developed anthracene- and pyridine-derived Schiff base **105** as an off–on sensor for Cu^{2+} detection (Fig. 39 and Table 2).[162] On excitation at 350 nm, sensor **105** displayed 23-fold fluorescence enhancement at 430 nm selectively with Cu^{2+} over other tested metal ions in acetonitrile solution. The stoichiometry of the complex was 1 : 1 (**105**/Cu^{2+}) and the association constant was 2.12×10^6 M^{-2}. The detection limit was 86.3 nM for Cu^{2+}. The sensing mechanism could be ascribed to suppression of the PET process upon Cu^{2+} coordination with sensor **105**, leading to the formation of the 5-membered stable chelate ring and turn-on emission through the CHEF effect. Sensor **105** showed excellent cell permeability, no cytotoxicity up to 40 μM concentration, and potential for fluorescence imaging of sub-cellular Cu^{2+}. The non-fluorescent Raw264.7 cells incubated with sensor **105** exhibited bright blue fluorescence upon treatment with Cu^{2+} under a confocal microscope.

Tian *et al.* synthesized quinoline-based Schiff base sensor **106** and utilized it as a turn-on sensor for Al^{3+} detection (Fig. 39 and Table 2).[163] In methanol solution, the complexation behavior of sensor **106** towards various metal ions revealed selective 38-fold fluorescence enhancement at 517 nm (λ_{ex} = 373 nm) only with Al^{3+}. Job's plot revealed a 1 : 1 (**106**/Al^{3+}) complexation and the association constant as determined using the Benesi–Hildebrand equation was 2.4×10^4 M^{-1}. The detection limit was 0.12 μM for Al^{3+}. The turn-on sensing mechanism could be credited to suppression of the PET process upon Al^{3+} coordination with sensor **106**. HeLa cells incubated with different concentrations of Al^{3+} displayed fluorescence emission when exposed to sensor **106**, demonstrating the potential of sensor **106** for imaging Al^{3+} in living cells.

Tian *et al.* developed 2-hydroxynaphthalene-based Schiff base sensor **107** for Al^{3+} detection (Fig. 39 and Table 2).[164] In methanol medium, free sensor **107** was non-fluorescent. Upon addition of Al^{3+}, sensor **107** underwent a significant increase in fluorescence intensity (150-fold) at 430 nm (λ_{ex} = 307 nm). The binding constant was 3.01×10^4 M^{-1} and the limit of detection was 0.137 μM for Al^{3+}. ^1H NMR and Job's plot analysis indicated inhibition of the ESIPT process upon coordination of Al^{3+} with sensor **107** through the nitrogen atom of imine, secondary amine, and the naphthol hydroxyl group in 1 : 1 stoichiometry. HeLa cells incubated with Al^{3+} showed blue fluorescence when exposed to sensor **107** under a confocal microscope, demonstrating the potential of sensor **107** for fluorescence imaging of Al^{3+} in living cells. Sensor **107** also found application in the *in vivo* bioimaging of Al^{3+} in zebrafish larvae (Fig. 46A and B).

Wang *et al.* developed boron-dipyrromethene-based Schiff base **108** for fluorescence-based detection of Au^{3+} (Fig. 39 and Table 2).[165] In phosphate buffer–ethanol (7 : 3, v/v) solution, sensor **108** was weakly fluorescent. Among various metal ions, significant enhancement in fluorescence intensity was observed only with Au^{3+} (Fig. 47A). Upon gradual addition of Au^{3+} to the solution of sensor **108**, the fluorescence intensity increased linearly with concentration from 0 to 50 μM at 516 nm (λ_{ex} = 480 nm) and reached a plateau after the addition of 6 equvi. of Au^{3+}. The limit of detection was 60 nM for Au^{3+}. The sensing mechanism was a reaction-based process, wherein the reaction of sensor **108** with Au^{3+} resulted in the conversion of the C=N bond into aldehyde and formation of a new boron-dipyrromethene derivative (bright green fluorescent). Sensor **108** found potential application in monitoring Au^{3+} in living cells and in zebrafish. As shown in Fig. 47C, PC12 cells incubated with sensor **108** displayed bright fluorescence when exposed to Au^{3+}. Fig. 47B shows an increase in fluorescence intensity with the increasing concentration of Au^{3+} ions in zebrafish.

Rahman *et al.* developed methionine-based Schiff base **109** as a turn-on sensor for Zn^{2+} detection (Fig. 39 and Table 2).[166] In buffered acetonitrile–water (1 : 1) solution, sensor **109** displayed significant fluorescence enhancement at 450 nm (λ_{ex} = 370 nm) only with Zn^{2+} over other metal ions. The binding constant was 5.3×10^6 M^{-1} and the detection limit was 0.5 μM for Zn^{2+}. The sensing mechanism could be attributed to the complexation of Zn^{2+} with the oxygen, nitrogen, and sulfur atom of sensor **109** in a 1 : 1 ratio as confirmed from ^1H NMR titration. Breast cancer cells incubated with sensor **109** and then with Zn^{2+} displayed strong fluorescence under a confocal microscope, demonstrating the potential of sensor **109** for monitoring intracellular Zn^{2+}.

Yang *et al.* developed biphenyl- and benzohydrazide-based Schiff base **110** for Cu^{2+} detection (Fig. 48 and Table 2).[167] In buffered ethanol–water (1 : 1, v/v) solution, sensor **110** exhibited fluorescence at 566 nm (λ_{ex} = 400 nm). Fluorescence titration of sensor **110** with Cu^{2+} revealed a gradual decrease in

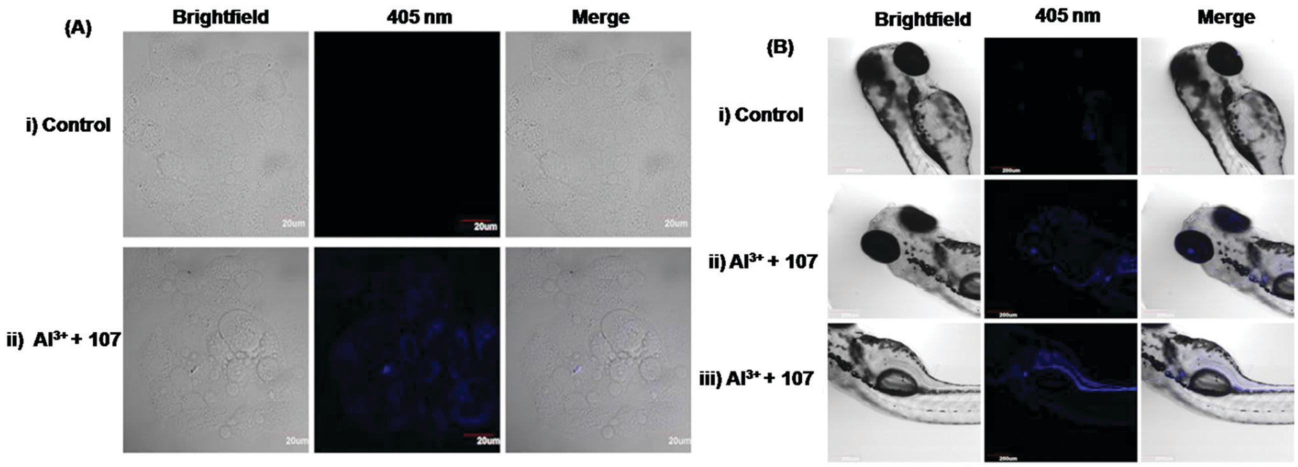

Fig. 46 Confocal microscopic images of HeLa cells incubated with (i) sensor **107** and (ii) sensor **107** and further with Al^{3+}. (b) Confocal microscopic images of zebrafish larvae treated with (i) sensor **107** and (ii, iii) sensor **107** and further with Al^{3+}. Reproduced with permission from ref. 164 Copyright 2019, Elsevier.

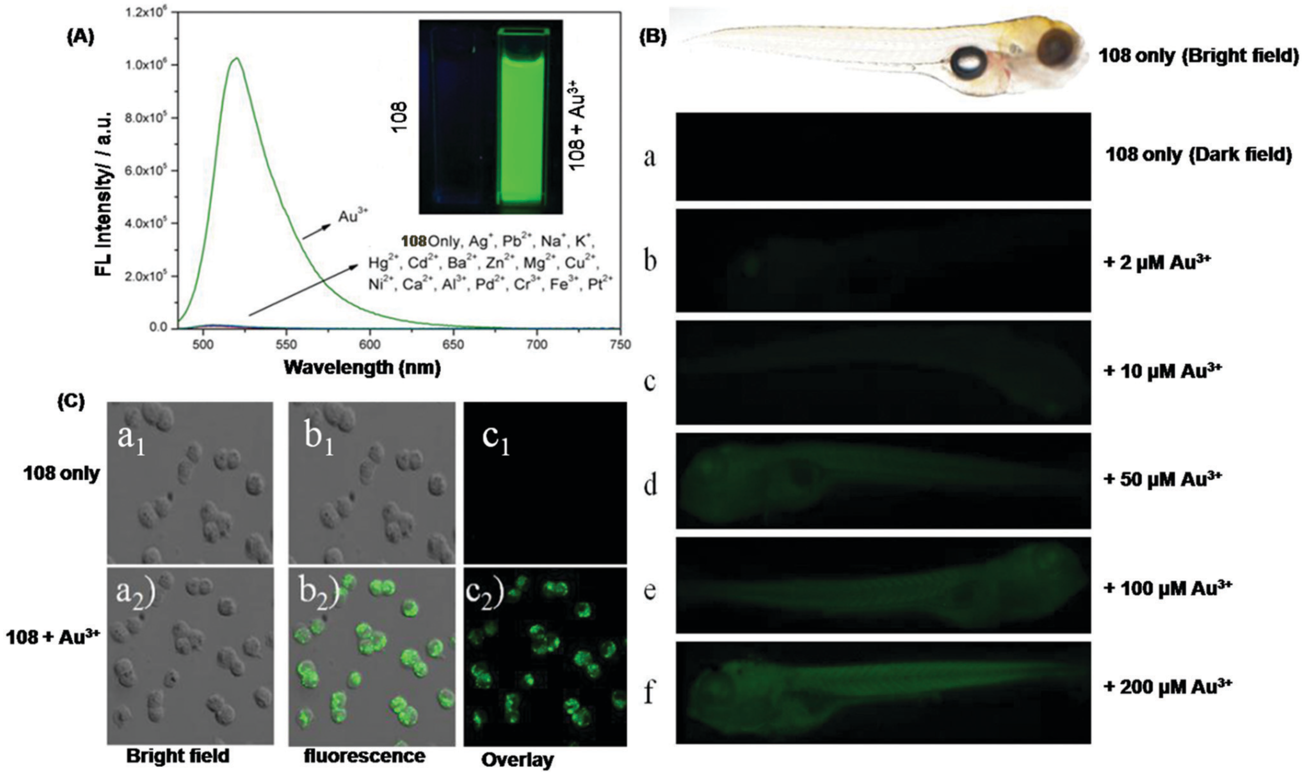

Fig. 47 (A) Fluorescence spectrum of sensor **108** in the presence of different metal ions. (Inset:) Visible color change of sensor **108** in the presence of Au^{3+}. (B) Confocal microscopic images of (a) zebrafish incubated with sensor **108**; (b–f) zebrafish incubated with different concentrations of Au^{3+} followed by the addition of sensor **108**. (C) Confocal microscopic images of PC12 cells (a_1, b_1, c_1) incubated with sensor **108**; (a_2, b_2, c_2) incubated with sensor **108** and further incubated with Au^{3+}. Reproduced with permission from ref. 165 Copyright 2016, Elsevier.

fluorescence intensity, which reached saturation after the addition of 4.0 equivalents of Cu^{2+}. The association constant was $13.87 \times 10^4\ M^{-1}$ and the binding stoichiometry was 1 : 1 (**110**/Cu^{2+}). The limit of detection was 15.4 nM for Cu^{2+}. The coordination of Cu^{2+} with sensor **110** through two oxygen atoms of the hydroxyl group and two nitrogen atoms of the imine group resulted in excited state energy/electron transfer from sensor **110** to Cu^{2+}, causing fluorescence quenching. The bright fluorescence of HeLa cells incubated with sensor **110** diminished after treatment with Cu^{2+}, demonstrating the potential application of sensor **110** in biological systems.

Zhu *et al.* developed Schiff base **111** as an on–off sensor for Al^{3+} detection in DMSO–H_2O (9 : 1, v/v) solution (Fig. 48 and Table 2).[168] On excitation at 377 nm, sensor **111** exhibited a weak emission band at 479 nm. In the presence of Al^{3+}, sensor **111** displayed a more than 700-fold increase in fluorescence intensity at 479 nm. The detection limit was 9.79 nM for Al^{3+}. The complexation stoichiometry was 2 : 1 (**111**/Al^{3+}). The chelation of sensor **111** with Al^{3+} inhibited the PET process and resulted in fluorescence enhancement through the CHEF effect. The Benesi–Hildebrand equation revealed an association constant value of 7.106×10^{10} M^{-2}. HeLa cells incubated with sensor **111** displayed insignificant fluorescence. Upon further incubation with Al^{3+}, remarkable bright blue fluorescence was observed under a confocal microscope, demonstrating the application potential of sensor **111** in biological systems.

3.4.2 Bacterial detection. Pathogenic bacteria cause serious diseases such as typhoid fever, tetanus, tuberculosis, pneumonia, *etc.*, globally. Therefore, for safety purposes, detection of bacteria is important. In the literature, various methods such as PCR-based assays, immunological methods, colony counting and culturing, *etc.* have been used for the detection of bacteria. However, these methods suffer from complicated

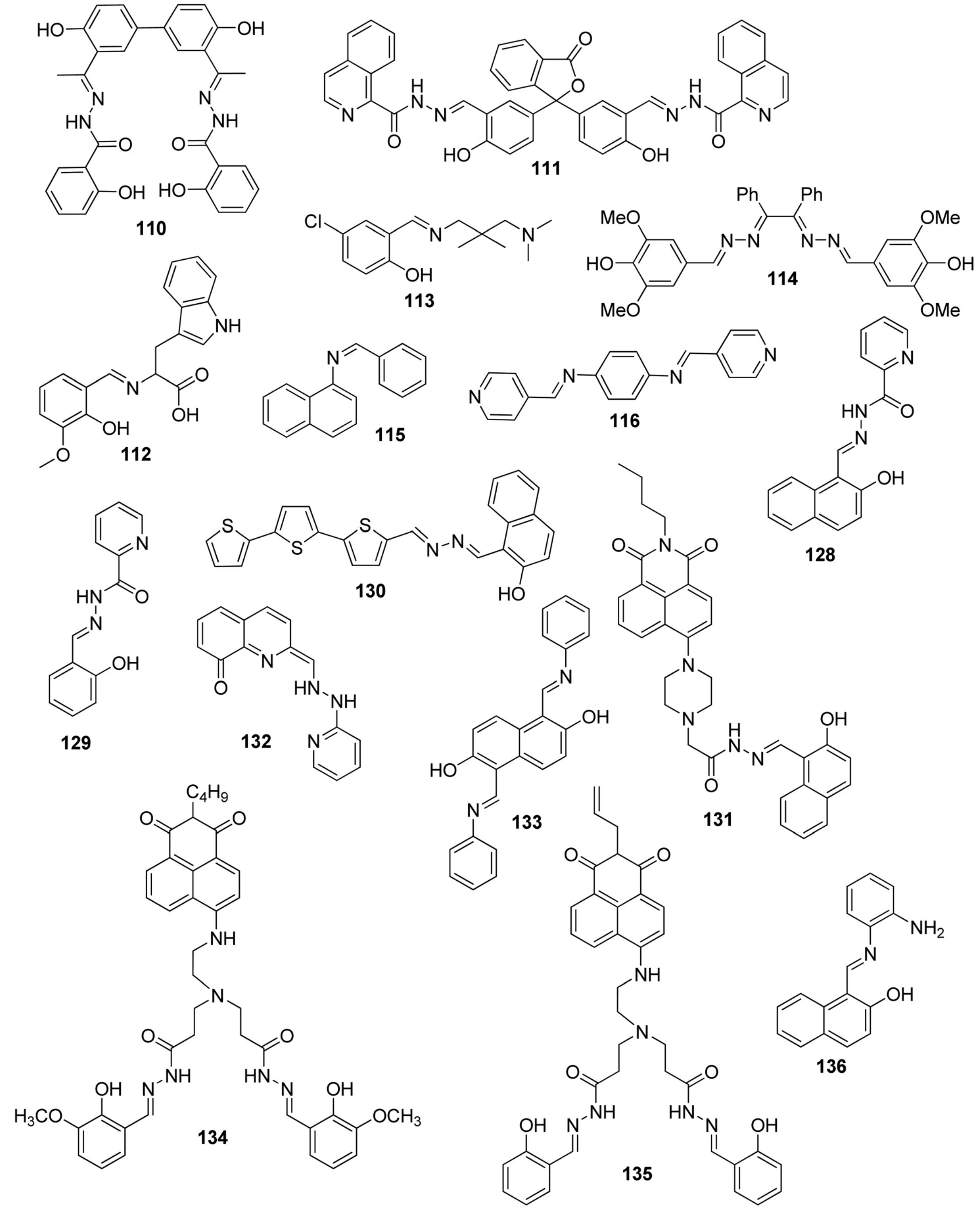

Fig. 48 Chemical structure of sensors **110–136**.

procedures, time-consuming operations, and costly apparatus. Fluorescent biosensors offer the advantages of high selectivity, sensitivity, and fast response time in bacterial detection.

Subha *et al.* developed Schiff base **112** as a turn-on sensor for Zn^{2+} (Fig. 48 and Table 2).[169] In an aqueous medium, sensor **112** exhibited weak emission at 458 nm (λ_{ex} = 350 nm). Sensor **112** showed selective fluorescence enhancement only with Zn^{2+} over other metal ions. Fluorescence titration of sensor **112** with Zn^{2+} revealed ~40-fold fluorescence enhancement at 460 nm along with a slight red-shift, attributed to inhibition of C=N isomerization. The stoichiometry of the complex was 1 : 1 (**112**/Zn^{2+}) and the binding constant was $1.57 \times 10^5\ M^{-1}$. The limit of detection was 10.4 nM for Zn^{2+}. Sensor **112** exhibited potential application in sensing bacterial cells, *viz. Staphylococcus aureus* and *E. coli*. The turn-on fluorescence enhancement with bacterial cells could be credited to the formation of an amide or ester bond with the cell wall of bacteria (Fig. 49).

3.4.3 Drug sample analysis. The improvement in the field of analytical chemistry is supported by the use of fluorescent materials,[170] biomaterials,[271,272] and nanomaterials[273–275] in the analysis of samples. Fluorescent materials offer various advantages such as fast analysis time, high sensitivity and selectivity, low detection limit, and *in vivo* and *in vitro* investigation facility.

Kundu *et al.* reported Schiff base sensor **113** for Al^{3+} and Zn^{2+} detection in methanol–H_2O (1/9, v/v) solution (Fig. 48 and Table 2).[170] On excitation at 254 nm, sensor **113** exhibited weak emission with maxima at 355 nm. In the presence of Al^{3+} or Zn^{2+}, sensor **113** underwent fluorescence enhancement with emission maxima centred at 495 nm (λ_{ex} = 392 nm) for Al^{3+} and with emission maxima at 448 nm (λ_{ex} = 384 nm) for Zn^{2+} (Fig. 50a and b). Job's plot proved a 1 : 1 (**113** : Al^{3+}/Zn^{2+}) complexation. The binding constant value was $1.66 \times 10^4\ M^{-1}$ and $0.6 \times 10^4\ M^{-1}$ for Al^{3+} and Zn^{2+}, respectively. The detection limit was 0.804 μM and 0.795 μM for Al^{3+} and Zn^{2+}, respectively. The complexation of sensor **113** with Al^{3+}/Zn^{2+} provides rigidity to the system by inhibiting the ESIPT process, the PET process, and C=N isomerization, causing fluorescence enhancement through the CHEF effect. Sensor **113** found application in Al^{3+} and Zn^{2+} analysis in drug samples such as Gelucil and Zincovit, as well as in bioimaging of Al^{3+} and Zn^{2+} in HeLa cells.

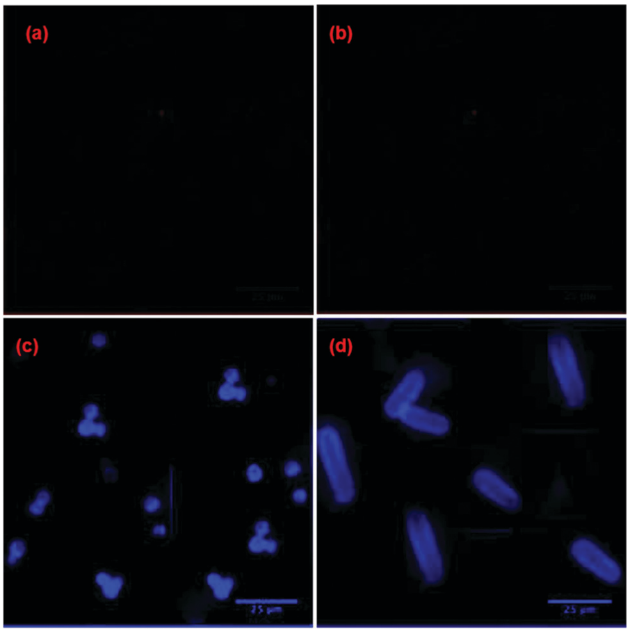

Fig. 49 Fluorescence photographs of (a) *Streptococcus* cells; (b) *E. coli* cells; (c) *Streptococcus* cells incubated with sensor **112**; (d) *E. coli* cells incubated with sensor **112**. Reproduced with permission from ref. 169 Copyright 2016, Elsevier.

3.4.4 Biological sample analysis[276]. Bovine serum albumin is a large globular protein composed of 582 amino acid residues. BSA is most abundant in plasma protein ($0.38\ mL^{-1}$). BSA performs important functions in our circulatory system such as transport of endogenous and exogenous compounds such as drugs, *etc.*[277,278] Thus, quantification of BSA is important. Recently, researchers are developing fluorescent biosensors for metal ion detection using BSA as a medium, since it provides rapid, highly selective, and sensitive detection under physiological conditions.

Ghorai *et al.* developed sensor **114** based on azino bis-Schiff base for fluorescence-based detection of Pb^{2+} (Fig. 48 and Table 2).[171] In methanol–water (2 : 1, v/v) solution, sensor **114** exhibited weak emission at 429 nm (λ_{ex} = 340 nm). Among various metal ions, sensor **114** displayed 34-fold fluorescence enhancement at 442 nm (λ_{ex} = 340 nm) only with Pb^{2+}. The limit of detection was 8 nM for Pb^{2+}. The binding stoichiometry was 2 : 1 (**114** : Pb^{2+}). The coordination of Pb^{2+} with sensor **114** resulted in blockage of the PET process along with the formation of a rigid system, causing fluorescence enhancement through the CHEF effect. Fluorescence titration of sensor **114** with Pb^{2+} in BSA medium displayed a ~32-fold increase in emission intensity, illustrating the potential application of sensor **114** in biological samples. In addition, sensor **114** found application in Pb^{2+} determination in environmental samples such as tap water, river water, and urine samples.

Kumar *et al.* developed Schiff base sensor **115** for fluorescence-based detection of Al^{3+} by turn-on mode (Fig. 48 and Table 2).[172] In CH_3CN–H_2O (1 : 1, v/v) solution, sensor **115** exhibited emission maxima at 430 nm (λ_{ex} = 360 nm). Fluorescence titration of sensor **115** with Al^{3+} revealed a 42-fold increase in fluorescence intensity. The binding constant was $0.4 \times 10^6\ M^{-1}$ and the binding stoichiometry ratio was 3 : 1 (**115** : Al^{3+}). The limit of detection was 50 μM for Al^{3+}. The off–on fluorescence behavior could be attributed to inhibition of the PET process and enhanced electron delocalization upon coordination of Al^{3+} with sensor **115**. The fluorescence titration of sensor **115** with Al^{3+} in BSA aqueous medium showed 30 times fluorescence enhancement in comparison to that of the initial one, demonstrating the application of sensor **115** in biological samples. In addition, sensor **115** found application in Al^{3+} detection in living cells (human embryonic kidney (HEK)).

Ghorai *et al.* developed Schiff base sensor **116** for fluorescence-based detection of Al^{3+} and HSO_3^- in methanol–water (2 : 1, v/v) solution (Fig. 48 and Table 2).[173] Fluorescence

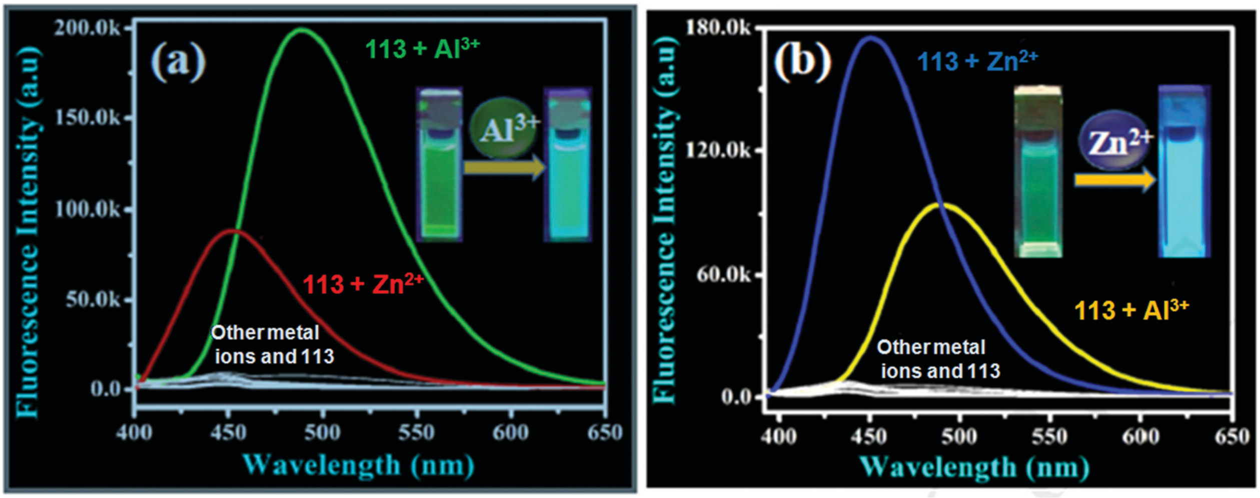

Fig. 50 The emission spectrum of sensor **113** in the absence and presence of different metal ions: (a) fluorescence response on excitation at 392 nm; (b) fluorescence response on excitation at 384 nm. Reproduced with permission from ref. 170 Copyright 2019, Elsevier.

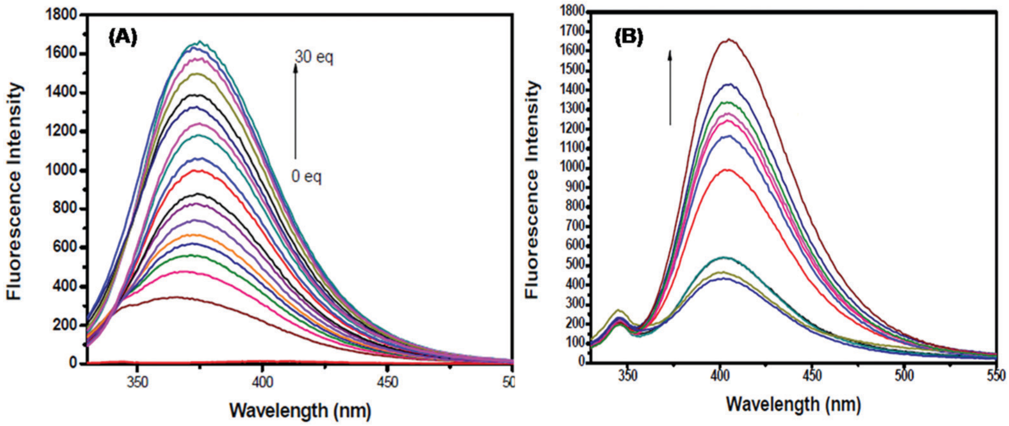

Fig. 51 Fluorescence titration of (A) sensor **116** with Al^{3+} in methanol–water (2 : 1, v/v) solution; (B) sensor **116** with Al^{3+} in bovine serum albumin medium. Reproduced with permission from ref. 173 Copyright 2015, Royal Society of Chemistry.

titration of sensor **116** with Al^{3+} showed a gradual increase in fluorescence intensity at 373 nm (λ_{ex} = 310 nm) upon addition of an increasing concentration of Al^{3+} along with the blue-shift of the emission maxima by 28 nm (Fig. 51A). The interaction of Al^{3+} with sensor **116** resulted in inhibition of the PET process and C=N isomerization, causing fluorescence enhancement through the CHEF effect. The stoichiometry of the complex was 1 : 2 (**116**/Al^{3+}) and the association constant was 1.26×10^5 M^{-1}. The limit of detection was 0.903 μM for Al^{3+}. Sensor **116** showed remarkable detection over a wide pH range of 4–11 and found application in Al^{3+} detection in the aqueous solution of bovine serum albumin protein (Fig. 51B).

3.4.5 Anticancer activity[174–176,279].

Nowadays cancer is a very serious disease, and looking into the present situation of drugs for cancer treatment, WHO predicted that more than 13.1 million people may die by 2030 due to cancer. Currently, platinum-based complexes are used as antitumor drugs in the clinic worldwide. However, these drugs have shown multiple side effects such as drug resistance, tissue damage, *etc.* This necessitates the development of an efficient drug for cancer treatment.

Liu *et al.* synthesized Schiff base complexes **117** and **118** for fluorescence-based detection of Cu^{2+} and Fe^{3+} in an aqueous medium (Fig. 52 and Table 2).[174] Among various metal ions, sensor **117** underwent fluorescence quenching selectively with

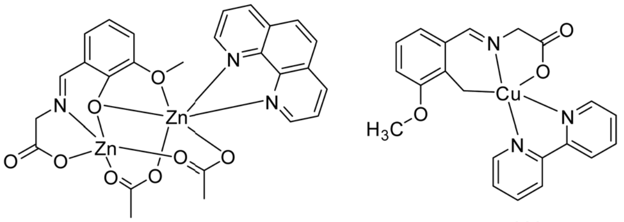

117

118

Fig. 52 Chemical structure of complexes **117** and **118**.

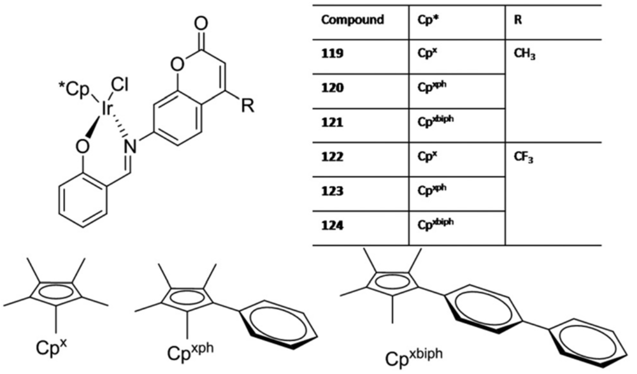

Compound	Cp*	R
119	Cpx	CH3
120	Cpxph	
121	Cpxbiph	
122	Cpx	CF3
123	Cpxph	
124	Cpxbiph	

Fig. 53 Chemical structure of complexes **119–124**.

Cu^{2+} and Fe^{3+} only. The sensing mechanism could be attributed to host–guest interaction, metal-ion exchange, or competition between the metal ions and complexes for absorption and excitation energy. Furthermore, complex **118** demonstrated excellent anticancer activity against four human tumor cell lines, namely, MDA-MB-231 (human breast cancer), HT29 (human colon cancer), HeLa (human cervical cancer), and PC-3 (human prostate cancer).

Considering the important applications of coumarin derivatives such as antifungal, anticoagulant, and anticancer, Liu *et al.* synthesized Schiff base-Ir(III) complexes (**119–124**) as an antitumor agent (Fig. 53 and Table 2).[175] All the six complexes exhibited excellent biological stability, and their anticancer activity can be tuned by slight adjustment in the number of phenyl groups and electron donor ability of the Schiff base. In DMSO–H_2O (2 : 8, v/v), the fluorescence spectrum of complexes **119–121** showed maxima at 422 nm and this was red-shifted to 474 nm in complexes **122–124**. Further, these complexes successfully targeted lysosomes and mitochondria, could induce apoptosis, and displayed potential application as antitumor agents.

Kim *et al.* provided a naphthalene-based donor–acceptor type platform for fluorescence-based detection of Fe^{3+} (Fig. 54 and Table 2).[176] The fluorescence spectrum of sensor **125** showed enhancement in emission intensity at 550 nm upon the addition of Fe^{3+}, credited to inhibition of the ESIPT based quenching effect. Further, the sensor displayed application in the fluorescence imaging of Fe^{3+} in HeLa cells and cancer cell lines. The yellow emission of HeLa cells following incubation with exogenous Fe^{3+} was more intense than that of the control group incubated with sensor **125**.

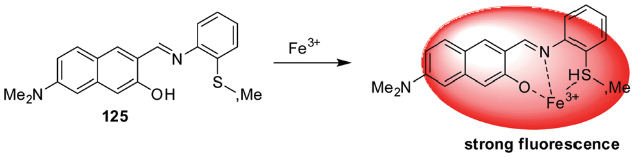

Fig. 54 Sensing mechanism of Fe^{3+} with sensor **125**.

3.5 Environmental monitoring

3.5.1 Catalytic applications. Over the years, numerous Schiff base–metal complexes have been developed and efficiently used as catalysts in organic transformation reactions.[280,281] Thus, discussion of the catalytic applications of fluorescent Schiff base–metal complexes constitutes an interesting topic of research.

Salih *et al.* prepared fluorescent Schiff base ligand **126** using 2-(1-piperazinyl)ethylamine and 2-hydroxy-5-nitrobenzaldehyde, and the corresponding Cu(II)-complexes (Fig. 55 and Table 2).[177] In DMSO solution, the emission spectrum of the Schiff base ligand **126** revealed turn-off response upon complexation with Cu(II) (λ_{ex} = 360 nm, λ_{em} = 475 nm), could be attributed to the PET process and the CHEF effect or to structural change in the ligand upon complexation. Further under mild catalytic conditions for oxidation and in the presence of H_2O_2 (green oxidant), the Schiff base–Cu(II) complex successfully catalyzed the benzyl alcohol to benzaldehyde oxidation reaction.

3.5.2 Adsorption. Fluorescent Schiff base doped polymeric materials have emerged as new candidates for metal ion detection, owing to several advantages offered by fluorescent polymeric materials such as amplified optical properties, high detection limit, *etc.*

Xue *et al.* developed sulfonylhydrazone type Schiff base sensor **127** (AIE-active) for fluorescence-based detection of Hg(II) (Fig. 56 and Table 2).[178] The emission spectrum of sensor **127** showed turn-off response (λ_{ex} = 414 nm, λ_{em} = 549 nm) with the addition of an increasing concentration of Hg^{2+}, and a good linear range between 0.1 and 0.6 μM concentration of Hg^{2+}. The limit of detection was 0.284 nM, and the response time was 15 seconds for Hg^{2+}. Interestingly, polyacrylamide (PAM) doped Schiff base **127** (**127**–PAM polymer) demonstrated high efficiency of Hg^{2+} adsorption, with a 99.9% removal rate.

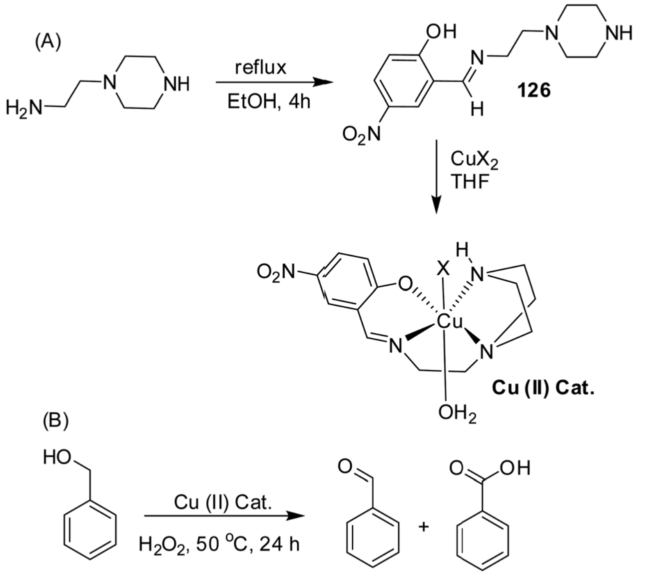

Fig. 55 (A) Chemical structure of Schiff base ligand **126** and the **126**–Cu^{2+} complex. (B) Benzyl alcohol oxidation reaction catalysed by **126**–Cu^{2+} complex.

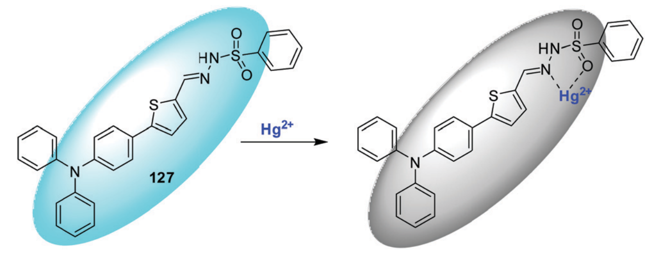

Fig. 56 Sensing mechanism of Hg^{2+} with sensor **127**.

Additionally, sensor **127** displayed potential for Hg^{2+} detection in real water samples and for logic gate construction.

3.5.3 Real sample analysis[185,280,282–285]. Although the fluorescent sensors for metal ion detection have shown advantages such as simplicity, selectivity, sensitivity, and rapid response time over other analytical methods, working with some toxic metal ions has always been problematic due to strong hydration, poor coordination, and lack of spectroscopic characteristics. Therefore, researchers are working on the development of fluorescent materials for direct detection of metal ions in real samples such as water, food, *etc.*

Peng *et al.* synthesized pyridine-based Schiff base sensors **128** and **129** for Al^{3+} detection (Fig. 48 and Table 2).[179] In DMF–H_2O (v : v = 1 : 9) solution, both sensors **128** and **129** exhibited weak emission centered at 483 nm (λ_{ex} = 360 nm) and 467 nm (λ_{ex} = 300 nm), respectively. However, upon the addition of Al^{3+}, sensors **128** and **129** displayed an increase in fluorescence intensity at 483 nm and 467 nm, respectively. The turn-on fluorescence was associated with colorless to aquamarine color change of the solution. The limit of detection for Al^{3+} was 3.2 nM and 0.29 nM with sensors **128** and **129**, respectively. Job's plot and HRMS revealed 1 : 1 (**128**/**129** : Al^{3+}) stoichiometry of the complex. The mechanism of interaction could be ascribed to the blockage of the PET and ESIPT processes upon addition of Al^{3+} as confirmed from the ^1H NMR titration experiment. Sensors **128** and **129** found potential application in the detection of Al^{3+} in lake water and tap water.

Guo *et al.* synthesized oligothiophene-based Schiff base **130** as a fluorometric probe for Cu^{2+} detection (Fig. 48 and Table 2).[180] In DMF/H_2O (2/3, v/v) solution, free sensor **130** exhibited strong fluorescence with emission maxima at 580 nm (λ_{ex} = 450 nm). In the presence of Cu^{2+}, sensor **130** underwent fluorescence quenching along with the hypsochromic shift of the emission maxima from 580 nm to 560 nm. The binding constant was 2.52×10^4 M^{-1} for the 1 : 1 (**130**/Cu^{2+}) complex. The limit of detection was 28.1 nM for Cu^{2+}. The decrease in the fluorescence intensity of sensor **130** upon complexation with Cu^{2+} could be ascribed to the paramagnetic nature of Cu^{2+} and the CHEQ mechanism. Furthermore, sensor **130** found application in Cu^{2+} detection in real samples such as water and food with excellent accuracy and precision.

Kang *et al.* synthesized naphthalimide functionalized Schiff base **131** as a fluorescent turn-on sensor for Al^{3+} detection (Fig. 48 and Table 2).[181] In methanol solution, sensor **131** exhibited weak emission maxima at 524 nm (λ_{ex} = 401 nm). Among various tested metal ions, sensor **131** showed significant fluorescence enhancement with Al^{3+} (39-fold), and fluorescence quenching to some extent with Ni^{2+}, Fe^{2+}, Co^{2+}, and Cu^{2+}, whereas other metal ions had an insignificant effect. Fluorescence titration of sensor **131** with Al^{3+} revealed linear enhancement in emission intensity along with the blue shift of the emission maxima from 524 nm to 508 nm, attributed to the combined effect of inhibition of the ICT process and the CHEF effect (Fig. 57A and B). The detection limit was 7.4 nM for Al^{3+}. The association constant was 1.62×10^4 M^{-1} for the 1 : 1 (**131**/Al^{3+}) complex. In addition, the sensor displayed potential application in measuring Al^{3+} concentration in real water samples.

Kao *et al.* synthesized quinoline-derived Schiff base **132** as a fluorescence turn-on sensor for Mg^{2+} detection (Fig. 48 and Table 2).[182] On excitation at 353 nm, free sensor **132** displayed no significant emission in acetonitrile solution. However, in the presence of Mg^{2+}, sensor **132** underwent a significant increase in emission intensity at 487 nm and 532 nm. The association constant was 1.91×10^7 M^{-1} for the 1 : 1 (**132**/Mg^{2+}) complex. The detection limit was 19.1 ppb for Mg^{2+}. The coordination of sensor **132** with Mg^{2+} resulted in the formation of a rigid system by inhibiting C=N isomerization, leading to fluorescence enhancement through the CHEF effect. In addition, sensor **132** found practical application in the determination of Mg^{2+} in real water samples such as tap, ground, and lake water (Fig. 58).

Zhang *et al.* developed Schiff base **133** with AIEE (Aggregation induced emission enhancement) characteristics as a turn-off fluorescent sensor for Cu^{2+} (Fig. 48 and Table 2).[183] In THF-H_2O (4/1, v/v) solution, sensor **133** exhibited emission maxima at 565 nm (λ_{ex} = 428 nm). Both UV-Vis and fluorescence spectra of sensor **133** displayed good selectivity only for Cu^{2+} over other tested metal ions. Fluorescence titration of sensor **133** with Cu^{2+} showed a gradual decrease in fluorescence intensity at 565 nm with the addition of an increasing concentration of Cu^{2+}. The limit of detection was 16.4 nM for Cu^{2+}. The binding

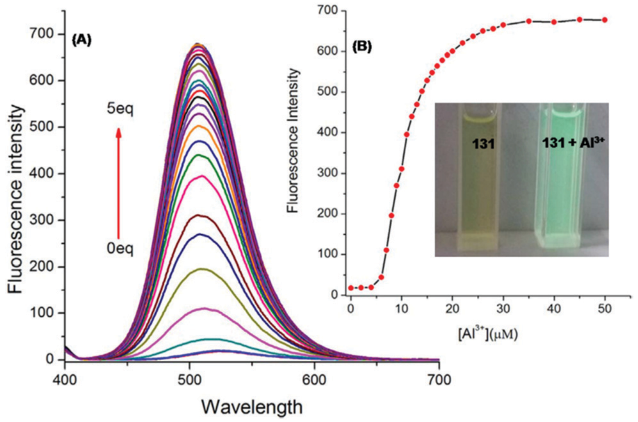

Fig. 57 (A) Fluorescence titration of sensor **131** with Al^{3+}. (B) Plot of fluorescence intensity *vs.* Al^{3+} concentration. Inset: naked eye detectable color change of sensor **131** in the absence (left) and presence of Al^{3+} (right) under 365 nm UV light illumination. Reproduced with permission from ref. 181 Copyright 2017, Elsevier.

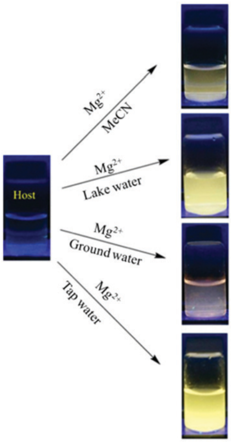

Fig. 58 Photographs of Mg^{2+}-induced light-up emission of sensor **132** in different media such as CH_3CN, lake water, groundwater, and tap water. Reproduced with permission from ref. 182 Copyright 2016, Elsevier.

stoichiometry was 1 : 2 (**133**/Cu^{2+}) and the binding constant was 1.22×10^3 M^{-1}. The transfer of lone pairs of electrons from the nitrogen and oxygen atoms to the empty orbitals of Cu^{2+} blocked the initial ESIPT process and resulted in fluorescence quenching (Fig. 59). Furthermore, sensor **133** found application in monitoring Cu^{2+} concentration in environmental water samples. The percentage recovery of sensor **133** was 98.49–102.37% in tap water and 99.10–102.90% in lake water.

Peng *et al.* developed naphthalimide-based Schiff base **134** as a fluorescent turn-on probe for Al^{3+} (Fig. 48 and Table 2).[184] In DMF-HEPES (1 : 1, v/v) solution, free sensor **134** was weakly fluorescent with emission maxima at 531 nm (λ_{ex} = 350 nm). Upon addition of Al^{3+} into the solution of sensor **134**, a significant increase in fluorescence intensity was observed at 524 nm, attributed to inhibition of the PET process and the CHEF effect. The binding constant value was 4.95×10^4 M^{-1} for the 1 : 1 (**134**/Al^{3+}) complex. The lowest limit of detection was 86.5 nM for Al^{3+}. Furthermore, sensor **134** was found to be useful for Al^{3+} determination in real water samples such as yellow river and tap water.

Further, the same group reported another naphthalimide-based Schiff base **135** for fluorescence-based detection of Al^{3+} (Fig. 48 and Table 2).[185] In Tris–HCl buffer (1 : 1, v/v) solution, free sensor **135** exhibited weak emission at 526 nm (λ_{ex} = 350 nm). Upon addition of various metal ions to the solution of sensor **135**, no significant change in emission intensity was observed except with Al^{3+}. In the presence of Al^{3+}, sensor **135** showed fluorescence enhancement with emission maxima at 526 nm, attributed to strong coordination between sensor **135** and Al^{3+} resulting in inhibition of the PET process and the CHEF effect. The limit of detection was 0.34 μM for Al^{3+}. The binding constant was 2.6×10^4 M^{-1} for the 1 : 1 (**135**/Al^{3+}) complex. Moreover, sensor **135** demonstrated potential application in monitoring Al^{3+} concentration in real water samples such as yellow river and tap water.

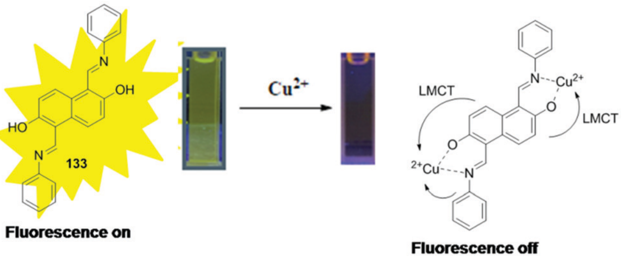

Fig. 59 Sensing mechanism of sensor **133** for Cu^{2+} detection. Reproduced with permission from ref.183 Copyright 2021, MDPI, Basel, Switzerland.

Zhu *et al.* developed Schiff base **136** as a turn-on fluorescent sensor for Al^{3+} detection (Fig. 48 and Table 2).[186] In ethanol-HEPES buffer (95 : 5, v/v) solution, sensor **136** showed high selectivity for Al^{3+} over other tested metal ions. On excitation at 273 nm, sensor **136** displayed weak emission at 473 nm and 499 nm. However, upon the addition of Al^{3+}, a significant enhancement in emission intensity (63-fold) was observed at 473 nm and 499 nm along with the color change of the solution from green to bright blue under 273 nm UV light illumination. The complexation stoichiometry was 1 : 1 (**136**/Al^{3+}). The binding constant of the complex was 6.53×10^3 M^{-1} and the detection limit was 0.108 μM for Al^{3+}. The sensing mechanism could be attributed to blockage of the PET process upon complexation of sensor **136** with Al^{3+}. Furthermore, sensor **136** displayed potential application in detecting Al^{3+} in living cells and environmental samples.

3.5.4 Rewritable paper.

Paper is a versatile material with various uses such as writing, reading, printing, cleaning, *etc.* Although paper is recyclable, huge energy consumption and chemical discharge during the recycling process are unavoidable. In the present world, the massive use of paper is being continuously alleviated by digital storage devices such as computers, mobile, *etc.* Nowadays, researchers are focusing on the development of organic photochromic materials due to their potential application as rewritable paper, sensors, data storage systems, molecular switches, *etc.*[286–291]

Sun *et al.* designed tetraphenylethene-based Schiff base **137** as a colorimetric/fluorescent sensor for Zn^{2+} and for inkless rewritable paper (Fig. 60 and Table 2).[187] In the THF–H_2O (1 : 1, v/v) mixture, sensor **137** showed weak emission maxima at 600 nm, which upon addition of Zn^{2+} resulted in significant fluorescence enhancement along with the blue shift of the emission maxima from 600 nm to 550 nm. Moreover, the emission color of the solution changed from weak red to strong yellow (Fig. 61A). The limit of detection was 38.9 nM for Zn^{2+}. The sensing mechanism could be attributed to the CHEF effect which inhibits the ESIPT, PET, and non-radiative processes, thus resulting in fluorescence enhancement. Further, an inkless rewritable, self-erasing paper was fabricated by utilizing sensor **137** as the imaging layer and H_2O as ink, which showed potential application in data storage, information security, and anti-counterfeiting (Fig. 61B and C). Additionally, sensor **137** found application in monitoring Zn^{2+} in SiHa cells.

Sun *et al.* designed tetraphenylethene-based Schiff base sensor **138** with photochromic properties and employed it as rewritable paper and a UV sensor (Fig. 60 and Table 2).[188] Sensor **138** exhibited weak fluorescence in solid-state, which

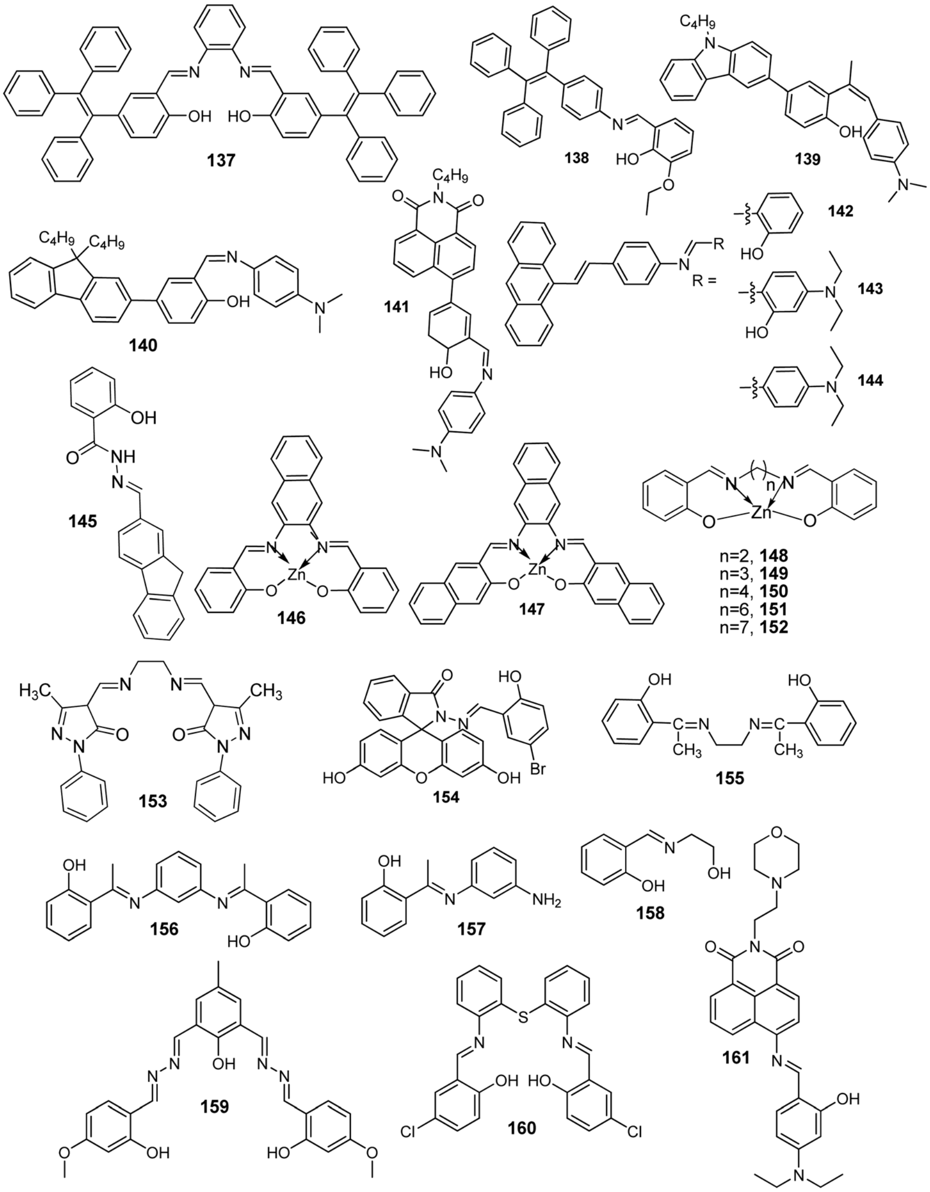

Fig. 60 Chemical structure of chemosensors **137–161**.

after grinding with a pestle resulted in the appearance of a strong emission band between 550 nm and 700 nm, longer response time and reduced photochromic efficiency. The photochromic mechanism of sensor **138** resulted from enol to keto form photoisomerization. Further sensor **138** found application as rewritable paper. With violet light at 410 nm, sensor **138** served as a pen, while with white light and 420 nm–590 nm visible light, sensor **138** was used as an eraser. Moreover, sensor **138** also served as a UV sensor for the detection of UV radiation pollution by the naked eye (Fig. 62A–D).

3.6 Optoelectronic applications

3.6.1 Mechanoluminescence[191,193,194]**.** The tunable emission properties of mechanochromic materials have grabbed significant attention because of their potential application in devices, optical recordings, security inks, and sensors.

Yang *et al.* synthesized Schiff base derivatives **139**, **140**, and **141** for fluorescence-based detection of Cu^{2+} (Fig. 60 and Table 2).[189] All the three sensors (**139**, **140**, and **141**) displayed AIE characteristics in the $CH_3CN–H_2O$ mixture with different water fractions. From the fluorescence experiment, sensor **141** was found to be a specific sensor for Cu^{2+}, whereas sensors **139** and **140** lacked selectivity and displayed fluorescence enhancement with various metal ions (Fig. 63A and C). The fluorescence titration of sensor **141** with Cu^{2+} in $CH_3CN–H_2O$ (4 : 1, v/v) solution revealed a linear increase in fluorescence intensity at 463 nm (λ_{ex} = 350 nm) with the addition of an increasing concentration of Cu^{2+} (0–20 μM). The limit of detection was 2.3×10^{-7} M for Cu^{2+} and the stoichiometry of the complex was

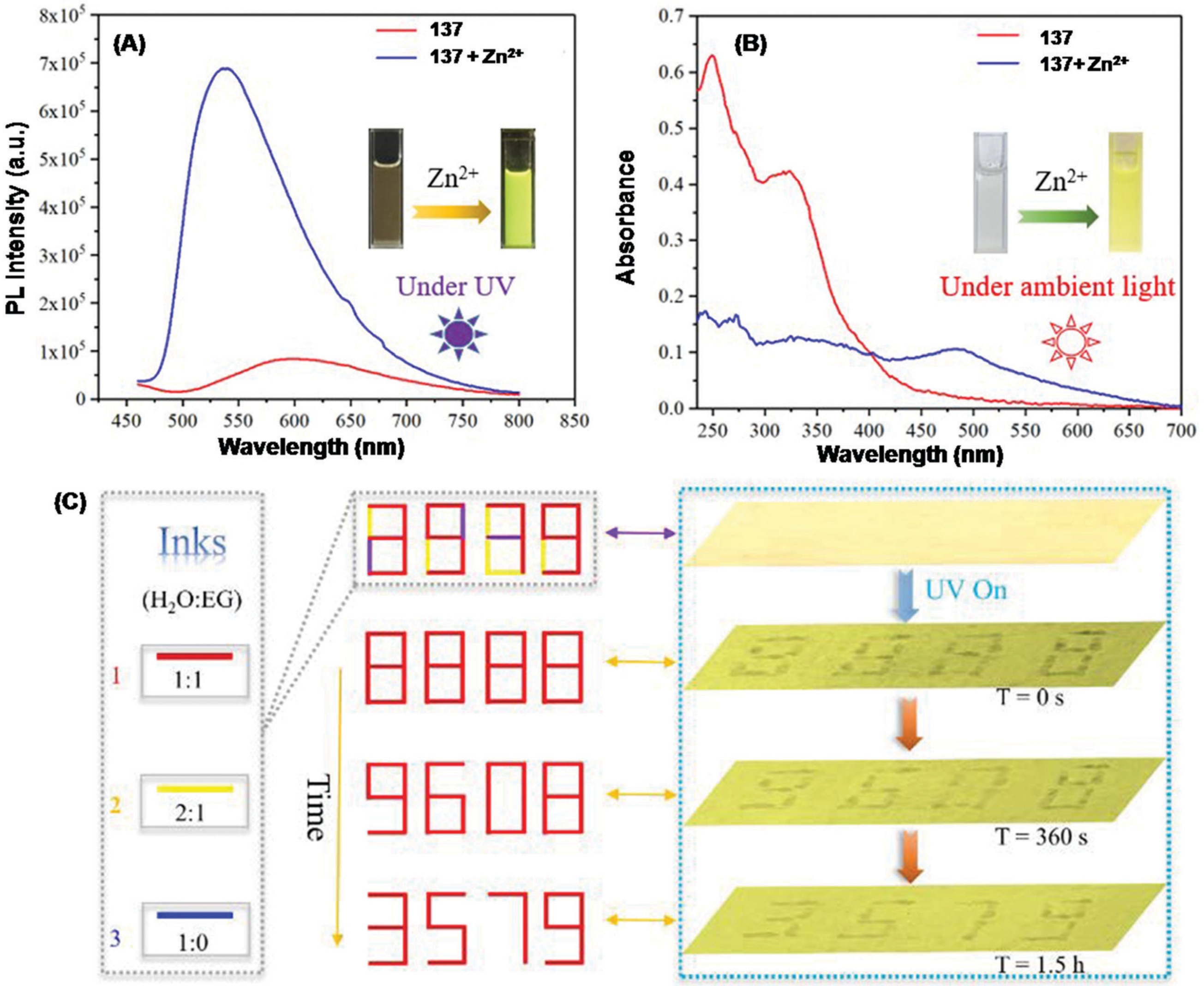

Fig. 61 (A) Fluorescence spectrum; (B) absorbance spectrum of sensor **137** in the absence and presence of Zn^{2+}. Inset: Naked eye detectable color change of sensor **137** solution in the absence and presence of Zn^{2+} under (A) 365 nm UV light and (B) ambient light. (C) Sensor **137** application as inkless rewritable paper in information safety. Reproduced with permission from ref. 187 Copyright 2021, Royal Society of Chemistry.

2 : 1 (**141** : Cu^{2+}). The turn-on fluorescence response of sensor **141** with Cu^{2+} could be attributed to the CHEF effect. Sensor **141** showed reversible mechanochromic fluorescence behavior with the mechanical stress-induced shift of fluorescence spectra by 21 nm, attributed to transformation between crystalline and amorphous states (Fig. 63B and D).

Yang *et al.* developed anthryl-based Schiff bases **142**, **143**, and **144** for Cu^{2+} and Zn^{2+} detection (Fig. 60 and Table 2).[190] Among various tested metal ions, only sensor **143** (λ_{ex} = 432 nm) showed on–off type fluorescence response (λ_{em} = 508 nm) with Cu^{2+} in HEPES buffered methanol-H_2O (4/1, v/v) solution, and off–on type fluorescence response (λ_{em} = 510 nm) with Zn^{2+} in pure methanol solution. The binding stoichiometry was 2 : 1 (**143** : Cu^{2+}/Zn^{2+}), and the binding constant was 1.28×10^8 M^{-1} and 1.05×10^6 M^{-1} for Cu^{2+} and Zn^{2+}, respectively. The limit of detection was 0.212 μM and 71.9 nM for Cu^{2+} and Zn^{2+}, respectively. The different fluorescence responses of sensor **143** with Cu^{2+} and Zn^{2+} could be due to the different electronic configurations of metal ions. For Cu^{2+}, the PET process could be responsible for fluorescence quenching. And for Zn^{2+}, the filled d-orbital and no possibility of d-d transition could be responsible for fluorescence enhancement.

Muthamma *et al.* used fluorene-based Schiff base **145** (AIE-active) for developing environmentally friendly flexographic ink for printed electronics and for security printing applications (Fig. 60 and Table 2).[191] The Schiff base **145** writing and fingerprints on UV dull security paper using flexo ink were invisible under daylight but showed bluish green fluorescence under UV light. Further, the emission of Schiff base **145** writing and fingerprints was sensitive to pH, demonstrating the potential application of the Schiff base in anti-counterfeiting. Further, the mechanical and electrical measurements of flexo-ink printing on UV dull security paper substrates exhibited p-type semiconductivity, thus signifying the potential

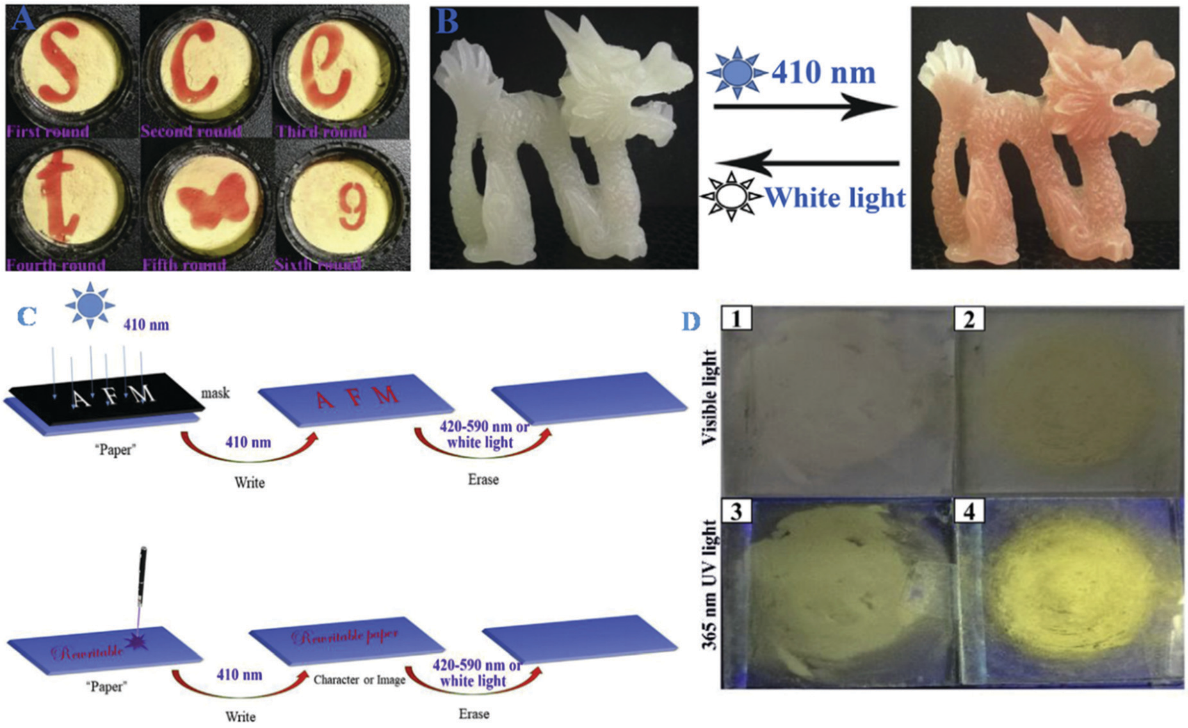

Fig. 62 Application of sensor **138** as rewritable paper: (A) different letter, pattern, and number on rewritable paper; (B) proposed system-based reversible photochromic dragon. (C) Writing and erasing process on rewritable paper. (D) Photographs of sensor **138** under 365 nm UV light and visible light: (1 and 3) pristine sample; (2 and 4) ground sample. Reproduced with permission from ref. 188 Copyright 2019, Elsevier.

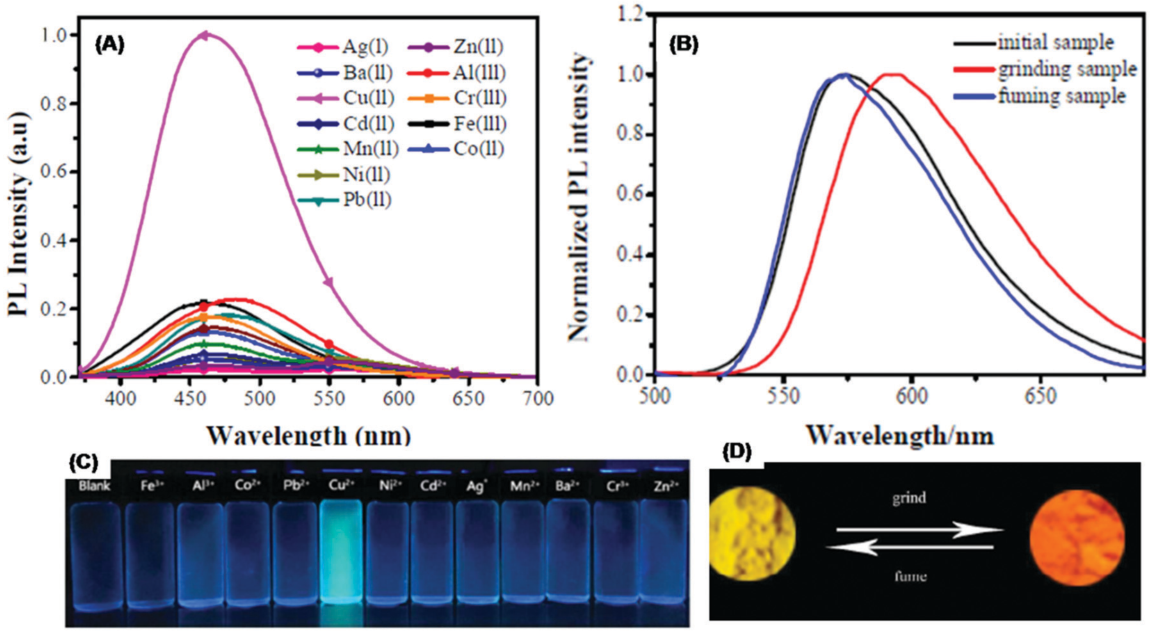

Fig. 63 (A) Fluorescence response of sensor **141** in the presence of different metal ions. (B) Normalized fluorescence spectrum of sensor **141** in different solid-states, *viz.* initial sample, ground sample, and fumed sample. (C) Photographs of sensor **141** solutions in the presence of different metal ions under 365 nm UV light. (D) Color change of sensor **141** after grinding and fuming under 365 nm UV light illumination. Reproduced with permission from ref. 189 Copyright 2017, Royal Society of Chemistry.

for application of Schiff base **145** in organic printed transistor devices.

3.6.2 Color tunable. Currently, various fluorescent materials have been fabricated into devices because of their potential application as light-emitting components in display devices. The optical properties of fluorescent materials can be tuned by chemical modification, functional group addition or substitution, or by complexation with ions.[60,292] The diverse application of these fluorescent materials encouraged the researchers to develop materials with improved fluorescence properties.

Gondia and Sharma *et al.* studied comparative optical properties of sensor **146**–Zn^{2+} and sensor **147**–Zn^{2+} complexes (Fig. 60 and Table 2).[192] Both sensors **146** and **147** are similar in structure except for the presence of additional phenyl groups in sensor **147**. The fluorescence spectrum of sensor **146**–Zn^{2+} and sensor **147**–Zn^{2+} complexes revealed significant emission intensity peaks at 504 nm and 444 nm (λ_{ex} = 372 nm), respectively. Further, the sensor **146**–Zn^{2+} complex showed nearly two times increased fluorescence as well as blue shift as compared to the emission spectrum of the sensor **147**–Zn^{2+} complex, attributed to the presence of an additional phenyl group. The change in emission of sensors **146** and **147** upon complexation with Zn^{2+} through *N*-azomethine and the oxygen atom of the –OH group could be due to the highest to lowest energy state intraligand transition. The CIE (Commission Internationale de L'Eclairage) chromaticity diagram for **146**–Zn^{2+} and **147**–Zn^{2+} complexes revealed a bluish-green region for the **146**–Zn^{2+} complex and a blue region for the **147**–Zn^{2+} complex, suggesting potential application of these complexes in electroluminescent devices (Fig. 64 and Table 3).

Nishal *et al.* presented a series of zinc-Schiff base complexes **148–152** for organic light-emitting device (OLED) application (Fig. 60 and Table 2).[193] On excitation at 365 nm, Schiff base complexes **148**, **149**, **150**, **151**, and **152** emitted blue with the emission maxima centered at 447, 440, 436, 433, and 430 nm, respectively. The blue luminescence of the Schiff-base complexes was assigned to relaxation from higher to lower energy levels because of intra-ligand transition. Notably, as the number of alkyl groups in bridging diamines increased, the emission maxima were more shifted toward the blue region. The CIE chromaticity diagram and color coordinate calculation showed the potential application of Schiff base-zinc complexes in organic light-emitting devices (OLEDs).

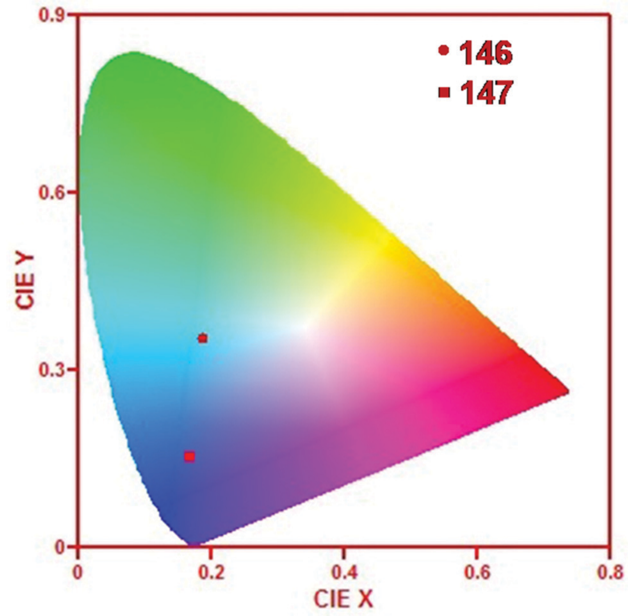

Fig. 64 CIE diagram of **146**–Zn^{2+} and **147**–Zn^{2+} complexes. Reproduced with permission from ref. 192 Copyright 2019, Elsevier.

Table 3 CIE parameter of the complexes and quantum yield. Reproduced with permission from ref. 192 Copyright 2019, Elsevier

Compound	Slope	Quantum yield	Color coordinates	
			x	*y*
146	6.37	0.46	0.187	0.355
147	16.59	1.21	0.168	0.152
Standard	777.95	0.54	—	—

Gusev *et al.* presented an ethylenediamine Schiff base-Zn^{2+} complex (**153**) as a promising emissive material for blue fluorescent OLED applications (Fig. 60 and Table 2).[194] The complex **153** emitted strongly both in solution and solid state with maximum emission in the blue region (430–460 nm), assigned to combination of monomer (419 nm)–excimer (433 and 468 nm). Interestingly, complex **153** was fabricated into an organic-light emitting device and demonstrated promising blue fluorescent OLED applications (maximum external quantum efficiency, EQE_{max} = 5%, and maximum brightness 17 000 cd m^{-2}).

3.6.3 Logic gate[175,178,293].

Modern science may benefit from computations based on molecular logic functions. The logic operation at the molecular level is performed using two input signals and one output signal. The Schiff base-based logic gates have a lot of promise for optical sensing, which opens up new possibilities for multidirectional memory device innovation in the future.

Das *et al.* prepared fluorescein-based Schiff base **154** as a fluorometric turn-on sensor for Zn^{2+} (Fig. 60 and Table 2).[195] In HEPES buffered ethanol–H_2O (9 : 1, v/v) solution, sensor **154** displayed fluorescence enhancement only with Zn^{2+} over other metal ions. Fluorescence titration of sensor **154** with Zn^{2+} revealed an increase in emission intensity at 520 nm (λ_{ex} = 375 nm) along with color change of the solution from colorless to greenish-yellow under UV light. The complexation of sensor **154** with Zn^{2+} through the imine group and –OH groups inhibits the PET process and C=N isomerization, leading to fluorescence enhancement by the CHEF effect. The binding constant was 2.86×10^4 M^{-1} for the 1 : 1 (**154**/Zn^{2+}) complex. The limit of detection was 1.59 μM for Zn^{2+}. Additionally, an INHIBIT type logic gate was designed using Zn^{2+} and EDTA as inputs and emission intensity at 520 nm as output at the molecular level (Fig. 65). Sensor **154** also found application in Zn^{2+} detection using TLC supported paper strips and in the bioimaging of intracellular Zn^{2+} ions in Vero cells (African green monkey kidney cells).

Das *et al.* constructed Schiff base sensor **155** using ethylenediamine and 2-hydroxyacetophenone and utilized it for Al^{3+} detection by fluorescence off–on mode (Fig. 60 and Table 2).[196]

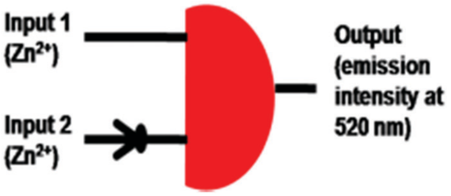

Fig. 65 Truth table and INHIBIT type logic gate representation with Zn^{2+} and EDTA as input and the emission intensity of sensor **154** at 520 nm as output at the molecular level. Reproduced with permission from ref. 195 Copyright 2019, Elsevier.

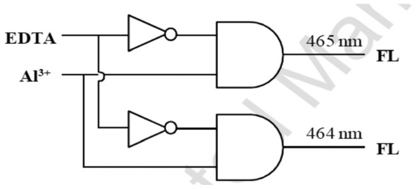

Fig. 66 Truth table and AND and NOT gate representation with Al^{3+} and EDTA as two inputs and emission intensity as output. Reproduced with permission from ref. 197 Copyright 2015, Elsevier.

In methanol–water (1 : 1, v/v) solution, sensor **155** exhibited weak emission in the 380 nm to 700 nm range (λ_{ex} = 370 nm). Upon the addition of Al^{3+}, sensor **155** underwent an increase in emission intensity along with red-shift. The binding constant was log β = 5.14 for 1 : 1 (**155** : Al^{3+}) stoichiometry. The limit of detection was 10 μM for Al^{3+}. The off–on fluorescence response could be attributed to inhibition of the PET process upon complexation of Al^{3+} with sensor **155**, resulting in fluorescence enhancement. The **155**–Al^{3+} complex further acted as an on–off type fluorescent sensor for PO_4^{3-}. An INHIBIT type logic gate was constructed utilizing Al^{3+} and PO_4^{3-} as two inputs. Sensor **155** found application in Al^{3+} determination in BSA and in rat L6 myoblast cells.

Gupta *et al.* synthesized sensors **156** and **157** for fluorescence-based detection of Al^{3+} (Fig. 60 and Table 2).[197] The fluorescence spectrum of sensors **156** and **157** (λ_{ex} = 375 nm) in methanol solution displayed fluorescence enhancement selectively with Al^{3+} over other tested metal ions and the emission maxima were centered at 465 nm and 464 nm for sensors **156** and **157**, respectively. The detection limit of sensors **156** and **157** was 0.525 μM and 2.38 μM, respectively for Al^{3+} ions. The binding constant was 6.64×10^3 M^{-1} and 7.29×10^3 M^{-1} for **156** : Al^{3+} (1 : 1) and **157** : Al^{3+} (1 : 1) complexes, respectively. The sensing mechanism could be attributed to the CHEF effect. A combination of AND and NOT gates was developed using Al^{3+} and EDTA as two inputs and emission intensity as output (Fig. 66).

Naskar *et al.* synthesized Schiff base sensor **158** using 2-amino-1-ethanol and salicyladehyde for Zn^{2+} detection in an aqueous medium (Fig. 60 and Table 2).[198] On excitation at 359 nm, sensor **158** exhibited emission maxima at 454 nm. In the presence of various metal ions, sensor **158** displayed strong fluorescence enhancement with Zn^{2+} and moderate response with Al^{3+}, whereas other metal ions had an insignificant effect. The limit of detection of sensor **158** for Zn^{2+} was 0.477 μM. The binding constant was 24.75×10^4 M^{-1} for 2 : 1 (**158**/Zn^{2+}) stoichiometry. The coordination of sensor **158** with Zn^{2+} caused inhibition of the ESIPT process and C═N isomerization, leading to fluorescence enhancement through the CHEF effect. An 'OR' logic gate and a 'Keypad lock' logic network were fabricated using Zn^{2+} and Al^{3+} as input with absorbance at 359 nm and emission at 454 nm as output (Fig. 67A and B). Additionally, sensor **158** found potential application in the fluorescence imaging of Zn^{2+} in rice seedlings.

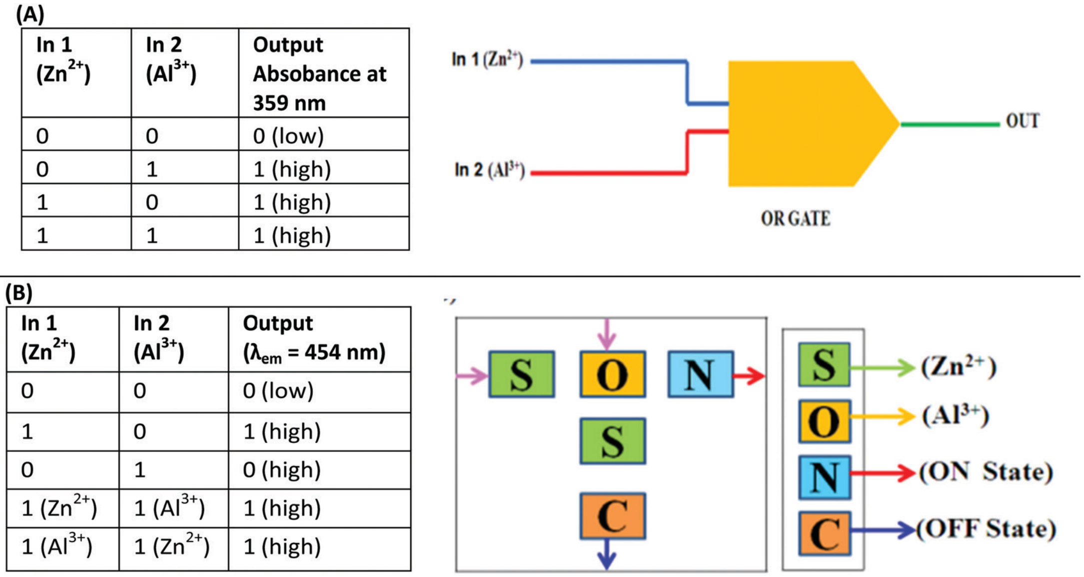
(A)

In 1 (Zn^{2+})	In 2 (Al^{3+})	Output Absobance at 359 nm
0	0	0 (low)
0	1	1 (high)
1	0	1 (high)
1	1	1 (high)

(B)

In 1 (Zn^{2+})	In 2 (Al^{3+})	Output (λ_{em} = 454 nm)
0	0	0 (low)
1	0	1 (high)
0	1	0 (high)
1 (Zn^{2+})	1 (Al^{3+})	1 (high)
1 (Al^{3+})	1 (Zn^{2+})	1 (high)

Fig. 67 (A) Truth table and OR gate representation with Zn^{2+} and Al^{3+} as inputs and absorbance at 359 nm as output. (B) Truth table for fluorescent keypad logic operation. Reproduced with permission from ref. 198 Copyright 2016, Elsevier.

Zn^{2+}	EDTA	Output (λ_{max} = 545 nm)
0	0	0
1	0	1
0	1	0
1	1	0
Cd^{2+}	**EDTA**	**Output (λ_{max} = 560 nm)**
0	0	0
1	0	1
0	1	0
1	1	0

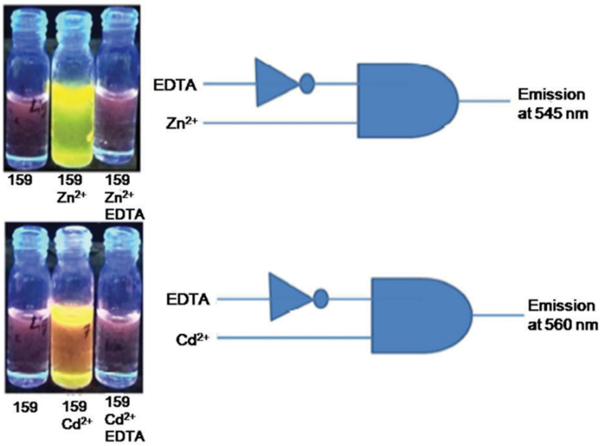

Fig. 68 Truth table and INHIBIT logic gate representation with the Zn^{2+} and Cd^{2+} complex of sensor **159** and EDTA as inputs. Reproduced with permission from ref. 199 Copyright 2018, Royal Society of Chemistry.

Purkait *et al.* synthesized Schiff base sensor **159** for fluorescence-based detection of Zn^{2+}, Cd^{2+}, and I^- (Fig. 60 and Table 2).[199] In DMSO–water (9 : 1 v/v) solution, sensor **159** was non-fluorescent (λ_{ex} = 482 nm). Among various tested metal ions, sensor **159** displayed fluorescence enhancement only with Zn^{2+} (λ_{em} = 545 nm) and Cd^{2+} (λ_{em} = 560 nm) along with naked eye detectable color change from colorless to bright yellow (for Zn^{2+}) and from colorless to orange color (for Cd^{2+}) under UV light illumination. The interaction of Zn^{2+}/Cd^{2+} with sensor **159** resulted in fluorescence enhancement due to the CHEF effect. The limit of detection was 2.7 nM (for Zn^{2+}) and 6.6 nM (for Cd^{2+}). The binding constant was 2.7×10^4 M^{-1} (for the **159**–Zn^{2+} (1 : 1) complex) and 0.96×10^4 M^{-1} (for the **159**–Cd^{2+} (1 : 1) complex). Upon addition of Na_2EDTA to the solution of the sensor **159**–Zn^{2+}/Cd^{2+} complex, on–off type fluorescence response was observed, signifying reversibility and reusability of sensor **159**. An INHIBIT type logic gate was generated using Zn^{2+}/Cd^{2+} and EDTA as input and emission intensity as output (Fig. 68). Sensor **159** also displayed practical application in sensing Zn^{2+} and Cd^{2+} in TLC plates and in drinking water.

Vinoth Kumar *et al.* synthesized Schiff base **160** as a turn-on sensor for Ni^{2+} (Fig. 60 and Table 2).[200] In acetonitrile solution, sensor **160** showed an off–on type fluorescence response with Ni^{2+}, whereas other metal ions had an insignificant effect. Fluorescence titration of sensor **160** with Ni^{2+} revealed a continuous increase in fluorescence intensity at 542 nm (λ_{ex} = 400 nm) upon addition of an increasing concentration of Ni^{2+} (0–60 μM), attributed to the CHEF effect. The detection limit was 8.67 nM for Ni^{2+} and the association constant was 4.18×10^5 M^{-1} for the **160**–Ni^{2+} (1 : 1) complex. Upon addition of Na_2EDTA to the solution of the sensor **160**–Ni^{2+} complex, fluorescence quenching was observed, suggesting reversibility and reusability of sensor **160**. Additionally, the molecular logic gate of AND, OR, NOT, and NOR type and truth table were created based on Ni^{2+} and EDTA as input and absorbance and emission intensity at 428 nm and 542 nm as output. Sensor **160** found application in the fluorescence imaging of intracellular Ni^{2+} in HeLa cells.

Jothi *et al.* synthesized naphthalimide-based Schiff base **161** for detection of Fe^{3+} based on a fluorometric method (Fig. 60 and Table 2).[201] In the acetonitrile–water (7 : 3) mixture, sensor **161** showed strong emission at 531 nm (λ_{ex} = 344 nm). The fluorescence titration of sensor **161** with Fe^{3+} revealed a gradual decrease in fluorescence intensity with the addition of an increasing concentration of Fe^{3+}. The limit of detection was 0.81 μM for Fe^{3+}. The stoichiometry of the complex was 1 : 1 (**161**/Fe^{3+}) and the binding constant was 2.49×10^4 M^{-1}. The sensing mechanism could be attributed to blockage of ICT and C=N isomerization upon complexation of sensor **161** with Fe^{3+}. Furthermore, NOT gate, OR gate logic circuit, and truth table were constructed using Fe^{3+} and EDTA as input and emission intensity at 531 nm as

Input 1 Fe^{3+}	Input 2 EDTA	Output FL
0	0	1
1	0	0
0	1	1
1	1	1

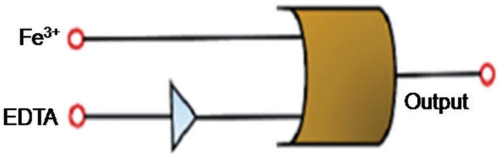

Fig. 69 Truth table and logic gate representation with $Fe^{3+}$and EDTA as inputs. Reproduced with permission from ref. 201 Copyright 2021, Royal Society of Chemistry.

output (Fig. 69). Additionally, sensor **161** demonstrated potential application in detecting Fe^{3+} in test paper and water samples, and in fluorescent bioimaging.

4. Conclusion and future opportunities

Metal ions are ubiquitous in nature, and up to certain concentrations as fixed by WHO and EPA they are non-toxic. In fact, some metal ions are essential for the normal functioning of living organisms. Nowadays, researchers are using Schiff base metal ion complexes for productive purposes owing to their outstanding applications in optoelectronic systems. However, with the increase in their concentration due to industrialization and urbanization, metal ions have shown toxic effects on human health and the environment. Therefore, their detection is crucial, which is challenging. This review summarized the recent advances in fluorescent Schiff base sensors for metal ion detection in the past six years.

The commonly used mechanisms for metal ion detection include self-assembly/disassembly, aggregation/disaggregation, photo-induced electron transfer (PET), intra/intermolecular charge transfer (ICT), metal to ligand charge transfer (MLCT), ligand to metal charge transfer (LMCT), Förster resonance energy transfer (FRET), excited state intramolecular proton transfer (ESIPT), inner filter effect (IFE), metal-induced chemical change and C=N isomerization. Metal ions upon coordination with Schiff base sensors generally show fluorescence enhancement or quenching leading to the CHEF or CHEQ effect, respectively. However, for a few systems, ratiometric fluorescence change was also observed. Usually, paramagnetic metal ions such as Cu^{2+} and Fe^{3+} act as a fluorescence quencher and show CHEQ effects when bound with chemosensors. However, there are several reports wherein fluorescence enhancement was also observed with these metal ions. Additionally, the ESIPT process was associated with the sensors containing the salicylimine group. Because of the free rotation around the C=N bond, Schiff base-based sensors may show the AIE phenomenon. Schiff bases commonly include hydrazone, acyl hydrazone, salicylimine, azine, and other groups, and provide nitrogen and oxygen atoms for coordination with metal ions.

Due to the global existence of metal ions, environmental monitoring and biomedical application are the most common practical application of Schiff base sensors. Other applications of fluorescent Schiff base sensors include multi-metal ion sensors, a sequential sensor for other ions, and optoelectronic systems. The molecular switching properties of Schiff base sensors have been applied in the construction of molecular keypads and logic gates.

The development of fluorescent Schiff base sensors and their commercial applications will always be of immense interest to researchers. Although existing results are plentiful, future efforts need to be undertaken in the following aspects. First, the main drawbacks of as-developed fluorescent Schiff base sensors are instability and poor water solubility in an aqueous medium. Except for sensors **2**, **8**, **11**, **22**, **35**, **45**, **58**, **84**, **112**, **117**, **118**, and **158**, the optical properties of Schiff base sensors were studied in either H_2O-DMF/DMSO/THF/CH_3CN/ethanol/methanol buffered binary mixtures or in CH_3CN, ethanol, methanol solutions (Table 2), thus limiting their application in biological and environmental systems. Second, from Table 2 we can conclude that most of the work has been done on the detection of Al^{3+}, Cu^{2+}, and Zn^{2+}, and insufficient literature is available for other important and toxic metal ions. Third, Schiff base sensors can be applied for fluorescence-based speciation of metal ions such as Fe^{2+}/Fe^{3+}, As^{3+}/As^{5+}, Cr^{3+}/Cr^{4+}, *etc.* Fourth, the selectivity and sensitivity of the Schiff base sensor need to be improved. Fifth, although there are several practical applications of Schiff base sensors, so far there have been no available well known commercial applications because of the poor stability (as Schiff bases are prone to hydrolysis, the carbonyl and amine groups might be regenerated on hydrolysis), pH sensitivity, and decrease in fluorescence of Schiff base sensors with time. Therefore, the prototype should be made for the commercialization of these techniques. This will be useful for diagnostic purposes and pollutant detection on-site. Sixth, the majority of the developed sensors are based on one-photon excitation and few reports are available for two-photon fluorescent sensors. In comparison, two-photon fluorescent probes offer several advantages over conventional one-photon fluorescent probes such as decreased photo-damage to biological samples, deeper penetration into cells, tissues, and organelles, and minimization of background interference. Therefore, future efforts should be on the development of two-photon fluorescent sensors.

Although fluorescent-based Schiff base sensors encounter many challenges in terms of both exploratory and practical application, by taking into consideration the above-mentioned aspects in the sensor design and application-oriented research work, we believe that fluorescent Schiff base sensors can be utilized as important materials in the upcoming days and their commercial availability will be expected in the future.

Conflicts of interest

There are no conflicts to declare.

References

1 K. S. Egorova and V. P. Ananikov, *Organometallics*, 2017, **36**, 4071–4090.

2 J. K. Fawell, E. Ohanian, M. Giddings, P. Toft, Y. Magara and P. Jackson, *Inorganic Tin in Drinking-water WHO, Guidelines for Drinking-water Quality*, 2004.

3 F. S. Al-fartusie and S. N. Mohssan, *Indian J. Adv. Chem. Sci.*, 2017, **5**, 127–136.

4 A. L. Berhanu, Gaurav, I. Mohiuddin, A. K. Malik, J. S. Aulakh, V. Kumar and K.-H. Kim, *Trends Anal. Chem.*, 2019, **116**, 74–91.

5 M. Kumar and A. Puri, *Indian J. Occup. Environ. Med.*, 2012, **16**, 40–44.

6 T. Gong, J. Liu, X. Liu, J. Liu, J. Xiang and Y. Wu, *Food Chem.*, 2016, **213**, 306–312.

7 J. Dalmieda and P. Kruse, *Sensors*, 2019, **19**, 5134.

8 Y. Lu, X. Liang, C. Niyungeko, J. Zhou, J. Xu and G. Tian, *Talanta*, 2018, **178**, 324–338.

9 L. Cui, J. Wu and H. Ju, *Biosens. Bioelectron.*, 2015, **63**, 276–286.

10 S. Sikdar and M. Kundu, *ChemBioEng Rev.*, 2018, **5**, 18–29.

11 M. H. Chua, H. Zhou, Q. Zhu, B. Z. Tang and J. W. Xu, *Mater. Chem. Front*, 2021, **5**, 659–708.

12 J. Zhang, L. Xu and W. Wong, *Coord. Chem. Rev.*, 2018, **355**, 180–198.

13 S. Sandhu, R. Kumar, N. Tripathi, H. Singh, P. Singh and S. Kumar, *Sens. Actuators, B*, 2017, **241**, 8–18.

14 N. Tripathi, P. Singh and S. Kumar, *New J. Chem.*, 2017, **41**, 8739–8747.

15 N. Tripathi and M. K. Goshisht, *Aggregation of Luminophores in Supramolecular Systems: From Mechanisms to Applications*, CRC Press, Taylor Fr., 2020, pp. 1–220.

16 N. Tripathi, R. Kumar, P. Singh and S. Kumar, *Sens. Actuators, B*, 2017, **246**, 1001–1010.

17 M. K. Goshisht and N. Tripathi, *J. Mater. Chem. C*, 2021, **9**, 9820–9850.

18 N. Tripathi, P. Singh, V. Luxami, D. Mahajan and S. Kumar, *Sens. Actuators, B*, 2018, **270**, 552–561.

19 N. Tripathi, S. Sandhu, P. Singh, A. Mahajan, M. Kaur and S. Kumar, *Sens. Actuators, B*, 2016, **231**, 79–87.

20 P. Sabari and M. Ravikanth, *J. Chem. Sci.*, 2021, **133**, 59–67.

21 M. Sahu, A. K. Manna and G. K. Patra, *Inorg. Chim. Acta*, 2021, **517**, 120199.

22 X. Liu, X. Peng, F. Xu, L. Wang and M. Liu, *Russ. J. Gen. Chem.*, 2021, **91**, 1093–1098.

23 S. D. Pradeep, D. Sebastian, A. K. Gopalakrishnan, D. K. Manoharan, D. T. Madhusudhanan and P. V. Mohanan, *J. Fluoresc.*, 2021, **31**, 1113–1123.

24 Y. Xing, Z. Liu, B. Li, L. Li, X. Yang and G. Zhang, *Sens. Actuators, B*, 2021, **347**, 130497.

25 M. Liu, H. Yang, D. Li, Q. Yao, H. Wang, Z. Zhang and J. Dou, *Inorg. Chim. Acta*, 2021, **522**, 120384.

26 C. Pan, K. Wang, S. Ji, H. Wang, Z. Li, H. He, Y. Huo and Y. Huo, *RSC Adv.*, 2017, **7**, 36007–36014.

27 J. Harathi and K. Thenmozhi, *Mater. Chem. Front*, 2020, **4**, 1471–1482.

28 C. Chen, P. Hung, C. Wan and A. Wu, *Inorg. Chem. Commun.*, 2013, **38**, 74–77.

29 X. Feng, Y. Li, X. He, H. Liu, Z. Zhao, R. T. K. Kwok, M. R. J. Elsegood, J. W. Y. Lam and B. Z. Tang, *Adv. Funct. Mater.*, 2018, **28**, 1802833.

30 A. Mukherjee and M. Chakravarty, *New J. Chem.*, 2020, **44**, 6173–6181.

31 V. Kachwal, P. Alam, H. R. Yadav, S. S. Pasha, A. R. Choudhury and I. R. Laskar, *New J. Chem.*, 2018, **42**, 1133–1140.

32 N. Chakraborty, A. Chakraborty and S. Das, *J. Lumin.*, 2018, **199**, 302–309.

33 J. Xiong, Z. Li, J. Tan, S. Ji, J. Sun, X. Li and Y. Huo, *Analyst*, 2018, **143**, 4870–4886.

34 M. Shyamal, S. Maity, A. Maity, R. Maity, S. Roy and A. Misra, *Sens. Actuators, B*, 2018, **263**, 347–359.

35 W. Chen, H. Xu, L. Ju and H. Lu, *Tetrahedron*, 2021, **88**, 132123.

36 J. Qin, T. Li, B. Wang, Z. Yang and L. Fan, *Synth. Met.*, 2014, **195**, 141–146.

37 R. Azadbakht and S. Rashidi, *Spectrochim. Acta, Part A*, 2014, **127**, 329–334.

38 R. Bhaskar and S. Sarveswari, *ChemistrySelect*, 2020, **5**, 4050–4057.

39 A. Kumar, S. Mondal, K. S. Kayshap, S. K. Hira, P. P. Manna, W. Dehaend and S. Dey, *New J. Chem.*, 2018, **42**, 10983–10988.

40 Y. Wang, X. Hao, L. Liang, L. Gao, X. Ren, Y. Wu and H. Zhao, *RSC Adv.*, 2020, **10**, 6109–6113.

41 Y. Wang, H. Wu, W. Wu, S. Li, Z. Xu, Z. Xu, Y. Fan, X. Zhao and B. Liu, *Sens. Actuators, B*, 2018, **260**, 106–115.

42 D. Aydin, S. Dinckan, S. Nihan, K. Elmas, T. Savran, F. N. Arslan and I. Yilmaz, *Food Chem.*, 2021, **337**, 127659.

43 O. Alici and D. Aydin, *J. Photochem. Photobiol., A*, 2021, **404**, 112876.

44 H. Yu, J. Zhi, Z. Chang, T. Shen, W. Ding, X. Zhang and J. Wang, *Mater. Chem. Front.*, 2019, **3**, 151–160.

45 Y. Yang, C. Gao, N. Zhang and D. Dong, *Sens. Actuators, B*, 2016, **222**, 741–746.

46 H. Fang, G. Cai, Y. Hu and J. Zhang, *Chem. Commun.*, 2018, **54**, 3045–3048.

47 H. Yao, J. Wang, Q. Zhou, X.-W. Guan, Y.-Q. Fan, Y.-M. Zhang, T.-B. Wei and Q. Lin, *Soft Matter*, 2018, **14**, 8390–8394.

48 A. C. Sedgwick, L. Wu, H. H. Han, S. D. Bull, X. P. He, T. D. James, J. L. Sessler, B. Z. Tang, H. Tian and J. Yoon, *Chem. Soc. Rev.*, 2018, **47**, 8842–8880.

49 J. Zhao, S. Ji, Y. Chen, H. Guo and P. Yang, *Phys. Chem. Chem. Phys.*, 2012, **14**, 8803–8817.

50 S. Gupta and M. D. Milton, *New J. Chem.*, 2018, **42**, 2838–2849.

51 V. Kachwal, I. S. V. Krishna, L. Fageria, J. Chaudhary, R. K. Roy, R. Chowdhury and I. R. Laskar, *Analyst*, 2018, **143**, 3741–3748.

52 Q. Yu, X. Zhang, S.-T. Wu, H. Chen, Q.-L. Zhang, H. Xu, Y.-L. Huang, B.-X. Zhu and X.-L. Ni, *Chem. Commun.*, 2020, **56**, 2304–2307.

53 S. Sharma, S. Virk, P. Pradeep and A. Dhir, *Eur. J. Inorg. Chem.*, 2017, 2457–2463.

54 A. Sen Gupta, K. Paul and V. Luxami, *Sens. Actuators, B*, 2017, **246**, 653–661.

55 Y. Jia and J. Li, *Chem. Rev.*, 2015, **115**, 1597–1621.

56 F. Faridbod, M. R. Ganjali, R. Dinarvand, P. Norouzi and S. Riahi, *Sensors*, 2008, **8**, 1645–1703.

57 A. Q. Alorabi, M. Abdelbaset and S. A. Zabin, *Chemosensors*, 2020, **8**, 1.

58 M. J. Reimann, D. R. Salmon, J. T. Horton, E. C. Gier and L. R. Jefferies, *ACS Omega*, 2019, **4**, 2874–2882.

59 A. Singh and P. Barman, *Top. Curr. Chem.*, 2021, **379**, 29.
60 W. Liping, J. Shibo, Z. Weifeng, L. I. U. Yunqi and Y. Gui, *Chinese Sci. Bull.*, 2013, **58**, 2733–2740.
61 İ. Sıdır, Y. G. Sıdır, H. Berber and F. Demiray, *J. Mol. Struct.*, 2019, **1176**, 31–46.
62 P. H. A. Nayak, H. S. B. Naik, H. B. Teja, B. R. Kirthan, R. Viswanath, P. H. A. Nayak, H. S. B. Naik, H. B. Teja, B. R. Kirthan and R. Viswanath, *Mol. Cryst. Liq. Cryst.*, 2021, 1–7.
63 A. Sakthivel, K. Jeyasubramanian, B. Thangagiri and J. D. Raja, *J. Mol. Struct.*, 2020, **1222**, 128885.
64 S. K. Patil and D. Das, *ChemistrySelect*, 2017, **2**, 6178–6186.
65 M. T. Kaczmarek, M. Zabiszak, M. Nowak and R. Jastrzab, *Coord. Chem. Rev.*, 2018, **370**, 42–54.
66 D. Udhayakumari and V. Inbaraj, *J. Fluoresc.*, 2020, **30**, 1203–1223.
67 S. Shekhar, A. M. Khan, S. Sharma, B. Sharma and A. Sarkar, *Emergent Mater.*, 2021, DOI: 10.1007/s42247-021-00234-1.
68 M. Kaur, S. Kumar, M Yusuf, J. Lee, R. J. C. Brown, K.-H. Kim and A. K. Malika, *Coord. Chem. Rev.*, 2021, **449**, 214214.
69 H. Wan, Q. Xu, P. Gu, H. Li, D. Chen, N. Li, J. He and J. Lu, *J. Hazard. Mater.*, 2021, **403**, 123656.
70 C. C. Vidyasagar, B. M. Muñoz Flores, V. M. Jiménez-Pérez and P. M. Gurubasavaraj, *Mater. Today Chem.*, 2019, **11**, 133–155.
71 C. Immanuel David, G. Prabakaran and R. Nandhakumar, *Microchem. J.*, 2021, **169**, 106590.
72 W.-N. Wu, P.-D. Mao, Y. Wang, X.-J. Mao, Z.-Q. Xu, Z.-H. Xu, X.-L. Zhao, Y.-C. Fan and X.-F. Hou, *Sens. Actuators, B*, 2018, **258**, 393–401.
73 P. Singh, H. Singh, V. Vanita and R. Sharma, *ChemistrySelect*, 2016, **1**, 6880–6887.
74 W. Dong, S. F. Akogun, Y. Zhang, Y. Sun and X. Dong, *Sens. Actuators, B*, 2017, **238**, 723–734.
75 K. Rout, A. K. Manna, M. Sahu, J. Mondal, S. K. Singh and G. K. Patra, *RSC Adv.*, 2019, **9**, 25919–25931.
76 M. Pannipara, A. G. Al-Sehemi, A. Kalam, A M Asiri and M. N. Arshad, *Spectrochim. Acta, Part A*, 2017, **183**, 84–89.
77 S. Bhardwaj, N. Maurya and A. K. Singh, *Sens. Actuators, B*, 2018, **260**, 753–762.
78 J. Yang, J. Chai, B. Yang and B. Liu, *Spectrochim. Acta, Part A*, 2019, **211**, 272–279.
79 P. Puri, G. Kumar, K. Paul and V. Luxami, *New J. Chem.*, 2018, **42**, 18550–18558.
80 A. Abbasi and M. Shakir, *New J. Chem.*, 2018, **42**, 293–300.
81 T. Hu, L. Wang, J. Li, Y. Zhao, J. Cheng, W. Li, Z. Chang and C. Sun, *Inorg. Chim. Acta*, 2021, **524**, 120421.
82 G. Wang, J. Qin, L. Fan, C. Li and Z. Yang, *J. Photochem. Photobiol., A*, 2016, **314**, 29–34.
83 S. M. Saleh and R. F. M. Elshaarawy, *RSC Adv.*, 2016, **6**, 68709–68718.
84 H. Wang, X. Xu, J. Yin, Z. Zhang and L. Xue, *ChemistrySelect*, 2021, **6**, 1–7.
85 Y.-J. Chang, S.-S. Wu, C.-H. Hu, C. Cho, M. X. Kao and A.-T. Wu, *Inorg. Chim. Acta*, 2015, **432**, 25–31.
86 S. M. Hossain, K. Singh, A. Lakma, R. N. Pradhan and A. K. Singh, *Sens. Actuators, B*, 2017, **239**, 1109–1117.
87 C. Li, J. Qin, B. Wang, L. Fan, J. Yan and Z. Yang, *J. Fluoresc.*, 2016, **26**, 345–353.
88 C. Li, J. Qin, G. Wang, B. Wang, A. Fu and Z. Yang, *Inorg. Chim. Acta*, 2015, **430**, 91–95.
89 C. Liu, Z. Yang, L. Fan, X. Jin, J. An, X. Cheng and B. Wang, *J. Lumin.*, 2013, **158**, 172–175.
90 L. Liu and Z. Yang, *Inorg. Chim. Acta*, 2018, **469**, 588–592.
91 J. Qin and Z. Yang, *J. Photochem. Photobiol., A*, 2015, **303–304**, 99–104.
92 J.-C. Qin, X. Cheng, K. Yu, R. Fang, M. Wang and Z. Yang, *Anal. Methods*, 2015, **7**, 6799–6803.
93 W. Ruo, J. Guang-qi and L. Xiao-hong, *Inorg. Chim. Acta*, 2017, **455**, 247–253.
94 S. K. Shoora, A. K. Jain and V. K. Gupta, *Sens. Actuators, B*, 2015, **216**, 86–104.
95 S. J. Zhang, H. Li, C. L. Gong, Z. J. Wang, Z. Y. Wu and F. Wang, *Synth. Met.*, 2016, **217**, 37–42.
96 M. Kumar, A. Kumar, S. Kishor, S. Kumar, N. Manav, A. K. Bhagi, S. Kumar and R. P. John, *J. Mol. Struct.*, 2022, **1247**, 131257.
97 M. Wang, L. Lu, W. Song, X. Wang, T. Sun, J. Zhu and J. Wang, *J. Lumin.*, 2021, **233**, 117911.
98 F. Kolcu, D. Erdener and İ. Kaya, *Synth. Met.*, 2021, **272**, 116668.
99 G. B. Chalmardi, M. Tajbakhsh, A. Bekhradnia and R. Hosseinzadeh, *Inorg. Chim. Acta*, 2017, **462**, 241–248.
100 G. Babaei, M. Tajbakhsh, N. Hasani and A. Bekhradnia, *Tetrahedron*, 2018, **74**, 2251–2260.
101 Y. He, J. Yin and G. Wang, *Chem. Heterocycl. Compd.*, 2018, **54**, 146–152.
102 B. Li, D. Zhang and F. Tian, *Luminescence*, 2017, **32**, 1567–1573.
103 S. Santhoshkumar, K. Velmurugan, J. Prabhu, G. Radhakrishnan and R. Nandhakumar, *Inorg. Chim. Acta*, 2016, **439**, 1–7.
104 B. Zhao, T. Liu, Y. Fang, L. Wang, B. Song and Q. Deng, *Tetrahedron Lett.*, 2016, **57**, 4417–4423.
105 J. Zhang, Y. Liu, Q. Fei, H. Shan, F. Chen, Q. Liu, G. Chai, G. Feng and Y. Huan, *Sens. Actuators, B*, 2017, **239**, 203–210.
106 S. Dalbera, S. Kulovi and S. Dalai, *ChemistrySelect*, 2018, **3**, 6561–6569.
107 S. Carlos, M. C. Nunes, L. De Boni, G. S. Machado and F. S. Nunes, *J. Photochem. Photobiol., A*, 2017, **348**, 41–46.
108 Y. Fu, C. Fan, G. Liu and S. Pu, *Sens. Actuators, B*, 2017, **239**, 295–303.
109 J. Kumar, P. K. Bhattacharyya and D. Kumar, *Spectrochim. Acta, Part A*, 2015, **138**, 99–104.
110 F. N. Moghadam, M. Amirnasr, S. Meghdadi, K. Eskandari, A. Buchholz and W. Plass, *Spectrochim. Acta, Part A*, 2019, **207**, 6–15.
111 P. Torawane, S. K. Sahoo, A. Borse and A. Kuwar, *Luminescence*, 2017, **32**, 1426–1430.
112 X. Wang, T. Xu and H. Duan, *Sens. Actuators, B*, 2015, **214**, 138–143.

113 J. Yin, Q. Bing, L. Wang and G. Wang, *Spectrochim. Acta, Part A*, 2018, **189**, 495–501.

114 M. Gao, C. Xing, X. Jiang, L. Xu, P. Li and C. Der Hsiao, *Luminescence*, 2021, **36**, 951–957.

115 J. Zhu, Y. Zhang, Y. Chen, T. Sun, Y. Tang, Y. Huang, Q. Yang, D. Ma, Y. Wang and M. Wang, *Tetrahedron Lett.*, 2017, **58**, 365–370.

116 M. Kumar, A. Kumar, M. K. Singh, S. K. Sahu and R. P. John, *Sens. Actuators, B*, 2017, **241**, 1218–1223.

117 C. Liu, Q. Zhou, Y. Li, L. V. Garner, S. P. Watkins, L. J. Carter, J. Smoot, A. C. Gregg, A. D. Daniels, S. Jervey and D. Albaiu, *ACS Cent. Sci.*, 2020, **6**, 315–331.

118 J. Yan, L. Fan, J. Qin, C. Li and Z. Yang, *Tetrahedron Lett.*, 2016, **57**, 2910–2914.

119 S. O. Tümay, *ChemistrySelect*, 2021, **6**, 10561–10572.

120 F. Lei, W. Shi, J. Ma, Y. Chen, F. Kui, Y. Hui and Z. Xie, *Sens. Actuators, B*, 2016, **237**, 563–569.

121 D. Singhal, N. Gupta and A. K. Singh, *RSC Adv.*, 2015, **5**, 65731–65738.

122 Q. Su, Q. Niu, T. Sun and T. Li, *Tetrahedron Lett.*, 2016, **57**, 4297–4301.

123 V. Tekuri, S. K. Sahoo and D. R. Trivedi, *Spectrochim. Acta, Part A*, 2019, **218**, 19–26.

124 X. Wan, H. Ke, J. Tang and G. Yang, *Talanta*, 2019, **199**, 8–13.

125 D. Mohanasundaram, R. Bhaskar, G. Gangatharan, V. Kumar, J. Rajesh and G. Rajagopal, *Microchem. J.*, 2021, **164**, 106030.

126 H. H. Hammud, S. El, G. Sonji, N. Sonji and K. H. Bouhadir, *Spectrochim. Acta, Part A*, 2015, **150**, 94–103.

127 M. Saleem, C. H. Khang and K. H. Lee, *J. Fluoresc.*, 2016, **26**, 11–22.

128 Y. Sie, C. Wan and A. Wu, *RSC Adv.*, 2017, **7**, 2460–2465.

129 T. Simon, M. Shellaiah, V. Srinivasadesikan, C.-C. Lin, F.-H. Ko, K. W. Sun and M.-C. Lin, *Sens. Actuators, B*, 2016, **231**, 18–29.

130 X. Tang, J. Han, Y. Wang, L. Ni, X. Bao, L. Wang and W. Zhang, *Spectrochim. Acta, Part A*, 2017, **173**, 721–726.

131 S. Zhang, X. Wu, Q. Niu, Z. Guo and T. Li, *J. Fluoresc.*, 2017, **27**, 729–737.

132 X. Zhu, Y. Duan, P. Li, H. Fan, T. Han and X. Huang, *Anal. Methods*, 2019, **11**, 642–647.

133 J. Xue, L. Tian and Z. Yang, *J. Photochem. Photobiol., A*, 2019, **369**, 77–84.

134 S. Y. Lee, K. H. Bok, T. G. Jo, S. Y. Kim and C. Kim, *Inorg. Chim. Acta*, 2017, **461**, 127–135.

135 Y. Dong, R. Fan, W. Chen, P. Wang and Y. Yang, *Dalton Trans.*, 2017, **46**, 6769–6775.

136 M. Tajbakhsh, G. B. Chalmardi, A. Bekhradnia, R. Hosseinzadeh, N. Hasani and M. A. Amiri, *Spectrochim. Acta, Part A*, 2018, **189**, 22–31.

137 S. Zhang, Q. Niu, L. Lan and T. Li, *Sens. Actuators, B*, 2017, **240**, 793–800.

138 W. Zhu, L. Yang, M. Fang, Z. Wu, Q. Zhang and F. Yin, *J. Lumin.*, 2015, **158**, 38–43.

139 J. Fu, B. Li, H. Mei, Y. Chang and K. Xu, *Spectrochim. Acta, Part A*, 2020, **227**, 117678.

140 A. Gomathi, P. Viswanathamurthi and K. Natarajan, *J. Photochem. Photobiol., A*, 2019, **370**, 75–83.

141 J. Qiu, S. Jiang, B. Lin, H. Guo and F. Yang, *Dyes Pigm.*, 2019, **170**, 107590.

142 Y. Xu, H. Wang, J. Zhao, X. Yang, M. Pei, G. Zhang, Y. Zhang and L. Lin, *J. Photochem. Photobiol., A*, 2019, **383**, 112026.

143 Z.-G. Wang, X.-J. Ding, Y.-Y. Huang, X.-J. Yan, B. Ding, Q.-Z. Li, C.-Z. Xie and J.-Y. Xu, *Dyes Pigm.*, 2020, **175**, 108156.

144 C. Patra, C. Sen, A. Das Mahapatra, D. Chattopadhyay, A. Mahapatra and C. Sinha, *J. Photochem. Photobiol., A*, 2017, **341**, 97–107.

145 R. Mehta, P. Kaur, D. Choudhury, K. Paul and V. Luxami, *J. Photochem. Photobiol., A*, 2019, **380**, 111851.

146 I. Kaur, P. Kaur and K. Singh, *Sens. Actuators, B*, 2018, **257**, 1083–1092.

147 S. K. Sheet, B. Sen, R. Thounaojam, K. Aguan and S. Khatua, *J. Photochem. Photobiol., A*, 2017, **332**, 101–111.

148 Y. Mu, C. Zhang, Z. Gao, X. Zhang, Q. Lu, J. Yao and S. Xing, *Synth. Met.*, 2020, **262**, 116334.

149 Z. Salarvand, M. Amirnasr and S. Meghdadi, *J. Lumin.*, 2019, **207**, 78–84.

150 A. Saravanan, G. Subashini, S. Shyamsivappan, T. Suresh, K. Kadirvelu, N. Bhuvanesh, R. Nandhakumar and P. S. Mohan, *J. Photochem. Photobiol., A*, 2018, **364**, 424–432.

151 A. K. Bhanja, C. Patra, S. Mondal, D. Ojha, D. Chattopadhyay and C. Sinha, *RSC Adv.*, 2015, **5**, 48997–49005.

152 X. Chen, W. Sun, Y. Bai, F. Zhang, J. Zhao and X. Ding, *Spectrochim. Acta, Part A*, 2018, **191**, 566–572.

153 S. Feng, Q. Gao, X. Gao, J. Yin and Y. Jiao, *Inorg. Chem. Commun.*, 2019, **102**, 51–56.

154 L. Hu, H. Wang, B. Fang, Z. Hu, Q. Zhang, X. Tian, H. Zhou, J. Wu and Y. Tian, *Sens. Actuators, B*, 2017, **251**, 993–1000.

155 Y. Huang, F. Wang, S. Mu, X. Sun, Q. Li, C. Xie and H. Liu, *Spectrochim. Acta, Part A*, 2020, **243**, 118754.

156 Y. Jiao, X. Liu, L. Zhou, H. He, P. Zhou and C. Duan, *Sens. Actuators, B*, 2017, **247**, 950–956.

157 Z. Li, H. Su, K. Zhou, B. Yang, T. Xiao, X. Sun, J. Jiang and L. Wang, *Dyes Pigm.*, 2018, **149**, 921–926.

158 B. Liu, P. Wang, J. Chai, X. Hu, T. Gao, J. Chao, T. Chen and B. Yang, *Spectrochim. Acta, Part A*, 2016, **168**, 98–103.

159 B. Naskar, R. Modak, Y. Sikdar, D. K. Maiti, A. Bauzá, A. Frontera, A. Katarkar, K. Chaudhuri and S. Goswami, *Sens. Actuators, B*, 2017, **239**, 1194–1204.

160 C. Patra, A. K. Bhanja, C. Sen, D. Ojha, D. Chattopadhyay, A. Mahapatra and C. Sinha, *Sens. Actuators, B*, 2016, **228**, 287–294.

161 M. Shellaiah, Y. C. Rajan, P. Balu and A. Murugan, *New J. Chem.*, 2015, **39**, 2523–2531.

162 T. Simon, M. Shellaiah, V. Srinivasadesikan, C.-C. Lin, F.-H. Ko, K. W. Sun and M.-C. Lin, *New J. Chem.*, 2016, **40**, 6101–6108.

163 J. Tian, X. Yan, H. Yang and F. Tian, *RSC Adv.*, 2015, **5**, 107012–107019.
164 H. Tian, X. Qiao, Z. Zhang, C. Xie, Q. Li and J. Xu, *Spectrochim. Acta, Part A*, 2019, **207**, 31–38.
165 E. Wang, L. Pang, Y. Zhou, J. Zhang, F. Yu, H. Qiao and X. Pang, *Biosens. Bioelectron.*, 2016, **77**, 812–817.
166 F.-Ur-Rahman, A. Ali, R. Guo, J. Tian, H. Wang, Z.-T. Li and D.-W. Zhang, *Sens. Actuators, B*, 2015, **211**, 544–550.
167 Y. Yang, S. Ma, Y. Zhang, J. Ru, X. Liu and H. Guo, *Spectrochim. Acta, Part A*, 2018, **199**, 202–208.
168 J. Zhu, L. Lu, M. Wang, T. Sun, Y. Huang, C. Wang, W. Bao, M. Wang, F. Zou and Y. Tang, *Tetrahedron Lett.*, 2020, **61**, 151893.
169 L. Subha, C. Balakrishnan, S. Natarajan, M. Theetharappan, B. Subramanian and M. A. Neelakantan, *Spectrochim. Acta, Part A*, 2016, **153**, 249–256.
170 B. K. Kundu, P. Mandal, B. G. Mukhopadhyay, R. Tiwari, D. Nayak, R. Ganguly and S. Mukhopadhyay, *Sens. Actuators, B*, 2019, **282**, 347–358.
171 A. Ghorai, J. Mondal, R. Saha, S. Bhattacharya and G. K. Patra, *Anal. Methods*, 2016, **8**, 2032–2040.
172 J. Kumar, M. J. Sarma, P. Phukan and D. K. Das, *Dalton Trans.*, 2015, **44**, 4576–4581.
173 A. Ghorai, J. Mondal, R. Chandra and G. K. Patra, *Dalton Trans.*, 2015, **44**, 13261–13271.
174 M. Liu, H. Yang, D. Li, Q. Yao, H. Wang, Z. Zhang and J. Dou, *Inorg. Chim. Acta*, 2021, **522**, 120384.
175 C. Liu, X. Liu, X. Ge, Q. Wang, L. Zhang, W. Shang, Y. Zhang, X. A. Yuan, L. Tian, Z. Liu and J. You, *Dalton Trans.*, 2020, **49**, 5988–5998.
176 N. H. Kim, J. Lee, S. Park, J. Jung and D. Kim, *Sensors*, 2019, **19**, 2500.
177 K. S. M. Salih, A. M. Shraim, S. R. Al-Mhini, R. E. Al-Soufi and I. Warad, *Emergent Mater.*, 2021, **4**, 423–434.
178 S. Xue, Z. Xie, Y. Wen, J. He, Y. Liu and W. Shi, *ChemistrySelect*, 2021, **6**, 7123–7129.
179 H. Peng, Y. Han, N. Lin and H. Liu, *Opt. Mater.*, 2019, **95**, 109210.
180 Z. Guo, Q. Niu, T. Li, T. Sun and H. Chi, *Spectrochim. Acta, Part A*, 2019, **213**, 97–103.
181 L. Kang, Y.-T. Liu, N.-N. Li, Q.-X. Dang, Z.-Y. Xing, J.-L. Li and Y. Zhang, *J. Lumin.*, 2017, **186**, 48–52.
182 M. Kao, T. Chen, Y. Cai, C. Hu, Y. Liu, Y. Jhong and A. Wu, *J. Lumin.*, 2016, **169**, 156–160.
183 X. Zhang, L. Shen, Q. Zhang, X. Yang, Y. Huang, C. Redshaw and H. Xu, *Molecules*, 2021, **26**, 1233.
184 H. Peng, K. Shen, S. Mao, X. Shi, Y. Xu, S. O. Aderinto and H. Wu, *J. Fluoresc.*, 2017, **27**, 1191–1200.
185 K. Shen, S. Mao, X. Shi, F. Wang, Y. Xu, S. O. Aderinto and H. Wu, *Luminescence*, 2018, **33**, 54–63.
186 J. Zhu, Y. Zhang, L. Wang, T. Sun, M. Wang, Y. Wang, D. Ma, Q. Yang and Y. Tang, *Tetrahedron Lett.*, 2016, **57**, 3535–3539.
187 H. Sun, Y. Jiang, J. Nie, J. Wei, B. Miao, Y. Zhao, L. Zhang and Z. Ni, *Mater. Chem. Front.*, 2021, **5**, 347–354.
188 H. Sun, J. Li, F. Han, R. Zhang, Y. Zhao, B. Miao and Z. Ni, *Dyes Pigm.*, 2019, **167**, 143–150.
189 X. Yang, W. Zhang, Z. Yi, H. Xu, J. Wei and L. Hao, *New J. Chem.*, 2017, **41**, 11079–11088.
190 M. Yang, Y. Zhang, W. Zhu, H. Wang, J. Huang, L. Cheng, H. Zhou, J. Wu and Y. Tia, *J. Mater. Chem. C*, 2015, **3**, 1994–2002.
191 K. Muthamma, D. Sunil, P. Shetty, S. D. Kulkarni, P. J. Anand and D. Kekuda, *Prog. Org. Coat.*, 2021, **161**, 106463.
192 N. K. Gondia and S. K. Sharma, *Mater. Chem. Phys.*, 2019, **224**, 314–319.
193 V. Nishal, D. Singh, R. K. Saini, V. Tanwar, S. Kadyan, R. Srivastava and P. S. Kadyan, *Cogent Chem.*, 2015, **1**, 1079291.
194 A. N. Gusev, M. A. Kiskin, E. V. Braga, M. Chapran, G. Wiosna-Salyga, G. V. Baryshnikov, V. A. Minaeva, B. F. Minaev, K. Ivaniuk, P. Stakhira, H. Ågren and W. Linert, *J. Phys. Chem. C*, 2019, **123**, 11850–11859.
195 B. Das, A. Jana, A. Das, D. Chattopadhyay, A. Dhara, S. Mabhai and S. Dey, *Spectrochim. Acta, Part A*, 2019, **212**, 222–231.
196 D. K. Das, J. Kumar, A. Bhowmick, P. K. Bhattacharyya and S. Banu, *Inorg. Chim. Acta*, 2017, **462**, 167–173.
197 V. K. Gupta, A. K. Jain and S. K. Shoora, *Sens. Actuators, B*, 2015, **219**, 218–231.
198 B. Naskar, R. Modak, Y. Sikdar, D. K. Maiti, A. Banik, T. K. Dangar, S. Mukhopadhyay, D. Mandal and S. Goswami, *J. Photochem. Photobiol., A*, 2016, **321**, 99–109.
199 R. Purkait, S. Dey and C. Sinhaa, *New J. Chem.*, 2018, **42**, 16653–16665.
200 G. G. V. Kumar, M. P. Kesavan, M. Sankarganesh, K. Sakthipandi, J. Rajesh and G. Sivaraman, *New J. Chem.*, 2018, **42**, 2865–2873.
201 D. Jothi, S. K. Munusamy, S. Sawminathana and S. K. Iyer, *RSC Adv.*, 2021, **11**, 11338–11346.
202 Q. Lin, X. Jiang, X. Ma, J. Liu, H. Yao, Y. Zhang and T. Wei, *Sens. Actuators, B*, 2018, **272**, 139–145.
203 X. Ma, Z. Zhang, H. Xie, Y. Ma, C. Liu, S. Liu and M. Liu, *Chem. Commun.*, 2018, **54**, 13674–13677.
204 S. K. Panigrahi and A. K. Mishra, *J. Photochem. Photobiol., A*, 2019, **41**, 100318.
205 H. Rubin, *Arch. Biochem. Biophys.*, 2007, **458**, 16–23.
206 R. Y. Walder, B. Yang, J. B. Stokes, P. A. Kirby, X. Cao, P. Shi, C. C. Searby, R. F. Husted and V. C. Sheffield, *Hum. Mol. Genet.*, 2009, **18**, 4367–4375.
207 M. Piskacek, L. Zotova, G. Zsurka and R. J. Schweyen, *J. Cell. Mol. Med.*, 2009, **13**, 693–700.
208 J. Tfelt-Hansen and E. M. Brown, *Crit. Rev. Clin. Lab. Sci.*, 2005, **42**, 35–70.
209 S. Minisola, J. Pepe, S. Piemonte and C. Cipriani, *BMJ*, 2015, **350**, 2723.
210 J. Fong and A. Khan, *Can. Fam. Phys.*, 2012, **58**, 158–62.
211 Y. Wang, Z. Y. Ma, D. L. Zhang, J. L. Deng, X. Chen, C. Z. Xie, X. Qiao, Q. Z. Li and J. Y. Xu, *Spectrochim. Acta, Part A*, 2018, **195**, 157–164.

212 H. Wang, X. Xu, J. Yin, Z. Zhang and L. Xue, *ChemistrySelect*, 2021, **6**, 6454–6459.

213 L. Fan, J. C. Qin, C. R. Li and Z. Y. Yang, *Spectrochim. Acta, Part A*, 2019, **218**, 342–347.

214 L. Bai, F. Tao, L. Li, A. Deng, C. Yan, G. Li and L. Wang, *Spectrochim. Acta, Part A*, 2019, **214**, 436–444.

215 W. Anbu Durai, A. Ramu and A. Dhakshinamoorthy, *Inorg. Chem. Commun.*, 2020, **121**, 108191.

216 L. Bai, G. Li, L. Li, M. Gao, H. Li, F. Tao, A. Deng, S. Wang and L. Wang, *React. Funct. Polym.*, 2019, **139**, 1–8.

217 L. Tomljenovic, *J. Alzheimer's Dis.*, 2011, **23**, 567–598.

218 A. Schiff-base, A. Iii, L. Fan, J. Qin, T. Li, Z. Yang, L. Fan, J. Qin, T. Li, B. Wang and Z. Yang, *J. Lumin.*, 2014, **155**, 84–88.

219 K. S. Patil, P. G. Mahajan and S. R. Patil, *Spectrochim. Acta, Part A*, 2017, **170**, 131–137.

220 C. R. Silva, M. B. N. Oliveira, S. F. Melo, F. J. S. Dantas, J. C. P. De Mattos, R. J. A. C. Bezerra, A. Caldeira-De-Araujo, A. Duatti and M. Bernardo-Filho, *Brain Res. Bull.*, 2002, **59**, 213–216.

221 R. Mcrae, P. Bagchi, S. Sumalekshmy and C. J. Fahrni, *Chem. Rev.*, 2009, **109**, 4780–4827.

222 Y. S. Yang, C. Liang, C. Yang, Y. P. Zhang, B. X. Wang and J. Liu, *Spectrochim. Acta, Part A*, 2020, **237**, 118391.

223 G. Singh, J. Sindhu, Manisha, V. Kumar, V. Sharma, S. K. Sharma, S. K. Mehta, M. H. Mahnashi, A. Umar and R. Kataria, *J. Mol. Liq.*, 2019, **296**, 111814.

224 R. Kouser, S. Zehra, R. A. Khan, A. Alsalme, F. Arjmand and S. Tabassum, *Spectrochim. Acta, Part A*, 2021, **247**, 119156.

225 L. Dong, X. Zeng, L. Mu, S. Xue, Z. Tao and J. Zhang, *Sens. Actuators, B*, 2010, **145**, 433–437.

226 H. Chen, F. Yuan, J. Xu, Y. Zhang, Y. Wu and L. Wang, *Spectrochim. Acta, Part A*, 2013, **107**, 151–155.

227 L. Wang, L. Yang and D. Cao, *J. Fluoresc.*, 2014, **24**, 1347–1355.

228 W. Bian, J. Ma, Q. Liu, Y. Wei, Y. Li, C. Dong and S. Shuang, *Luminescence*, 2014, **29**, 151–157.

229 S. Ramezani, M. Pordel and A. Davoodnia, *Inorg. Chim. Acta*, 2019, **484**, 450–456.

230 P. Aussawaponpaisan, P. Nusuwan, P. Tongraung, P. Jittangprasert, K. Pumsa-Ard and M. Kuno, *Mater. Today Proc.*, 2017, **4**, 6022–6030.

231 D. Vashisht, S. Sharma, R. Kumar, V. Saini, V. Saini, A. Ibhadon, S. C. Sahoo, S. Sharma, S. K. Mehta and R. Kataria, *Microchem. J.*, 2020, **155**, 104705.

232 X. Zhang, S. T. Wu, X. J. Yang, L. Y. Shen, Y. L. Huang, H. Xu, Q. L. Zhang, T. Sun, C. Redshaw and X. Feng, *Inorg. Chem.*, 2021, **60**, 8581–8591.

233 F. Yan, X. Sun, Y. Zhang, Y. Jiang, L. Chen, T. Ma and L. Chen, *J. Photochem. Photobiol., A*, 2021, **407**, 113065.

234 S. Wang, K. Cai, Y. Song and Y. Zhu, *ChemistrySelect*, 2021, **6**, 3788–3794.

235 W. Pan, X. Yang, Y. Wang, L. Wu, N. Liang and L. Zhao, *J. Photochem. Photobiol., A*, 2021, **420**, 113506.

236 A. Goel, N. Tomer, V. D. Ghule and R. Malhotra, *Spectrochim. Acta, Part A*, 2021, **249**, 119221.

237 H. Li, H. Li, Y. Zhu, B. Shi, W. Qu, Y. Zhang, Q. Lin, H. Yao and T. Wei, *Supramol. Chem.*, 2014, **27**, 471–477.

238 M. Liu, T. Wei, Q. Lin and Y. Zhang, *Spectrochim. Acta, Part A*, 2011, **79**, 1837–1842.

239 L. M. Gaetke, H. S. Chow and C. K. Chow, *Arch. Toxicol.*, 2014, **88**, 1929–1938.

240 X. Wang, D. Shi, Y. Xu, S. Yu, F. Zhao, Y. Wang, L. Hu, J. Tian, X. Yu and L. Pu, *Tetrahedron Lett.*, 2018, **59**, 2332–2334.

241 S. Ullmann, R. Schnorr, M. Handke, C. Laube, B. Abel, J. Matysik, M. Findeisen, R. Rüger, T. Heine and B. Kersting, *Chem. – Eur. J.*, 2017, **23**, 3824–3827.

242 S. J. Malthus, S. A. Cameron and S. Brooker, *Inorg. Chem.*, 2018, **57**, 2480–2488.

243 K. Rout, A. K. Manna, M. Sahu and G. K. Patra, *Inorg. Chim. Acta*, 2019, **486**, 733–741.

244 X. Mu, L. Shi, L. Yan and N. Tang, *J. Fluoresc.*, 2021, **31**, 971–979.

245 C. T. Chasapis, A. C. Loutsidou, C. A. Spiliopoulou and M. E. Stefanidou, *Arch. Toxicol.*, 2012, **86**, 521–534.

246 C. F. Walker and R. E. Black, *Annu. Rev. Nutr.*, 2004, **24**, 255–275.

247 Z. Yang, C. Yan, Y. Chen, C. Zhu, C. Zhang, X. Dong, W. Yang, Z. Guo, Y. Lub and W. He, *Dalton Trans.*, 2011, **40**, 2173–2176.

248 M. Hosseini, A. Ghafarlo, M. R. Ganjali, F. Faridbod, P. Norouzi and M. S. Niasari, *Sens. Actuators, B*, 2014, **198**, 411–415.

249 J. Afshani, A. Badiei, M. Karimi, N. Lashgari and G. Mohammadi Ziarani, *Appl. Organomet. Chem*, 2017, **31**, 1–12.

250 W. Fang, G. Zhang, J. Chen, L. Kong, L. Yang, H. Bi and J. Yang, *Sens. Actuators, B*, 2016, **229**, 338–346.

251 G. N. George, R. C. Prince, G. A. Buttigieg, M. B. Denton, H. H. Harris and I. J. Pickering, *Chem. Res. Toxicol.*, 2004, **17**, 999–1006.

252 J. Yan, L. Fan, J. C. Qin, C. R. Li and Z. Y. Yang, *J. Fluoresc.*, 2016, **26**, 1059–1065.

253 D. Mohanasundaram, R. Bhaskar, G. Gangatharan Vinoth Kumar, J. Rajesh and G. Rajagopal, *Microchem. J.*, 2021, **164**, 106030.

254 B. X. Shen and Y. Qian, *ChemistrySelect*, 2017, **2**, 2406–2413.

255 H. Tokunaga, K. Kazama, M. Tsuboi and M. Miyasaka, *Luminescence*, 2021, **36**, 1561–1568.

256 B. Li, Z. Liu, L. Li, Y. Xing, Y. Liu, X. Yang, M. Pei and G. Zhang, *New J. Chem.*, 2021, **45**, 6753–6759.

257 P. S. Hariharan and S. P. Anthony, *Spectrochim. Acta, Part A*, 2015, **136**, 1658–1665.

258 Ö. Şahin, Ü. Ö. Özdemir, N. Seferoğlu, Z. K. Genc, K. Kaya, B. Aydıner, S. Tekin and Z. Seferoğlu, *J. Photochem. Photobiol., B*, 2018, **178**, 428–439.

259 B. Kaur and N. Kaur, *J. Coord. Chem.*, 2019, **72**, 2189–2199.

260 N. Kaur and B. Kaur, *Inorg. Chem. Commun.*, 2020, **121**, 108239.

261 C. Li, L. Xiao, Q. Zhang and X. Cheng, *Spectrochim. Acta, Part A*, 2020, **243**, 118763.

262 E. K. İnal, *J. Fluoresc.*, 2020, **30**, 891–900.

263 S. Dey, R. Purkait, D. Mallick and C. Sinha, *ChemistrySelect*, 2020, **5**, 8274–8283.

264 P. Vijayakumar, E. Dhineshkumar, M. Arockia Doss, S. Nargis Negar and R. Renganathan, *Mater. Today Proc.*, 2020, **42**, 1050–1064.

265 S. Li, D. Cao, X. Meng, Z. Hu, Z. Li, C. Yuan, T. Zhou, X. Han and W. Ma, *J. Photochem. Photobiol., A*, 2020, **392**, 112427.

266 B. Li, X. Gu, M. Wang, X. Liu and K. Xu, *Dyes Pigm.*, 2021, **194**, 109637.

267 S. A. Khan, Q. Ullah, A. S. A. Almalki, S. Kumar, R. J. Obaid, M. A. Alsharif, S. Y. Alfaifi and A. A. Hashmi, *J. Mol. Liq.*, 2021, **328**, 115407.

268 H. He, Z. Cheng and L. Zheng, *J. Mol. Struct.*, 2021, **1227**, 129522.

269 O. A. Urucu and A. Aydin, *Anal. Lett.*, 2015, **48**, 1767–1776.

270 E. S. Almeida, E. M. Richter and R. A. A. Munoz, *Anal. Chim. Acta*, 2014, **837**, 38–43.

271 M. K. Goshisht, L. Moudgil, M. Rani, P. Khullar, G. Singh, H. Kumar, N. Singh, G. Kaur and M. S. Bakshi, *J. Phys. Chem. C*, 2014, **118**, 28207–28219.

272 A. Mahal, M. K. Goshisht, P. Khullar, H. Kumar, N. Singh, G. Kaur and M. S. Bakshi, *Phys. Chem. Chem. Phys.*, 2014, **16**, 14257–14270.

273 M. K. Goshisht, *Adv. Mater. Proc*, 2017, **2**, 535–546.

274 P. Khullar, M. K. Goshisht, L. Moudgil, G. Singh, D. Mandial, H. Kumar, G. K. Ahluwalia and M. S. Bakshi, *ACS Sustainable Chem. Eng.*, 2017, **5**, 1082–1093.

275 M. K. Goshisht, L. Moudgil, P. Khullar, G. Singh, A. Kaura, H. Kumar, G. Kaur and M. S. Bakshi, *ACS Sustainable Chem. Eng.*, 2015, **3**, 3175–3187.

276 H. Dezhampanah, R. Firouzi, Z. Moradi Shoeili and R. Binazir, *J. Mol. Struct.*, 2020, **1205**, 127557.

277 M. Cui, Y. Xin, R. Song, Q. Sun, X. Wang and D. Lu, *Cellulose*, 2020, **27**, 1621–1633.

278 X. Zeng, X. Zhang, B. Zhu, H. Jia and J. Xue, *Analyst*, 2011, **136**, 4008–4012.

279 Y. Sun, Y. Lu, M. Bian, Z. Yang, X. Ma and W. Liu, *Eur. J. Med. Chem.*, 2021, **211**, 113098.

280 S. Hazra, B. G. M. Rocha, A. K. M. Fátima, C. Guedes da Silva and A. J. L. Pombeiro, *Inorganics*, 2019, **7**, 17.

281 A. Soroceanu, M. Cazacu, S. Shova, C. Turta, J. Kožíšek, M. Gall, M. Breza, P. Rapta, T. C. O. Mac Leod, J. T. Armando, J. L. Pombeiro, A. A. Dobrov and V. B. Arion, *Eur. J. Inorg. Chem.*, 2013, 1458–1474.

282 Y. Wang, Q. Guo, X. Wu, H. Gao, R. Lu and W. Zhou, *Spectrochim. Acta, Part A*, 2022, **265**, 120358.

283 J. J. Celestina, P. Tharmaraj, C. D. Sheela and J. Shakina, *J. Lumin.*, 2021, **239**, 118359.

284 S. O. Tümay and S. Yeşilot, *J. Photochem. Photobiol., A*, 2021, **407**, 113093.

285 D. Aydin, S. Dinckan, S. N. Karuk Elmas, T. Savran, F. N. Arslan and I. Yilmaz, *Food Chem.*, 2021, **337**, 127659.

286 Z. Li, X. Zhang, S. Wang, Y. Yang, B. Qin, K. Wang, T. Xie, Y. Wei and Y. Ji, *Chem. Sci.*, 2016, **7**, 4741–4747.

287 D. Genovese, A. Aliprandi, E. A. Prasetyanto, M. Mauro, M. Hirtz, H. Fuchs, Y. Fujita, H. Uji-i, S. M. K. Lebedkin and L. De Cola, *Adv. Funct. Mater.*, 2016, **26**, 5271–5278.

288 C. Ma, B. Xu, G. Xie, J. He, X. Zhou, B. Peng, L. Jiang, B. Xu, W. Tian, Z. Chi, S. Liu, Y. Zhang and J. Xu, *Chem. Commun.*, 2014, **50**, 7374–7377.

289 B. Yoon, J. Lee, I. S. Park, S. Jeon, J. Lee and J.-M. Kim, *J. Mater. Chem. C*, 2013, **1**, 2388–2403.

290 L. Peng, Y. Zheng, X. Wang, A. Tong and Y. Xiang, *Chem. – Eur. J.*, 2015, **21**, 4326–4332.

291 K. Li, Y. Xiang, X. Wang, J. Li, R. Hu, A. Tong and B. Z. Tang, *J. Am. Chem. Soc.*, 2014, **136**, 1643–1649.

292 Y. Jhong, W. H. Hsieh, J. Chir and A. Wu, *J. Fluoresc.*, 2014, **24**, 1723–1726.

293 Z. Y. Yin, J. H. Hu, K. Gui, Q. Q. Fu, Y. Yao, F. L. Zhou, L. L. Ma and Z. P. Zhang, *J. Photochem. Photobiol., A*, 2020, **396**, 112542.